



FRIEDRICH-SCHILLER-
UNIVERSITÄT
JENA

DISSERTATION

Diffraction-based metrology
in the extreme ultraviolet

Dissertation zur Erlangung des akademischen Grades

Doctor rerum naturalium (Dr. rer. nat.)

vorgelegt dem Rat der Physikalisch-Astronomischen Fakultät der

Friedrich-Schiller-Universität Jena

von M. Sc. Frederik Tuitje

geboren am 22.06.1989 in Goslar

Gutachter

1. Prof. Dr. Christian Spielmann
Institut für Optik und Quantenelektronik
Friedrich-Schiller-Universität Jena
2. Prof. Dr. Birgit Kanngießer
Institut für Optik und Atomare Physik
Technische Universität Berlin
3. Dr. Hab. Hamed Merdji
Laboratoire Interactions, Dynamiques et Lasers
Université Paris-Saclay, Centre national de la recherche scientifique

Tag der Disputation: 13.10.2020

FRIEDRICH-SCHILLER UNIVERSITÄT

Abstract

Faculty of Physics and Astronomy
Institute for Optics and Quantum Electronics

Doctor rerum naturalium (Dr. rer. nat.)

Diffraction-based metrology in the extreme ultraviolet

by M. Sc. Frederik TUITJE

Lensless imaging in the extreme ultraviolet (XUV) down to the soft X-ray spectral range enables nanoscale resolutions with material-sensitive properties of the smallest objects thanks to increasing computing power and photon fluxes. The removal of the lenses not only leads to a theoretically diffraction-limited resolution, but also to a complex reconstruction of the sample. The growing numerical development of Coherent Diffraction Imaging (CDI) towards ptychography allows for the first time the separate reconstruction of object and the wavefront illuminating it. This work is dedicated to the investigation of further possibilities resulting from the complex reconstruction of object and illumination.

In this work, gold structures buried in silicon are reconstructed and examined with regard to their surface morphology. For this purpose, previously prepared samples are illuminated by high-energy synchrotron radiation and the resulting diffraction patterns are recorded in reflection geometry. This completely non-destructive method allows metrology on structures of embedded circuits and otherwise hidden defects. Lateral resolutions of less than 150 nm are achieved and the used wavelength of 5 nm allows surface roughness of less than 1 nm to be detected.

The increasing demand for easily accessible and compact high-performance light sources around the silicon and water window opens the question regarding their suitability for lensless imaging. Since these laser-plasma-based sources emit mostly

incoherent radiation, a more precise analysis of the beam parameters is required. In the following chapters a method is introduced which allows an almost complete source analysis by means of a single long time exposed diffraction pattern. The knowledge gained in this way allows an improvement of the source with respect to water window CDI and provides insight into dynamic processes within the source. Following on from the above mentioned source measurement, the complex-valued reconstruction of the wavefront allows an insight into the plasma and the ionization states prevailing there. The XUV seed pulse of a seeded Soft-X-Ray laser (SXRL), which passes the pumped plasma and changes its properties with respect to the states in the plasma, is reconstructed ptychographically. The complex-valued wavefront obtained in this way is propagated back to the location of the plasma using known optics. Adapted Maxwell-Bloch simulations allow by comparison with the measurement to restore the ionization states during the passage of the seed pulse. The spatially resolved ionization states obtained show over-ionization and thus a possible limitation of the SXRL concept used.

In order to exclude sources of error, periodic objects with large dimensions were used during most of the experiments presented here. This made the precise alignment of the object when using ptychography obsolete. Previous experiments showed artifacts during reconstruction, which were directly related to the periodicity of the objects. Simulation of periodic objects of different sizes and with the addition of intentional defects showed a dependence of the reconstruction of the object on the illumination function. Various criteria were derived from this simulation and are presented in this thesis.

FRIEDRICH-SCHILLER UNIVERSITÄT

Zusammenfassung

Physikalisch-Astronomische Fakultät
Institut für Optik und Quantenelektronik

Doctor rerum naturalium (Dr. rer. nat.)

Diffraction-based metrology in the extreme ultraviolet

von M. Sc. Frederik TUITJE

Linsenlose Bildgebung im extremen ultravioletten (XUV) bis hin zum weichen Röntgenbereich ermöglicht, dank steigender Rechenleistung und immer höheren Photonenflüssen, nanoskalige Auflösungen mit materialelektiven Eigenschaften von kleinsten Objekten. Das Entfernen optischer Elemente, wie Linsen oder Spiegel, führt nicht nur zu einer theoretisch beugungslimitierten Auflösung, sondern auch zu einer komplexwertigen Rekonstruktion der Probe. Die numerische Weiterentwicklung des Coherent Diffraction Imaging (CDI) hin zu Ptychographie erlaubt erstmals die getrennte Rekonstruktion von Objekt und der auftreffenden Wellenfront. Anknüpfend an diesen Sachverhalt widmet sich diese Arbeit der Untersuchung weiterer Möglichkeiten, die sich aus der komplexwertigen Rekonstruktion von Objekt und Beleuchtung ergeben.

Im Rahmen dieser Arbeit werden in Silizium vergrabene Goldstrukturen rekonstruiert und hinsichtlich ihrer Oberflächenmorphologie untersucht. Dazu werden vorher präparierte Proben mittels hochenergetischer Synchrotronstrahlung beleuchtet und die Diffraktogramme in Reflexionsgeometrie aufgenommen. Diese völlig zerstörungsfreie Methode ermöglicht Metrologie an Strukturen eingebetteter Schaltkreise und sonst verborgener Defekte. Es werden laterale Auflösungen unter 150 nm erreicht und durch die verwendete Wellenlänge von 5 nm können Oberflächenrauigkeiten unter 1 nm detektiert werden.

Die steigende Nachfrage hin zu leicht zugänglichen und kompakten Hochleistungsquellen um Silizium- und Wasserfenster eröffnet die Frage hinsichtlich ihrer Eignung für die linsenlose Bildgebung. Da diese Laser-Plasma basierten Quellen zum großen Teil inkohärente Strahlung emittieren, bedarf es einer genaueren Analyse der Strahlparameter. In den folgenden Kapiteln wird ein Verfahren eingeführt, welches eine nahezu vollständige Quellanalyse mittels eines einzigen langzeitbelichteten Diffraktogrammes ermöglicht. Die so gewonnenen Erkenntnisse ermöglichen eine Verbesserung der Quelle hinsichtlich Wasserfenster CDI und den Einblick dynamischer Vorgänge innerhalb der Quelle.

Anknüpfend an die Quellvermessung erlaubt die komplexwertige Rekonstruktion der Wellenfront einen Einblick in das Plasma und die dort herrschenden Ionisationszustände. Der XUV Seed-Puls eines seeded Soft-X-Ray-Lasers (SXRL), welcher das gepumpte Plasma passiert und dabei seine Eigenschaften hinsichtlich der Zustände im Plasma verändert, wird ptychographisch rekonstruiert. Die so gewonnene komplexwertige Wellenfront wird unter Beachtung bekannter Optiken zum Ort des Plasmas zurück propagiert. Angepasste Maxwell-Bloch Simulationen ermöglichen durch Vergleich mit der Messung eine Wiederherstellung der Ionisationszustände während des Durchganges des Seed-Pulses. Die gewonnenen, räumlich aufgelösten Ionisationszustände zeigen Überionisation und somit eine mögliche Limitierung des genutzten SXRL Konzepts.

Um Fehlerquellen auszuschließen, wurden während der meisten hier vorgestellten Experimente periodische Objekte mit großer Ausdehnung verwendet. Dadurch wurde das präzise Ausrichten des Objektes bei Anwendung von Ptychographie obsolet. Vorangegangene Experimente zeigten Artefakte während der Rekonstruktion, welche direkt auf die Periodizität der Objekte zurückzuführen waren. Simulation von periodischen Objekten verschiedener Größen und unter Zugabe von absichtlichen Defekten zeigte eine Abhängigkeit der Rekonstruktion des Objektes von der Beleuchtungsfunktion. Verschiedene Kriterien wurden aus dieser Simulation hergeleitet und werden innerhalb dieser Arbeit dargestellt.

Contents

Abstract	i
Zusammenfassung	iii
Contents	1
1 Introduction	4
1.1 The path to lensless imaging	4
1.2 Outline of this thesis	9
2 Fundamentals	10
2.1 Light and its properties	10
2.1.1 Coherence	10
Spatial coherence	11
Temporal coherence	11
2.1.2 Diffraction	11
Kirchhoff diffraction	12
Fresnel and Fraunhofer approximation	14
2.2 Lensless imaging	16
2.2.1 The phase problem	16
2.2.2 Coherent Diffraction Imaging	18
2.2.3 Ptychography	19
2.2.4 Phase retrieval transfer function	21
2.2.5 Resolution vs. exposure	22
2.3 XUV radiation sources	23
2.3.1 Synchrotron sources	23

	2
2.3.2	High Harmonic Generation 24
2.3.3	Laser-Plasma sources 26
2.3.4	Comparison 27
3	Reflection mode CDI at high photon energies 28
3.1	Experimental setup 30
3.2	Reflection-mode CDI of a buried sample 31
3.3	Summary 36
4	Imaging with a laser-driven soft X-ray source in the water-window 37
4.1	Experimental setup 38
4.2	Labeled bio-imaging with zone-plates 39
4.3	Source characterization with a single diffraction pattern 42
4.4	Summary 51
5	Beam diagnostics of a seeded SXRL for ultrafast XUV imaging 52
5.1	Experimental setup 53
5.2	Single-shot ultrafast lensless diffraction imaging with binary samples 56
5.3	Plasma investigations via ptychographic reconstructions 63
5.4	Summary 70
6	Ptychographic imaging of periodic structures 72
6.1	Numerical model and methods 74
6.2	Simulation results 75
6.3	Defects 79
6.4	Summary 84
7	Synopsis 86
7.1	Conclusions 86
7.2	Overview of experimental data and results 89
7.3	Outlook 90
7.3.1	Ghost imaging assisted CDI 90
7.3.2	In-situ diagnostics 90

A	Pre-processing of diffraction data	92
A.1	Background correction	93
A.2	Noise removal	93
A.3	Hot- and Cold-pixel elimination	94
A.4	Centering	95
A.5	Curvature and tilted plane correction	95
A.6	Additional processing: High dynamic range	98
B	Simulation of diffraction pattern	100
B.1	Framework	100
	Bibliography	102
	List of Figures	115
	List of Abbreviations	118
	List of Symbols	120
	Physical Constants	121
	Danksagung	122
	List of scientific contributions	125
	Eidesstattliche Erklärung	128

Chapter 1

Introduction

1.1 The path to lensless imaging

With the invention of the microscope in the early 17th century, a dramatically changed view on the world has been initiated. As the counterpart of the telescope, the up to this point invisible became tangible, revealing new mechanisms in different disciplines such as life- and material sciences. Hence, it made an essential contribution to the enlightenment towards our present world view. The basic principle of microscopy, to increase the viewing angle and therefore made observations on the smallest scales possible, were re-interpreted during the last centuries.

With the discovery of wave properties of matter by de Broglie around 1924 [1], the principle of microscopy could be applied to new forms of radiation to implement techniques from electron- [2] to neutron- microscopy [3]. Using matter particles instead of photons go hand in hand with different absorption and reflection mechanisms, revealing different views of the same object. The subsequently developed electron microscope for example allows to image the outer-shell electron configuration enabling a deep view into the matter of the sample. Due to the small de Broglie wavelength of fast electrons, the resolution could be increased to the nanometer scale. With the development of the field-ion microscope 1951 [4], the atomic scale was reached for the first time, enabling a direct view on the building blocks of our universe, excluding sub-atomic particles. However, these techniques underlie special preparation of the samples to be observed and are quite bulky and challenging to implement. Therefore, “classical” light microscopy is still the most use technique in the modern scientific world.

Like every physical concept, light-based microscopy underlies fundamental restrictions, avoiding further enhancements. Bypassing these restrictions is a matter of research until nowadays. Especially the resolution as a major parameter is an object of great effort, as it defines the level of detail. In 1873 Abbe defined the famous fundamental limit of resolution using wave optics [5] and plane waves, which is up to now the benchmark for developing imaging systems:

$$d = \frac{\lambda}{n \sin(\alpha)} = \frac{\lambda}{\text{NA}} \quad (1.1)$$

Here, λ is the used wavelength and NA is the numerical aperture, defined by the refraction index n between object and objective lens and α is the half opening angle of the field-of-view (FOV). Abbes law defines the distance d between two point-like light sources, where they can still be observed as separated. Using adapted illumination (Köhler illumination [6]) even extends the resolution by a factor of 2 ($d/2$). Driving this distance to shrinking scales calls out either for enlargement of the opening angle and the refraction index or decreasing the used wavelength. Whereas the opening angle is limited to a maximum of 90° (de facto limited to 80° found at high performance objectives) by the focal length and size of the lens, the refraction index can be increased by using an immersion medium between object and lens. However, also these enhancements come to an end induced by technological capabilities. As the wavelength is a, generally assumed, unconfined parameter, efforts were taken over the last decades to strive for highest resolutions by decreasing the wavelength further and further. With leaving the visible spectrum of light and diving into the ultraviolet regime, not only the resolution adapts, but also fluorescence effects can be harnessed for an augmented visualization of the microscopic universe [7]. Based on this technology, many developments were made, e.g. multi-photon-fluorescence microscopy [8] or STED-microscopy [9]. With decreasing wavelength, different interactions between light and matter appear. Whereas in the visible regime around 500 nm, light mainly interacts with the valence electrons, photons with higher energy starts to stimulate inner-shell electrons. Increasing the photon energy to the UV regime therefore increases the probability of absorption and reaches its peak in the

extreme ultraviolet (XUV) regime between approx. 100 and 10 nm, where absorption edges lead to opacity of most elements. Further increase of the energy into the soft- and hard X-ray regime shows again a higher transmission due to non-resonant electrons. Transmitting materials in this wavelength regime, however, show a refraction index close to vacuum, refraction-based imaging becomes therefore difficult and other methods have to be found [10–12].

Due to the existence of absorption edges in the XUV, it becomes an interesting spectral range for chemical and morphological analysis via e.g. near-edge x-ray absorption fine structure (NEXAF) [13]. The XUV regime contains different “windows” of lowered absorption for a specific material. The silicon window between 40 and 12 nm allowing semiconductor metrology [14] utilizing the otherwise high absorption. Biological investigations [15] in the water-window between 4.4 and 2.3 nm profit from a high contrast between carbon and oxygen. Using the fully concentrated XUV light without using spatial information benefits spectroscopic techniques to exceed the noise level despite the high absorption, but also call out for thin samples. Imaging techniques relying on refraction however have to deal with the high absorption of the specimen and the used optics together with the spatially distributed light. Even reflective optics using advanced multilayer techniques only reach reflectivities in the sub-percentage level [16]. To overcome these restrictions, the Fourier transforming property of lenses was exchanged by a numerical transform [17]. Removing the lens and using a spatial and temporal coherent light source leading to a projection of the near- or far-field pattern of the object onto an image sensor. Now, a simple inverse Fourier transform could recover the spatial information of the object, if there were not a considerable impairment: As every light-sensing detector is intensity sensitive, the phase of the incident wave is lost. Added to this, the detector needs a certain exposure time, to gather enough photons, averaging intrinsically temporal and spatial jittering. To recover the canceled-out phases, many attempts were made during the last century. Historically, this idea origins of crystallographic and electron-microscopic problems in the 1940s and grow into the optical sector with holography, where this so-called “phase problem” is solved via interference with a reference wave [18], developed shortly after the

first run of a laser 1960. This well-known wave enables coding the phase in the intensity pattern and therefore allows a rather simple reconstruction using algorithmic frameworks [19]. Illuminating an object with coherent light without a reference contains therefore no external interference-based phase modulation: The solution of the inverse problem becomes ambiguous. The reconstruction of these pattern is commonly referred to coherent diffractive imaging (CDI) and requires special numerical attention. Iterative algorithms become necessary to recover the phase and finally the object via an inverse Fourier transform [20]. This becomes possible during the 1980s with increasing computing power, inevitable for challenging the amount of data. From then on, more and more sophisticated phase-retrieval algorithms were developed [17, 21]. The additional numerical expenditure is rewarded with diffraction limited, complex-valued object images allowing conclusion about the objects material composition and thickness.

For a successful reconstruction, algorithms and constraints have to be adapted to the object, therefore, a low level of prior knowledge is necessary: A fundamental restriction of CDI is the size of the object, which has to be smaller than half of the illumination spot dimensions to not violate the Nyquist sampling condition [22]. This fundamental constraint could be relaxed by recording of diffraction patterns from overlapping illuminations with known distances. Here, the translation invariance of the Fourier transform lead to a certain degree of redundancy in neighboring diffraction pattern, paving the way for a new principle of phase retrieval called Ptychography (Greek: *ptyche*, $\pi\tau\nu\chi\eta$ = fold). Despite that the basic principle of Ptychography origins also from electron microscopy in the 90s of the last century [23], it has only recently becomes of large interest for the diffraction imaging community. The relatively high requirements to computing power, particularly considering additionally refining operations like position determination [24] and the increased detector resolution over the last years, could be fulfilled with the development of graphical processor (GPU)-based, highly parallelized calculations. The above proportional rise in computing power allowed the implementation of algorithmic frameworks, capable of separating the incident complex-valued illumination from the object [25]. As a result, ptychographic imaging could be used for wavefront characterization and

beam diagnostics, offering new applications in numerous disciplines.

Arrived today, CDI and its extension Ptychography are well-implemented tools in various fields of applied science. They were combined with nearly every man-made light source from the terahertz-scale [26] to the hard X-ray regime [27]. The possibility of determining the complex-valued wavefront at position of the sample allows interesting insights into the mechanism of the used light sources and materials in between and defines the starting point for the following thesis.

1.2 Outline of this thesis

This work is intended to tie with above mentioned properties and is concerned with the possibilities, lensless imaging offer beside the classical imaging of specimens. In the second chapter, fundamentals about the physics of lensless imaging are presented, followed by a brief introduction into the here used sources of XUV radiation. The third chapter deals with CDI at high energies in reflection geometry at *PETRAIII* (*DESY Hamburg*) to reveal buried structures in silicon and pointing out application in semiconductor research and metrology.

In the fourth chapter, the spectral window changed to the water window, where a plasma-based partially coherent laser-plasma source at *BliX* (*MBI Berlin*) emitting at 500 eV is investigated regarding its suitability for lensless imaging. A new framework was developed to gather information about the sources's stability and coherence properties with the record of only one long-exposed diffraction pattern.

Following on plasma diagnostics, the enhanced properties of a seeded soft X-ray Laser (SXRL) at *LOA* (*Ensta-Tech Paris*) are discussed in the fifth chapter. First, single-shot imaging was performed to enroll the important parameter for a developed ptychographic framework, which allows the reconstruction of ion states in the laser plasma amplifier (LPA) during the shots. The later discussed framework draws benefits from the seed of the SXRL, which accumulate the effects occurring in the LPA. To do so, Ptychography was implemented to reconstruct the complex-valued wavefront, containing the longitudinal averaged seed at the samples position.

The experiments, presented in this work, used mostly periodic objects. This and previous, preparatory experiments, show the importance of a closer look to the behavior of ptychography applied on periodic structures. The penultimate chapter will therefore discuss possible problems and solutions regarding this topic.

The experimental works were done at different places with different XUV-sources. Therefore, every chapter will discuss the setup separately in order to keep the overview and maintain faster access to parameters during reading.

Chapter 2

Fundamentals

2.1 Light and its properties

Light as an electromagnetic phenomenon can be described as optical waves $\Psi(\mathbf{r}, t)$ at position \mathbf{r} and time t which has to satisfy the wave equation.

$$\nabla^2\Psi - \frac{1}{c^2}\frac{\partial^2\Psi}{\partial t^2} = 0 \quad (2.1)$$

Every function Ψ fulfilling the wave equation represents therefore a possible somehow formed optical wave [28]. Out of the special characteristics of these equations, properties of the corresponding waves can be derived, e.g. superposition of waves due to the linearity of the wave equation. It follows a plethora of properties and conclusions, which cannot be fully discussed here. Therefore, for more detailed information, please refer to e.g. [28]. In the following sections, only the properties of coherence and diffraction shall be discussed, as they directly impact this work.

2.1.1 Coherence

As mentioned, the linearity of the wave equation enables optical waves to superpose without disturbing each other. This however enables interference of waves starting from different origins at different timings. The relation of their phases, and therefore their capability to stably interfere over time and space, defines the coherence and is a property of a complex-valued light field. Here, two distinctions can be made: spatial and temporal coherence.

Spatial coherence

Spatial coherence impinge the phase relation between two distanced, fixed points P_1, P_2 on a wavefront. The wavefront can be considered as coherent, if the phase relation remain constant. Typically the coherence decreases with increasing distance between the points. One can define the spatial coherence by interfere two spherical waves emerging of P_1 and P_2 . By measuring the contrast of the resulting fringes e.g. on a screen and applying a certain criterion (e.g. ratio between fringe maxima and minima to 0.5), the distance $\overline{P_1 P_2}$ defines the transversal coherence length ζ_t , if the contrast criterion is undercut. Due to the nature of light propagation, disturbed wavefronts gain on spatial coherence with distance to the light source z and decreasing size of the emitter d according to the Van Cittert-Zernicke theorem [28]:

$$\zeta_t = \frac{z\lambda}{2\pi d} \quad (2.2)$$

Temporal coherence

Phase jumps during propagation or generation of light cause sudden changes of phase relations at a fixed point on the wavefront and lowers the temporal coherence. These sudden changes away from the harmonic wave can caused by overlaying waves of different frequencies resulting in polychromatic light. The longitudinal coherence length ζ_l is the distance, light passes in the time between two disturbances in the wavefront and directly depends on the Gaussian distributed spectral width $\Delta\lambda$ of the light [29]:

$$\zeta_l = \frac{\lambda^2}{\Delta\lambda} \quad (2.3)$$

2.1.2 Diffraction

Starting with a qualitative view on this topic, diffraction can be assumed as the interference of all spherical waves (elementary waves) outgoing from an illuminated object (aperture). This well known *Huygens-Fresnel-principle* takes place after a certain propagation distance from the aperture to form the superposition of all elementary waves [30]. Whereas in the close vicinity of the aperture, the field can be

described by geometrical optics¹, the further propagated waves start to build up the interference pattern quickly in the Fresnel regime. For distances far away from the aperture, the spherical waves can be regarded as plane waves with different phases.

Kirchhoff diffraction

This intuitive view shall now be quantitatively discussed by the derivation of the *Fresnel-Kirchhoff diffraction formula* [29]. Fig. 2.1 shows the diffraction from a light source Q at an aperture a .

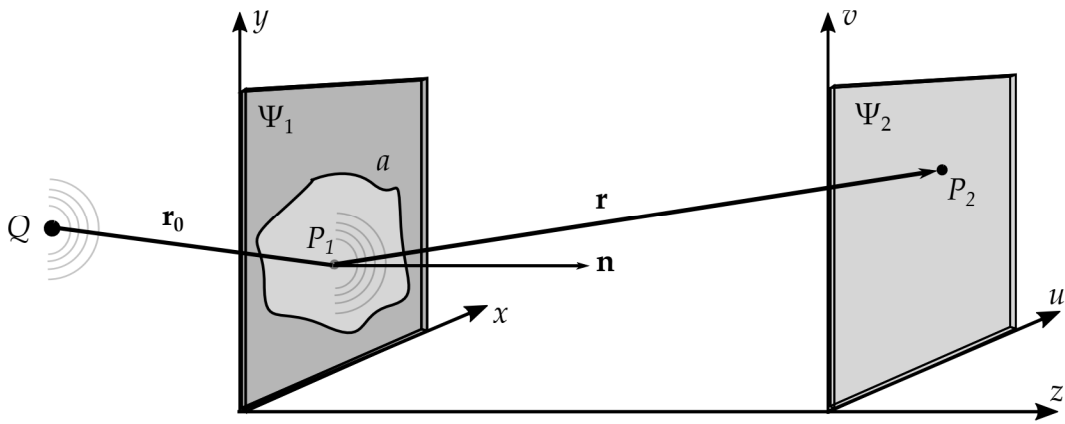


FIGURE 2.1: Schematic of diffraction for derivation of the Fresnel-Kirchhoff diffraction formula. A light source Q illuminates an aperture a , which results in the complex field Ψ_1 . The at point P_1 generated spherical wave propagates along \mathbf{r} to the point P_2 at the detector plane, where it interfere with other spherical waves outgoing from different points of the aperture. Due to the interference of all waves, the complex field Ψ_2 is generated. The vector \mathbf{r}_0 connects the light source with P_1 . The normal vector \mathbf{n} is perpendicular to a

To determine the light distribution at point P_2 , one has to assume a large aperture (larger than the wavelength), which has to be small compared to the distances $|\mathbf{r}_0| = r_0$ and $|\mathbf{r}| = r$ [29]. With *Kirchhoff integral theorem*:

$$\Psi(P_2) = \frac{1}{4\pi} \iint_a \left[\Psi \frac{\partial}{\partial n} \left(\frac{1}{r} \right) - \frac{1}{r} \frac{\partial \Psi}{\partial n} \right] da \quad (2.4)$$

one can calculate $\Psi(P_2)$ with integration over the surface S (see Fig. 2.2) formed by the aperture a , a portion b of the non-illuminated side of the non-transparent part of the screen and a large sphere c of radius R , with P_2 at the centre [29].

¹propagation length \approx wavelength

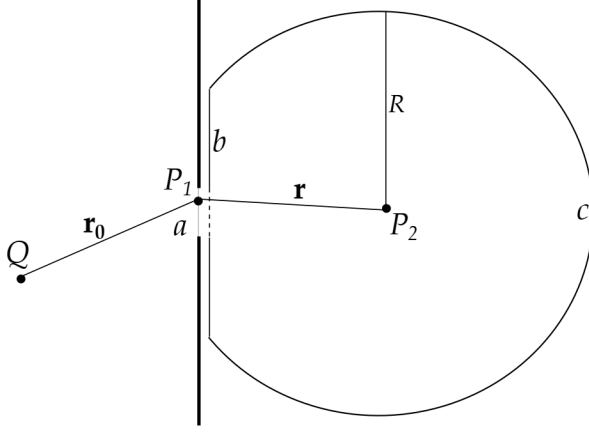


FIGURE 2.2: Schematic of diffraction with the Surface S formed by the aperture a , the non-illuminated screen b and a large sphere c , centred at P_2

$$\Psi(P_2) = \frac{1}{4\pi} \left[\iint_a + \iint_b + \iint_c \right] \left(\Psi \frac{\partial}{\partial \mathbf{n}} \left(\frac{e^{i\mathbf{k}\mathbf{r}}}{r} \right) - \left(\frac{e^{i\mathbf{k}\mathbf{r}}}{r} \right) \frac{\partial \Psi}{\partial \mathbf{n}} \right) dS \quad (2.5)$$

Here, $\mathbf{k} = \mathbf{e}2\pi/\lambda$ defines the wavevector along the unit vector \mathbf{e} perpendicular directed to the wavefront. It is difficult to know the values Ψ and $\frac{\partial \Psi}{\partial n}$ on a, b, c . One can suppose, that everywhere on a , Ψ and $\frac{\partial \Psi}{\partial n}$ will not much differ from the values obtained in the absence of the screen (*Kirchhoff's boundary conditions*) [29]:

$$\text{for } a : \Psi = \Psi^i, \quad \frac{\partial \Psi}{\partial \mathbf{n}} = \frac{\partial \Psi^i}{\partial \mathbf{n}} \quad (2.6)$$

$$\text{for } b : \Psi = 0, \quad \frac{\partial \Psi}{\partial \mathbf{n}} = 0 \quad (2.7)$$

where

$$\Psi^i = \frac{Ae^{i\mathbf{k}\cdot\mathbf{r}_0}}{r_0}, \quad \frac{\partial \Psi^i}{\partial \mathbf{n}} = \frac{Ae^{i\mathbf{k}\cdot\mathbf{r}_0}}{r_0} \left[ik - \frac{1}{r_0} \right] \cos(\angle(\mathbf{n}, \mathbf{r}_0)) \quad (2.8)$$

are the values from the incident field from the source (see Fig.2.1) and A is a constant. The remaining problem is the integration over the sphere c . The first assumption is increasing R which let the integral vanish, but with increasing R , the area of c also increases beyond all limits, so that $\Psi \rightarrow 0$ and $\frac{\partial \Psi}{\partial \mathbf{n}} \rightarrow 0$ are not sufficient to make the integral vanish [29].

Hence, a new assumption has to be made. The field propagates with the speed of light c_0 , therefore points exists that the field has not reached yet, but the disturbance at P_2 is measurable. Thus, R has to be chosen so large, that at the time when the disturbance at P_2 is considered, no contributions from c could have reached P_2 , then the integral over c will vanish. Neglecting in the normal derivatives the terms $\frac{1}{r_0}$

and $\frac{1}{r}$, one can obtain the *Fresnel-Kirchhoff diffraction formula* [29]:

$$\Psi(P_2) = -\frac{iA}{2\pi} \iint_a \frac{e^{i\mathbf{k}(\mathbf{r}_0+\mathbf{r})}}{r_0 r} [\cos(\angle(\mathbf{n}, \mathbf{r}_0)) - \cos(\angle(\mathbf{n}, \mathbf{r}))] dS \quad (2.9)$$

Fresnel and Fraunhofer approximation

To simplify Eq. 2.9 one has to examine this equation more closely. Therefore one can assume, that the term $e^{i\mathbf{k}(\mathbf{r}_0+\mathbf{r})}$ oscillate rapidly, because $(\mathbf{r}_0 + \mathbf{r})$ will change by many wavelengths. If the distance of the points Q and P_2 to P_1 are large compared to the aperture size and one further assume an additional point P'_0 on the aperture (see Fig. 2.3), the term $[\cos(\angle(\mathbf{n}, \mathbf{r}_0)) - \cos(\angle(\mathbf{n}, \mathbf{r}))]$ will not vary significantly and can be simplified to $2 \cos(\delta)$ [29].

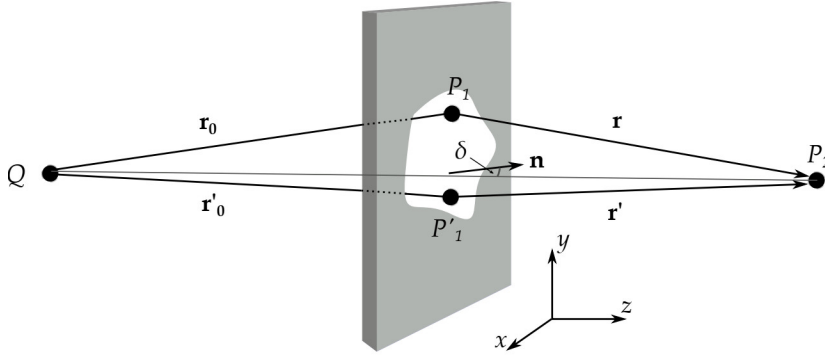


FIGURE 2.3: Schematic to illustrate the Fresnel/Fraunhofer approximation with a second spherical wave from point P'_1 . The angle δ is between the normal \mathbf{n} of the aperture and the line $\overline{QP_2}$.

The factor $\frac{1}{r_0 r}$ will be replaced by $\frac{1}{\tilde{r}_0 \tilde{r}}$, where \tilde{r}_0 and \tilde{r} are the distance of Q and P_2 from \tilde{P}_1 . Then Eq. 2.9 reduces to:

$$\Psi(P_2) \sim -\frac{iA \cos(\delta)}{\pi \tilde{r}_0 \tilde{r}} \iint_a e^{i\mathbf{k}(\mathbf{r}_0+\mathbf{r})} dS \quad (2.10)$$

One can switch to Cartesian coordinates to get a further expression of Eq. 2.10:

$$\begin{aligned} r_0^2 &= (x_Q - x_{\tilde{P}_1})^2 + (y_Q - y_{\tilde{P}_1})^2 + z_Q^2 \\ r^2 &= (x_{P_2} - x_{\tilde{P}_1})^2 + (y_{P_2} - y_{\tilde{P}_1})^2 + z_{P_2}^2 \\ \tilde{r}_0^2 &= x_Q^2 + y_Q^2 + z_Q^2 \\ \tilde{r}^2 &= x_{P_2}^2 + y_{P_2}^2 + z_{P_2}^2 \end{aligned} \quad (2.11)$$

Assuming, that the dimensions of the aperture are small compared to \tilde{r}_0 and \tilde{r} , r_0 and r can be expanded as a power series in $\frac{x_{\tilde{P}_1}}{\tilde{r}_0}$, $\frac{y_{\tilde{P}_1}}{\tilde{r}_0}$, $\frac{x_{\tilde{P}_1}}{\tilde{r}}$ and $\frac{y_{\tilde{P}_1}}{\tilde{r}}$:

$$\begin{aligned} r_0 &\sim \tilde{r}_0 - \frac{x_Q x_{\tilde{P}_1} + y_Q y_{\tilde{P}_1}}{\tilde{r}_0} + \frac{x_{\tilde{P}_1}^2 + y_{\tilde{P}_1}^2}{2\tilde{r}_0} - \frac{(x_Q x_{\tilde{P}_1} + y_Q y_{\tilde{P}_1})^2}{2\tilde{r}_0^3} - \dots \\ r &\sim \tilde{r} - \frac{x_{P_2} x_{\tilde{P}_1} + y_{P_2} y_{\tilde{P}_1}}{\tilde{r}} + \frac{x_{\tilde{P}_1}^2 + y_{\tilde{P}_1}^2}{2\tilde{r}} - \frac{(x_{P_2} x_{\tilde{P}_1} + y_{P_2} y_{\tilde{P}_1})^2}{2\tilde{r}^3} - \dots \end{aligned} \quad (2.12)$$

With Eq. 2.12 in Eq. 2.10 one get the following equation:

$$\Psi(P_2) = -\frac{iA \cos(\delta) e^{ik(\tilde{r}_0 + \tilde{r})}}{\lambda \tilde{r}_0 \tilde{r}} \iint_a e^{ikf(x_{\tilde{P}_1}, y_{\tilde{P}_1})} dx_{\tilde{P}_1} dy_{\tilde{P}_1} \quad (2.13)$$

with

$$\begin{aligned} f(x_{\tilde{P}_1}, y_{\tilde{P}_1}) &\sim \frac{x_Q x_{\tilde{P}_1} + y_Q y_{\tilde{P}_1}}{\tilde{r}_0} - \frac{x_{P_2} x_{\tilde{P}_1} + y_{P_2} y_{\tilde{P}_1}}{\tilde{r}} \\ &+ \frac{x_{\tilde{P}_1}^2 + y_{\tilde{P}_1}^2}{2\tilde{r}_0} + \frac{x_{\tilde{P}_1}^2 + y_{\tilde{P}_1}^2}{2\tilde{r}} \\ &- \frac{(x_Q x_{\tilde{P}_1} + y_Q y_{\tilde{P}_1})^2}{2\tilde{r}_0^3} - \frac{(x_{P_2} x_{\tilde{P}_1} + y_{P_2} y_{\tilde{P}_1})^2}{2\tilde{r}^3} \dots \end{aligned} \quad (2.14)$$

Now the complex field at the point P_2 can be determined with the evaluation of Eq. 2.13. One can further simplify this equation by neglecting the quadratic and higher order terms in Eq. 2.14, this case is called *Fraunhofer diffraction*, describing the far field and is identical to a Fourier transform of the aperture. This is only valid in the limiting case $\tilde{r}_0, \tilde{r} \rightarrow \infty$. The near field is described by considering also the quadratic terms and is called *Fresnel diffraction* [29]. The transition between these two regimes is continuously. One can define a transition criterion to separate these cases [30]:

$$\begin{aligned} z &\ll \frac{a^2}{\lambda} && \text{Fresnel regime} \\ z &\approx \frac{a^2}{\lambda} && \text{Transition zone} \\ z &\gg \frac{a^2}{\lambda} && \text{Fraunhofer regime} \end{aligned} \quad (2.15)$$

where a means in this case the lateral dimension of the aperture. In this work, Fraunhofer diffraction can be assumed justified by the rather long distance from the small

sample (micrometer dimensions) to the camera and the, in comparison, short wavelengths.

Assuming elastic scattering of photons during diffraction, each photon with the wave vector \mathbf{k}_i scatters at the aperture with the resulting new wavevector \mathbf{k}_s under the corresponding diffraction angle. Due to the energy conservation $|\mathbf{k}_i| = |\mathbf{k}_s|$, the outgoing wave vectors describing the so-called Ewald sphere [31] with radius $|\mathbf{k}_i|$. The momentum transfer vector can then defined by

$$\mathbf{q} = \mathbf{k}_i - \mathbf{k}_s \quad (2.16)$$

with the components q_x, q_y, q_z of the reciprocal space whereas the real-space coordinates x, y of the detector plane and the components of \mathbf{q} on the same plane are geometrically connected via

$$q_x = x/(z\lambda), q_y = y/(z\lambda) \quad (2.17)$$

2.2 Lensless imaging

Replacing the optics with numerical algorithms require slightly different considerations of the mechanisms happening. Geometrical optics, for instance, are not applicable anymore. The recovery of the phase, as the ground-laying problem to solve, engender several requirements considering e.g. limitations of objects in size and material or pixel size and number of the detector.

2.2.1 The phase problem

The previous section showed the connection between sample and its diffraction pattern in the far-field via Fourier transform. Due to the short wavelength in the XUV regime, one can consider this connection for most experimental setups. Optical sensors relying on the photo-effect such as charge coupled device (CCD) are sensitivity for the intensity of the incident light. The phase of the optical field is lost, preventing a simple inverse Fourier transform, and needs to be recovered forming the so-called

phase problem. To do so, the phase information has to be somehow encrypted in the intensity distribution on the detector to be calculable [22].

Due to the unavoidable pixelation of detectors, one pixel always average over a certain range of momentum transfer vectors, effectively filtering the diffraction pattern with a rectangular kernel. Here, the problem of sampling appears in a similar way as in signal reconstruction. The sampling has to sufficient "dense" [22], to not lose intensity information for phase reconstruction. These well-known Shannon theorem [32] states, that the sampling frequency has to be doubled the feature frequency to recover its phase. Applied to diffraction imaging, this criterion is known as oversampling of diffraction patterns. One can describe this criterion by imagine the pixelated detector plane as a system of coupled equations. Each of the N pixel is fully described by the two variables amplitude and phase, resulting in $2N$ variables. However, only the intensity and therefore the amplitude is known. To determine the equation system, one can oversample the amplitudes by a factor of 2 to reach $2N$ solutions. Practically, one has to take into account, that the sampling is not only determined by the pixelation of the sensor, but also to the characteristics of the measurement. A larger distance between object and detector increases the speckle size accordingly and increasing therefore the sampling under constant detector pixelation. Taking this into account, Miao et. al [33] described the oversampling degree to:

$$O = \frac{\lambda z}{ap} \quad (2.18)$$

with p as the width of a detector pixel and a as the aperture size of the object. Here O has to be larger than $\sqrt{2}$ (for 2D diffraction) to ensure a sufficient sampling. Nevertheless, solving the phase problem underlies some fundamental restrictions, which lead to ambiguities of several parameter: Complex conjugation, lateral translation, inversion and overall phase shifts are not covered by solving the phase problem [34].

2.2.2 Coherent Diffraction Imaging

Solving the mentioned phase problem with numerical frameworks is commonly referred to as coherent diffraction imaging and subsumes different techniques. Here, the basic reconstruction of a complex valued object shall briefly introduced [17]. As mentioned before, a simple inverse Fourier transform of a diffraction pattern $I(\mathbf{q})$ would end in an auto-correlation function of the corresponding object on the base of the Wiener-Khinchin theorem [35]. However, it can give a hint about the size of the object, since it has to be within its auto-correlation. Hence, this auto-correlation can be used to create a binary support function $S(\mathbf{r})$ between 0 and 1, limiting the extend of the reconstruction, shrink down the number of possible solutions and fulfilling the isolation constraint. Here, a threshold has to defined first, to select the non-zero area of S . Beside this, disc- or rectangular support function can also be used, but have to be adapted to the object size manually. Starting out of a random complex-valued field $\Psi_i(\mathbf{r})$ of iteration number i in the real space, multiplied with $S(\mathbf{r})$ and propagated to the detector plane in the reciprocal space via Fourier transform leading to a random complex-valued diffraction pattern

$$\Phi_i(\mathbf{q}) = \mathfrak{F}(\Psi_i(\mathbf{r})S(\mathbf{r})) \quad (2.19)$$

whereas \mathbf{q} and \mathbf{r} are the reciprocal and real space coordinates. Replacing the amplitude of $\Phi_i(\mathbf{q})$ with the measured amplitude $\sqrt{I(\mathbf{q})}$ via

$$\tilde{\Phi}_i(\mathbf{q}) = \sqrt{I(\mathbf{q})} \frac{\Phi_i(\mathbf{q})}{|\Phi_i(\mathbf{q})|} \quad (2.20)$$

and following inverse Fourier transform into the real space

$$\tilde{\Psi}_i(\mathbf{r}) = \mathfrak{F}^{-1}[\tilde{\Phi}_i(\mathbf{q})] \quad (2.21)$$

lead to a rough estimate of the object to reconstruct. At this point feedback- or update functions can be applied after a new iteration can start. The simplest one, the error-reduction (ER), sets all points excluded from the object via the support to

zero:

$$\tilde{\Psi}_{i+1}(\mathbf{r}) = \begin{cases} \tilde{\Psi}(\mathbf{r}) & S(\mathbf{r}) = 1 \\ 0 & S(\mathbf{r}) = 0 \end{cases} \quad (2.22)$$

At this point, more sophisticated update functions could be used to gain a feedback to the previous iterations. In this work, the hybrid input output (HIO) update function

$$\tilde{\Psi}_{i+1}(\mathbf{r}) = \begin{cases} \tilde{\Psi}_i(\mathbf{r}) & S(\mathbf{r}) = 1 \\ \tilde{\Psi}_i(\mathbf{r}) - \beta\Psi_i(\mathbf{r}) & S(\mathbf{r}) = 0 \end{cases} \quad (2.23)$$

with the feedback parameter β and the relaxed average alternating reflections (RAAR) [36] function

$$\tilde{\Psi}_{i+1}(\mathbf{r}) = \begin{cases} \tilde{\Psi}_i(\mathbf{r}) & S(\mathbf{r}) = 1 \\ \beta\Psi_i(\mathbf{r}) - (1 - 2\beta)\tilde{\Psi}_i(\mathbf{r}) & S(\mathbf{r}) = 0 \end{cases} \quad (2.24)$$

are used beside ER. For a detailed discription of update function, see [20]. Further constraints can be applied, e.g the positivity or modulus of the object field. This constraint reduce the number of equations to solve and can enhance the convergence to a solution. On the other side, further constraints restrict the diversity of the outcome and can disturb the algorithm, if the constraint is not matching the experimental conditions. From the last equation on, a new iteration could start.

To define a runtime, a termination criterion has to be implemented. Therefore the sum-square-error between the measured diffraction pattern and the reconstructed can be determined [17]:

$$E_i = \sqrt{\frac{\sum_{\mathbf{q}} (|\Phi_i(\mathbf{q})|^2 - I(\mathbf{q}))}{\sum_{\mathbf{q}} (I(\mathbf{q}))}} \quad (2.25)$$

2.2.3 Ptychography

A classical reconstruction via coherent diffraction imaging (CDI) needs constraints like non periodical, isolated objects [37]. To reconstruct objects larger than the spot size, a scanning method is required. To overcome the oversampling requirement, it is convenient to consider redundant data to over-determine the phase retrieval

problem which is known as problem of intersecting constraints. Therefore the objects has to be scanned with overlapping scan points. First introduced in the 1970s, it required knowledge about the exact properties of the incident beam (probe) to reconstruct the object image via the set of captured diffraction patterns. The development of the so-called "Wigner deconvolution", which was able to retrieve object and probe with the constraint, that the shift between the images have to be as fine as the required resolution [23], enables for the first time a reconstruction with vague knowledge about the incident wavefront. Shortly after, Maiden and Rodenburg [38] developed an advanced ptychographic algorithm called extended ptychographic iterative engine (ePie) that was able to retrieve the probe and object from a given dataset with a loosened requirement of the probe position and shape.

To retrieve the object and probe via ePIE the following has to be considered: The captured intensities $I_j(\mathbf{q})$ for a shift \mathbf{R}_j at position j in the data-set at the detector plane can be written as the modulo squared from the complex field $\Psi_j(\mathbf{q})$, which is generated via a complex Hadamard product² of the object field $O(\mathbf{r})$ and its shifted by \mathbf{R}_j illuminating probe field $P(\mathbf{r} - \mathbf{R}_j)$ and propagated via a Fourier transformation:

$$I_j = |\Psi_j(\mathbf{q})|^2 = |\mathfrak{F}[O(\mathbf{r})P(\mathbf{r} - \mathbf{R}_j)]|^2 \quad (2.26)$$

The task of a ptychographic algorithm is to determine the phases of Ψ_j for each j to calculate $O(\mathbf{r})$ and $P(\mathbf{r} - \mathbf{R}_j)$, that have to satisfy Eq. 2.26. An algorithm searching for a solution of Eq. 2.26 uses the redundancy of data-sets to converge. The ePie algorithm, applied in this work, uses update functions similar to the HIO-algorithm to recover the complex field in the object plane. Additionally to non-scanning algorithms reconstructing only the sample, it uses a coupling of fields to recover also the probe field. At first, initial fields are required as a starting condition like in CDI. Therefore, a random complex-valued field support function related to the size of the real illumination serve as the starting object and probe field. Note, that in Ptychography, the support has switched from object to illumination field. These both fields

²This is valid in case of optically thin apertures

getting combined as in Eq.2.26 to form an so called exit field Ψ_j [38]:

$$\Psi_{j,i}(\mathbf{r}) = O_i(\mathbf{r})P_i(\mathbf{r} - \mathbf{R}_j) \quad (2.27)$$

This field is propagated to the detector plane

$$\Phi_{j,i}(\mathbf{q}) = \mathfrak{F}[\Psi_{j,i}(\mathbf{r})] \quad (2.28)$$

where the phases are kept and the measured amplitudes $\sqrt{I_j(\mathbf{q})}$ are enforced.

$$\tilde{\Phi}_{j,i}(\mathbf{q}) = \sqrt{I_j(\mathbf{q})} \frac{\Phi_{j,i}(\mathbf{q})}{|\Phi_{j,i}(\mathbf{q})|} \quad (2.29)$$

This new exit field is propagated back to the object plane by an inverse Fourier transform:

$$\tilde{\Psi}_{j,i}(\mathbf{r}) = \mathfrak{F}^{-1}[\tilde{\Phi}_{j,i}(\mathbf{q})] \quad (2.30)$$

The object and probe fields get transformed via update functions:

$$O_{j,i+1}(\mathbf{r}) = O_{j,i}(\mathbf{r}) + \alpha \frac{P_j^+(\mathbf{r} - \mathbf{R}_j)}{|P_j(\mathbf{r} - \mathbf{R}_j)|_{\max}^2} (\tilde{\Psi}_{j,i}(\mathbf{r}) - \Psi_{j,i}(\mathbf{r})) \quad (2.31)$$

$$P_{j,i+1}(\mathbf{r}) = P_{j,i}(\mathbf{r}) + \beta \frac{O_j^+(\mathbf{r} - \mathbf{R}_j)}{|O_j(\mathbf{r} - \mathbf{R}_j)|_{\max}^2} (\tilde{\Psi}_{j,i}(\mathbf{r}) - \Psi_{j,i}(\mathbf{r})) \quad (2.32)$$

whereas the constants α and β describes the coupling strength between them. After the application of update functions, the next positions j has to be calculated before a new iteration can start.

2.2.4 Phase retrieval transfer function

As shown in the previous chapter, the highest resolution achievable with classical diffraction imaging experiments are determined by the highest recordable momentum q_{\max} , due to the nature of the Fourier transform. This is in best case a matter of the detector size. Due to the limited dynamic range of the detector, unavoidable

noise and the fast decrease of the diffraction signal in dependence of q , high momentum signal will not be captured effectively. During the reconstruction, weak signals will not be recognized and limits therefore the accessible resolution. Solving the phase problem will give access to the signals, which contributes to the reconstruction. To quantify a physical valid q_{\max} , the reconstructed diffraction pattern has to be compared with the measured one to access the transferred, and therefore valid, signal:

$$\text{PRTF}(\mathbf{q}) = \frac{|\Phi(\mathbf{q})|}{\sqrt{I(\mathbf{q})}} = \frac{|\mathfrak{F}(\Psi(\mathbf{q}))|}{\sqrt{I(\mathbf{q})}} \quad (2.33)$$

This so-called phase retrieval transfer function (PRTF) [39] compare the amplitude of the measured diffraction pattern $\sqrt{I(\mathbf{q})}$ with the reconstructed one $|\Psi(\mathbf{q})|$. Usually the PRTF will be plotted in dependence of the radial momentum $q_r = |\mathbf{q}|$, therefore $\text{PRTF}(\mathbf{q})$ will be averaged over shells of constant $|\mathbf{q}|$. The maximum expectable resolution depends now on the underlying resolution criterion. In this work, the FWHM criterion is used, which sets q_{\max} at half-maximum of $\text{PRTF}(q_r)$.

2.2.5 Resolution vs. exposure

To obtain high resolution in diffraction imaging, recording of high momentum signals is crucial as mentioned before. The diffracted signal intensity quickly drops with the diffraction angle, respective high momentum. High resolution diffraction images therefore demand high doses of radiation impacting the specimen. Howells et al. [40] showed, that the required dose scales with the inverse fourth power of the resolution. Small improvements therefore demands disproportionately high flux. Depending on energy and the radiation resistance of the sample, this issue causes alteration of the specimens. Reducing the dose is mostly hard to reach, hence, the recording of the pattern therefore has to be as fast as possible. In this case, the sample receives the same overall dose, but the alteration is slower than the recording. This so-called diffraction before destruction was introduced by Chapman et al. [41] and is a common procedure imaging proteins with high resolution. Another approach to imaging sensitive specimens lensless and without destroying them arisen out of the Hanbury Brown and Twiss (HBT) effect [42]. Correlations of light can be

used to image an object, never been in contact with the light, hitting the detector. Correlating light fields can be used to separate the object-illuminating light from the detector hitting radiation, whereas the intensity ratio is nearly freely shiftable. This so-called ghost- or quantum imaging allows imaging of very sensitive samples down to the X-ray regime [43].

2.3 XUV radiation sources

The procedures discussed in this work benefits from the extraordinary characteristics of modern XUV radiation sources. Here, three concepts shall briefly discussed, which are well-implemented in current research and fulfill different requirements regarding flux, coherence and energy.

2.3.1 Synchrotron sources

Developed in 50th of the last century out of the cyclotron, synchrotrons, as a special kind of particle accelerator, use synchronized electric fields in a ring-shaped cavity resonator to accelerate particles to relativistic speeds. They can increase the kinetic energy of various types of charge particles and are capable to store them, acting as a storage ring. A special application of synchrotrons is the usage as high brilliance light sources using synchrotron-radiation emitted from electrons. Here, electrons accelerated by the synchrotron are guided into an stacked magnetic structure with alternating polarities called undulators. Relativistic electrons, perpendicular accelerated in undulators emits radiation in tangential direction due to Lorentz contraction. By adapting the electron speed with the undulator period, a coherent stacking of photons are realized resulting in a partially spatial coherent bunch of photons. The spectrum is emitted in peaks from the terahertz to X-ray regime due to interfering photons [44].

2.3.2 High Harmonic Generation

The mentioned above synchrotron sources provide a high flux but suffer from accessibility due to their size and operating costs. To overcome these restrictions, the development of table-top sources is of paramount importance. One concept discovered in 1987 [45, 46] relies on highly nonlinear interaction between the electrical field induced by a high-intensity femtosecond laser and a noble gas resulting in the emission of various multiple harmonics of the driving laser field. This so-called high harmonic generation (HHG) can be described by the 3-step-model [47]:

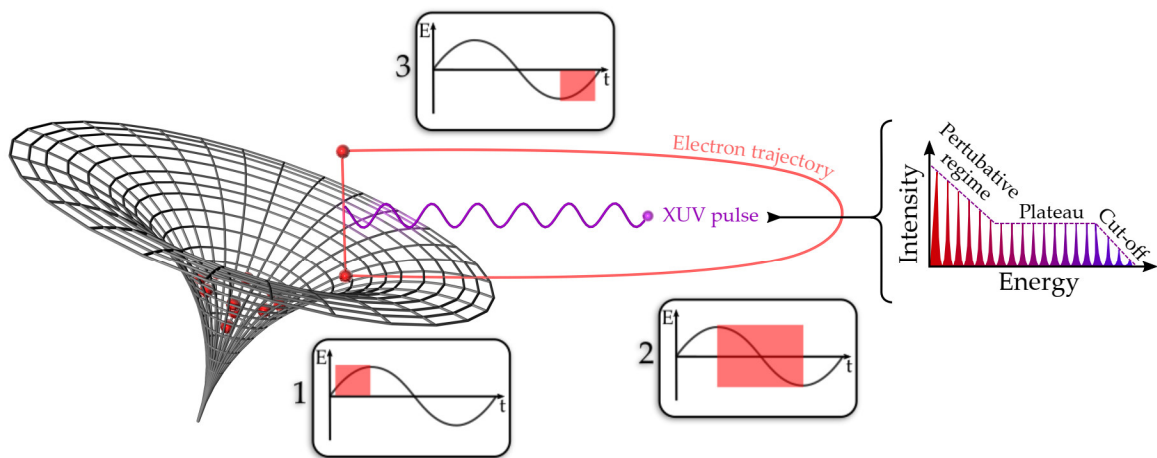


FIGURE 2.4: Principle of high harmonic generation: An atomic potential is tilted by the optical field, enabling an electron to exit the atomic boundaries to gain kinetic energy and emit radiation during recombination.

1. The incident electric field shifts the atomic potential during the first half period enabling an electron to leave the atom via different ionization mechanisms, despite the ionization-insufficient energy of the incident photon. Here, the corresponding ionization can be either field ionization, if the electric field is high enough to negotiate the binding or tunnel ionization with moderate fields decreasing the binding energy. Further separation between the two cases can be determined by the Keldysh parameter [48]

$$\gamma = \sqrt{\frac{U_i}{2U_p}} = \sqrt{\frac{U_i 4m_e \omega^2}{2e^2 E_0^2}} \quad (2.34)$$

with the ionization potential U_i dependent on the chosen gas and the ponderomotive potential U_p describing the average kinetic energy of the electron in a oscillating electric field with the amplitude E_0 and the frequency ω . One can assume multi-photon ionization, if γ is way larger than 1, meaning low amplitudes and short wavelength. $\gamma \ll 1$ however transits the mechanism towards tunnel ionization.

2. The freed electron gets accelerated by the electric field in a certain direction following classical electrodynamics and neglecting the influence of outer coulomb forces. With the end of the half period, the electron experience acceleration into the opposing direction gathering more kinetic energy.
3. By approaching the mother nucleus, the electron can recombine with a certain probability under bremsstrahlung-like emission of highly energetic radiation all the way down to the soft X-ray regime. The maximum photon energy emitted is defined by

$$E_{\max} = U_i + 3.17U_p \quad (2.35)$$

Driving this system to shorter wavelength output therefore requires either higher intensities or longer wavelengths at the input, which sounds contra-intuitive at a first glimpse, but becomes explainable with the electrons inertia. However, increasing the intensity increases the influence of the magnetic component of the driving field, ending in missing the nucleus due to Lorentz force and defining a saturation intensity [49].

An important characteristic of high harmonic radiation is the line spectrum only containing odd harmonics of the driving field starting with the perturbative regime with constantly decreasing intensities, following with a plateau-like regime, where the intensities of harmonics remain nearly constant until the emission rapidly stops at the cut-off wavelength. Due to the increased ionization probability with high intensities, the generated XUV pulse is significant shorter than the driving pulse and

enables attosecond pulse generation [47]. The coherent mechanism of HHG leading to partial conservation of beam characteristics of the driving laser regarding spatial coherence and divergence.

2.3.3 Laser-Plasma sources

Lowering the requirement for high intensity driving pulses with ultrashort duration down to moderate intensities and pulse durations in the nano- to picosecond regime, enabling different ionization mechanisms on different timescales. Focusing of such "long"-term pulses into a gas is followed by ionization via multi-photon absorption or tunneling (see equation 2.34) and heating, rising the electron temperature [50]. Here, many ionization states become possible roughly controllable with the induced energy. The isotropic ionization and recombination processes resulting in nearly incoherent isotropic radiation in 4π despite the coherent driving laser. Due to the excitation of intrashell electrons and corresponding e.g. Lyman alpha (L_{α}) transitions, emissions down to several hundred electronvolts become possible with high flux. However utilizing this kind of radiation source require collecting and focussing optics.

Another application for laser-plasma sources is the laser-like operation using amplified spontaneous emission (ASE) forming a SXRL. There, population inversion can be reached in the plasma via e.g. collisional pumping with additional laser sources [51, 52]. Random spontaneous emission occurring in the plasma can trigger stimulated emission of the neighboring excited atoms resulting in an effective amplification without the cavity, as used in regular laser systems, and a partially spatial coherent emission.

2.3.4 Comparison

The here presented and used XUV sources have different characteristics regarding flux, energy, stability, etc and are therefore only available for certain applications. Fig. 2.5 shows a comparison of the brilliance between the explained principles. The brilliance is a measure for the flux per solid angle (divergence) within a certain bandwidth limit and a suitable quantity to estimate e.g. exposure times. Whereas HHG-based sources cover a relatively large range in the lower energy regime with low to moderate brilliance, higher energies are relatively simple to reach by laser-plasma sources. The highest fluxes are still covered by large synchrotron facilities. Petra III shall here be used as a high brilliance example.

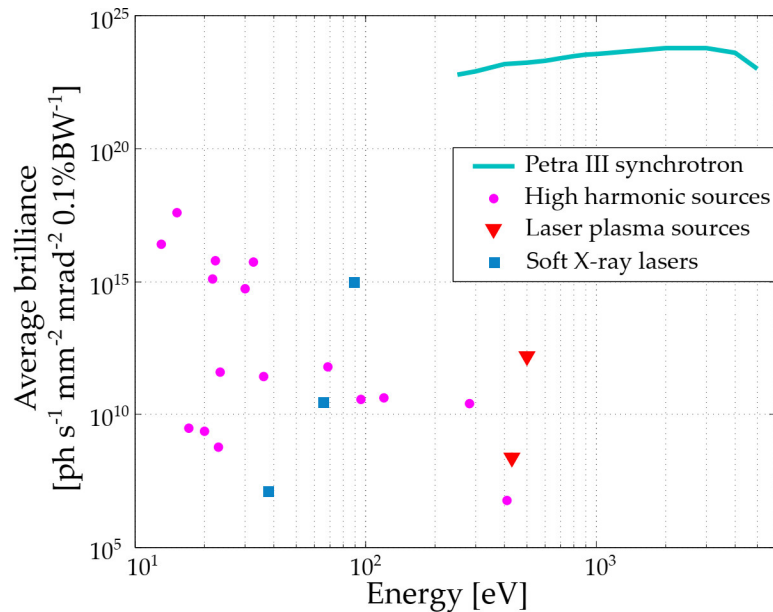


FIGURE 2.5: Average brilliance comparison of several XUV sources [53, 54] based on the principles used in this work. Different principles of XUV generation cover different regimes of energy-brilliance respective energy-flux combinations. Therefore, the sources must be carefully chosen for the desired imaging method and sample.

Chapter 3

Reflection mode CDI at high photon energies

XUV imaging in material-specific spectral regimes or so-called windows allows tuning the image contrast to its optimum reliant on the material composition. Two windows of specific interest are the silicon window [14, 55], and the water window [56, 57] as shown in Fig. 3.1:

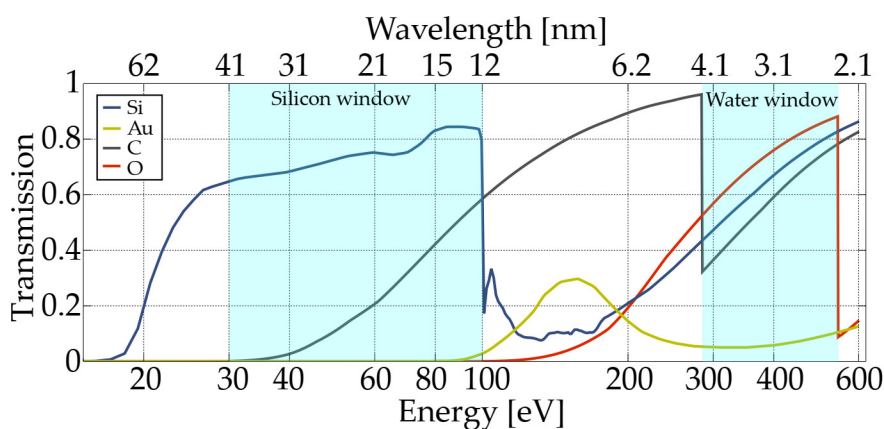


FIGURE 3.1: Transmission window of different materials for 10 μm thickness. Marked are the silicon window between 30 and 100 eV and the water window between 282 and 533 eV.

The silicon window between 30 and 100 eV (40 to 12 nm), where most of the materials, used in metal-oxide semiconductor (MOS) technology, are mainly absorbing, is of special interest to semiconductor applications. Absorbing structures embedded in silicon generate high contrast images allowing precision metrology [58] and material diagnostics, such as damage tests [59] or local current-induced electromigration observations [60]. The high transparency of silicon enables the observer to gather information about buried layers, thus, allowing depth-resolved measurements e.g. using coherence tomography [14]. CDI angular tomography is able to resolve 3D structures by combining reconstructed images under various angle of

incidence (AOI) [55]. CDI based techniques are often applied in transmission geometry due to the more simple setup and the fast pre-processing of diffraction data (see Appendix A). Therefore only well-prepared samples with rather thin substrates are suitable for this procedure.

In the following section, a buried gold layer in silicon is analyzed in reflection geometry under near-normal incidence to test diffraction imaging concerning more lifelike samples. Additionally, the reflection geometry allows the reconstruction of surface morphologies and therefore roughness measurements of hidden structures. However, reflective diffraction imaging poses other challenges for the experimental setup and the reconstruction. Due to the forced longer distance between sample and detector, the decreasing numerical aperture (NA) leading to a lowered resolution in comparison to transmission geometries. Additionally to the curvature correction, the thickness and the tilted plane of the sample imposes skewed diffraction patterns, which must be corrected first (see Appendix A).

Due to the limitations of the used synchrotron source, the diffraction pattern was obtained with 290 eV photon energy, which belongs to the water window but also ensures high transmission for silicon, compared to gold. However, the emitted synchrotron radiation is well suited for this kind of experiments due to the stable beam and well-controllable parameters such as energy, beam radius and flux.

3.1 Experimental setup

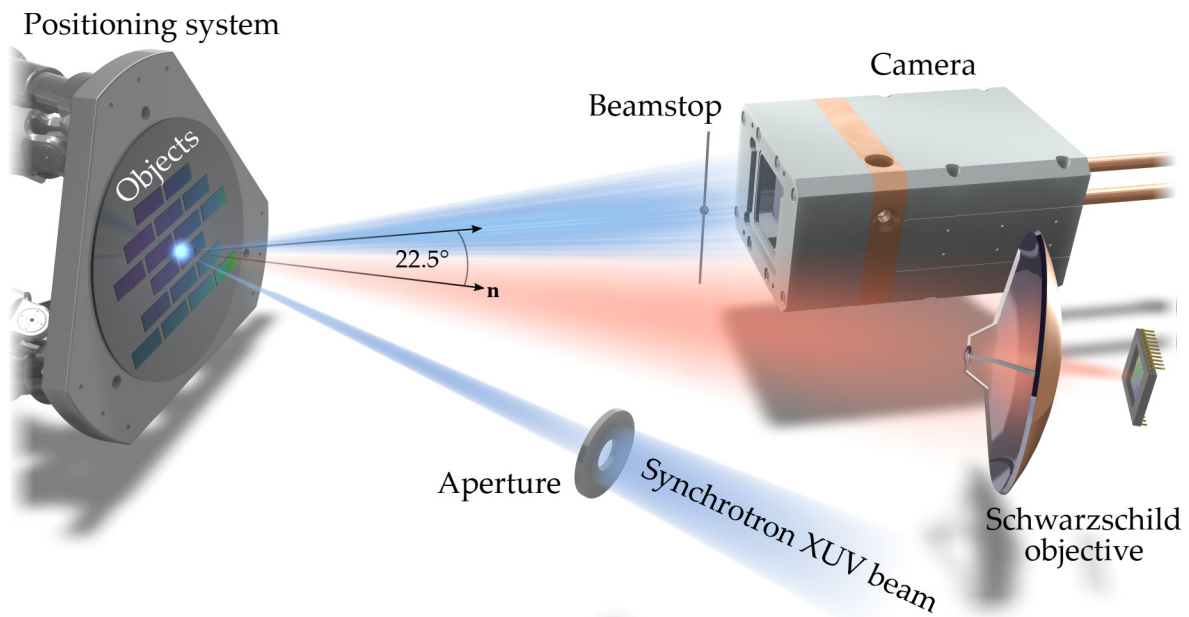


FIGURE 3.2: Reflection mode CDI setup. The variable energy XUV beam passes an aperture to increase the spatial coherence before it illuminates the sample, mounted on a 9 degrees of freedom (DOF) positioning system under 22.5° AOI. A Schwarzschild objective allows a direct view of the sample surface and enables the precise positioning of the XUV focus. The scattered light passes an absorbing beamstop to avoid oversaturation of the CCD by zero-order scattering

The experiment was performed at the variable polarization XUV beamline P04 at the *PETRA III* synchrotron at DESY, Hamburg. The beamline provides a variable energy from 250 to 3000 eV with a total flux greater than $1 \times 10^{12} \text{ ph s}^{-1}$. The variable polarization was not used and fixed to horizontal. Without additional optics, a spot size of $50 \mu\text{m}$ in diameter (FWHM) is guaranteed and used for this experiment. The spatial coherence of P04 is globally determined to 35% at $100 \mu\text{m}$ slit width at entrance [61]. This slit opening was chosen regarding the high flux mentioned above. The resolving power then decreased to $\sim 1 \times 10^4$ at 250 eV. To enhance spatial coherence further and tune a sharp, flat-top-like illumination profile, a pinhole of $50 \mu\text{m}$ in diameter was placed in 20 cm distance to the sample resulting in a focus size of $30 \mu\text{m}$ (FWHM). The sample itself was mounted on a Hexapod with nine DOF to freely shift the sample for different AOI. Fiber interferometers provide sub 100 nm closed-loop positioning in every direction. Matching the vacuum requirements of *PETRA III*, the imaging system is enveloped by a vacuum chamber with

different angled ports. During the beamtime, different experiments with different geometries were performed.

This work only availed oneself of reflection geometry under 22.5° AOI as shown in Fig. 3.2. Here, the scattered light hits an absorbing beamstop closely attached to the camera. This procedure eliminated the oversaturation of the camera due to the high intensity zero-diffraction order. The in-vacuum camera¹ was mounted onto a shiftable balcony within the chamber to increase the NA. Due to the Hexapod setup and the pinhole mount, the closest distance between sample and camera was 230 mm, resulting in a NA of 0.06 and an Abbe-limit of approx. 40 nm for the lower limit of P04 (250 eV). The sample consists of different buried gold structures, sorted by lateral size on nine rectangular fields as seen in Fig. 3.2. Due to processing variations, the fields were double applied onto a 4" silicon wafer to ensure redundancy. A Schwarzschild objective for the optical spectral range enables a coarse positioning and low contrast observation of the sample. Due to straylight, simultaneously XUV and VIS observation was not possible.

3.2 Reflection-mode CDI of a buried sample

A 15 nm thick gold star-shaped structure (Siemens star), buried under 120 nm silicon (see Fig. 3.3) was examined in reflection mode with 290 eV photon energy. The chosen energy was a trade-off between beam stability, flux and transmission of silicon. The top layer in this energy range is still transparent with a transmission of 0.4^2 for the used layer height.

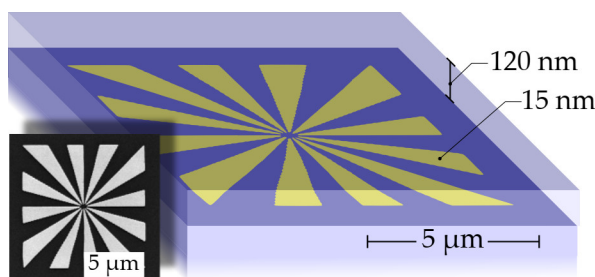


FIGURE 3.3: Model of the buried sample structure. A 15 nm thick star-shaped gold layer is placed under 120 nm mono-crystalline silicon on a $200\ \mu\text{m}$ silicon substrate. The overall size of the structure is $8.8 \times 8.8\ \mu\text{m}^2$. The inset shows a SEM image of the unburied gold layer.

¹Princeton Instruments PiMTE 4k

²CXRO X-ray database: Transmission of crystalline silicon

The incident flux on the sample could be determined to $3 \times 10^{11} \text{ ph s}^{-1}$ with a calibrated photodiode, which leads to an expected total scattered flux of $2.4 \times 10^6 \text{ ph s}^{-1}$, considering a gold reflection factor of 5×10^{-5} for the given energy and AIO³. This rather low signal required relatively long exposure times of 120 s.

Due to the interfering reflex of the silicon surface, a diffraction pattern of the structure-free vicinity was captured and subtracted from the actual measurement. Despite this, the reflected and scattered signal from the object may be still interfered by signals emerging from internal reflections at the surface. Internal scattered light could modulate the diffraction pattern, therefore a simulated diffraction pattern was generated using the “k_mask” code (see Appendix B) and compared to the measured and pre-processed one to get an impression of possible interference fringes.

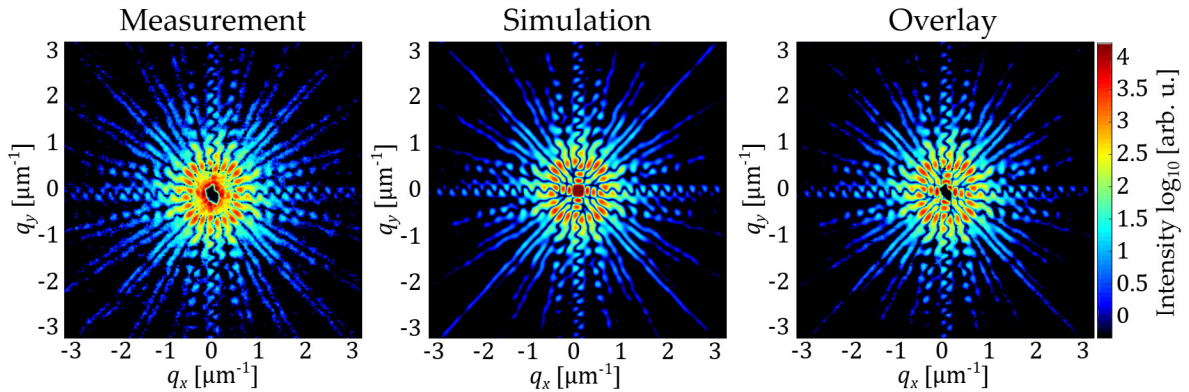


FIGURE 3.4: Comparison between measured and simulated diffraction pattern of the buried Siemens star in reflection mode. The momentum was limited to $\pm 3 \mu\text{m}^{-1}$, neglecting higher spatial frequencies with low amplitude for the comparison. Apparently, the wavy fringe structure of the measured data corresponds well with the simulation. The overlay, as a Hadamard product of both, conserve the fringes, indicate neglectible intra-layer interference between structure and surface.

Fig. 3.4 shows the direct comparison between the measured diffraction pattern of the buried Siemens star and the simulated one. The fringes only differ in the central region around the beamstop. This modulation appears as diffraction directly from the beamstop. Higher spatial frequencies over $0.5 \mu\text{m}^{-1}$ appear unchanged. The overlay in Fig. 3.4 show the Hadamard product of the two pattern. Differences between them should appear as blurred out or vanishing patterns. Due to the high similarity, surface interference can be assumed as negligible.

³CXRO X-ray database: Reflection of thick gold

The reconstruction of the buried object in Fig. 3.5 reveal the complex-valued Siemens star pattern with an edge resolution (10/90) of 179 nm and a possible PRTF resolution of 330 nm (FWHM). Here, the PRTF signal is below 0.25, therefore a different criterion would lead to higher a resolution (e.g. 110 nm for 1/e criterion), explaining the deviance between the edge- and PRTF resolution.

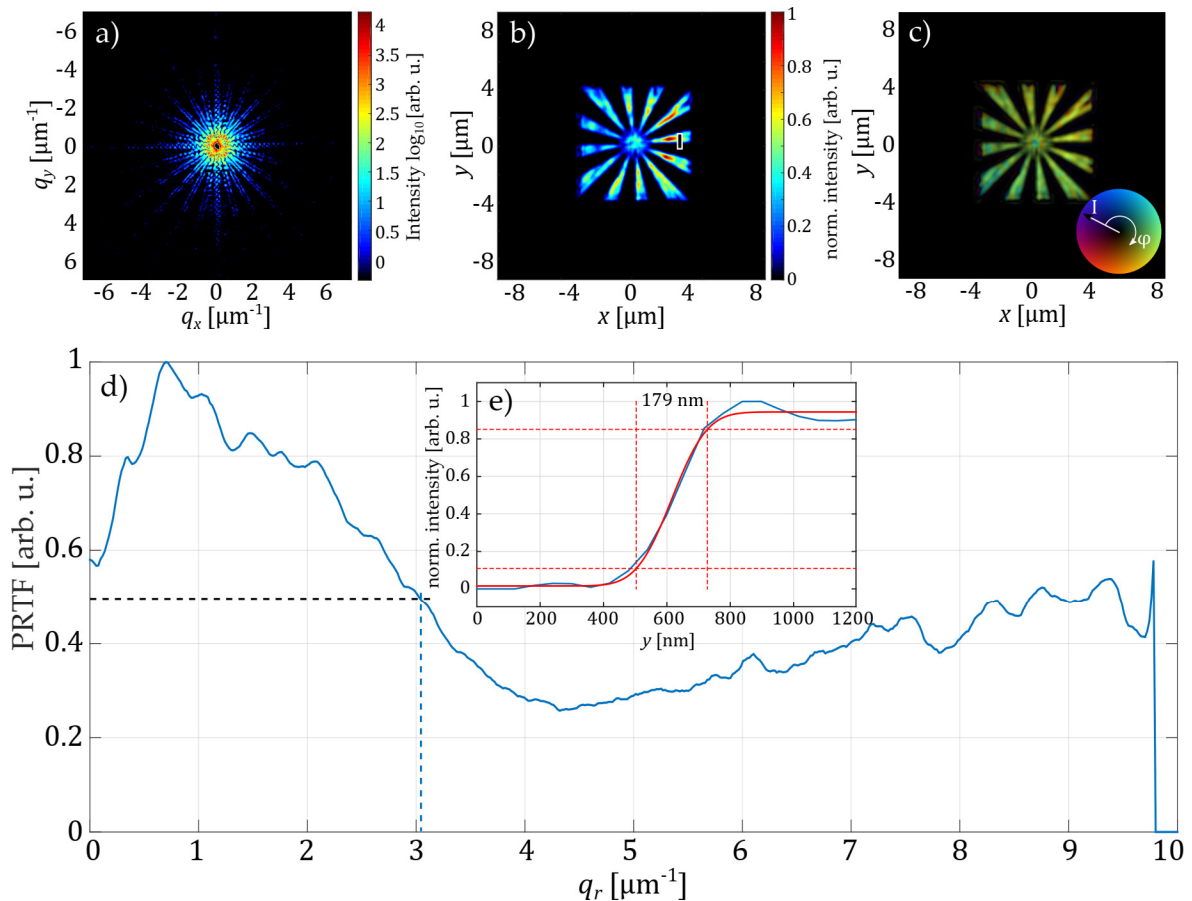


FIGURE 3.5: Reconstruction of the buried sample. The diffraction signal of the pre-processed diffraction pattern in a) nearly reaches the edges up to $6 \mu\text{m}^{-1}$ with a maximum count of $\sim 40\,000$ in 120 s. The reconstructed intensity (b) and complex-valued object function (c) show a dome-like artifact in the center, where the structures are smaller than the resolution limit. The PRTF (d), under usage of the FWHM criterion, set the resolution to 330 nm. The PRTF is always above 0.2 and increases again to higher momenta. Therefore, the PRTF is not sufficient for determining the resolution, which is in agreement with a simple edge resolution test in e) (179 nm).

Reconstruction parameter			
Update function:	ER + RAAR, $\beta = 0.9$	Support:	Static, disc, $12 \mu\text{m}$
Iterations:	1000	Constraints:	Positivity

The inner part of the star pattern, where the structure size undergo 100 nm, cannot be resolved anymore and leads to an artificial dome-like structure. Using this behavior, one can derive a third criterion in the style of Horstmeyer et al. [62] for

determining the resolution: The resolution limit is reached, if the dominant periodic structures are not separable and therefore not countable anymore (periodicity criterion). The Siemens star consists of 12 "arms". Deriving a circular profile around the center of the Siemens star shown in Fig. 3.6, allows to count the arms for every radius. The resolution limit is reached, if the arms are not separable anymore. This criterion is way more robust to misreadings through structural effects in comparison to e.g. FWHM or $1/e$ of PRTF or 10/90-edge, but is only applicable to structures, allowing this technique (e.g. rotation symmetric and smoothly increasing size). For the analyzed structure the radius, where the reconstruction begins to dissolve and the arms are not countable anymore, starts at approx. 650 nm. To extract the corresponding structure size, knowledge about the object is necessary. The width of the arms increase with the radius and represents therefore the smallest lateral structure resolvable for a measured minimal radius. In this case, a radius of 650 nm corresponds to a width of 160 nm, which claims the resolution limit and is comparable to previous limits (10/90-edge: 179 nm, PRTF: 110 ($1/e$) to 330 nm (FWHM)).

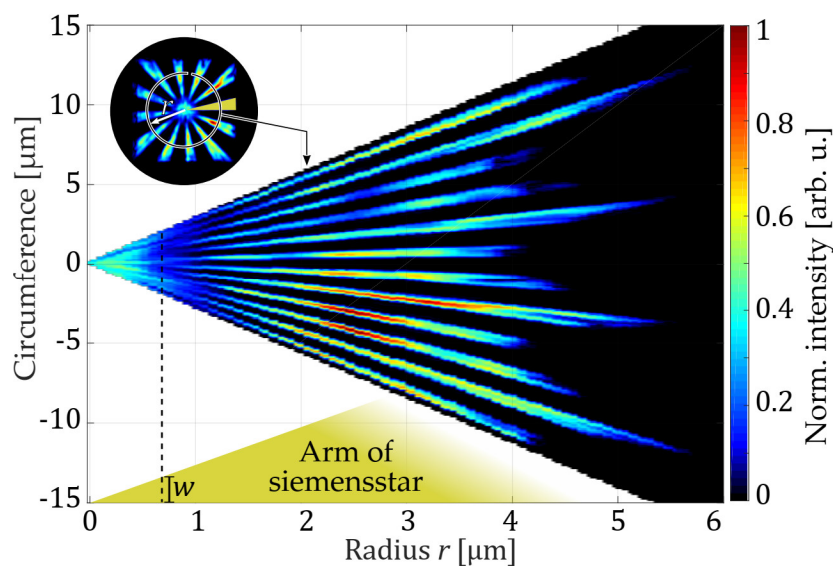


FIGURE 3.6: Circumference profiles of circles with increasing radius on the reconstructed Siemens star. The 12 "arms" start to vanish regarding to [62] at approx. 650 nm radius corresponding to 160 nm smallest resolvable width w of an arm, marked in yellow in the inset.

The complex-valued reconstruction allows a determination of the relative height of the object. Therefore, the phases Φ must be transitioned to the corresponding height h under consideration of the AOI α via

$$h = \frac{\Phi \lambda \cos(\alpha)}{4\pi} \quad (3.1)$$

which follows directly of the Bragg equation. However, the here investigated object was buried under a certain layer of silicon, which can be neglected, if the thickness of these cover layer can be considered as constant. The silicon was applied via chemical vapor deposition. Due to the small FOV ($8.8 \times 8.8 \mu\text{m}^{-2}$), it is permissible to assume a constant thickness in these area. The calculated height, shown in Fig. 3.7, reveals mainly the surface roughness of the buried star to 0.37 nm RMS. Due to the small wavelength, the whole procedure is highly sensitive to optical path differences. This is also the reason why the reconstruction can only show the relative height. Path differences, larger than the wavelength lead to phase jumps and therefore to ambiguous solutions [63].

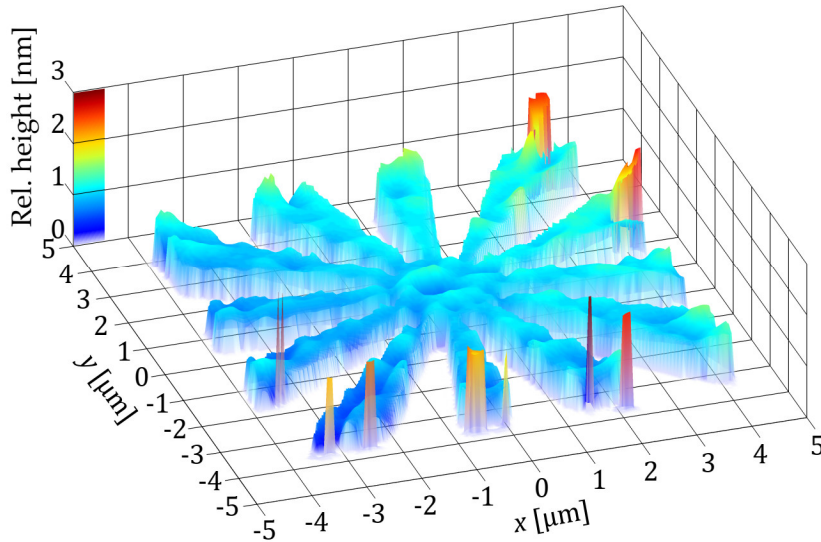


FIGURE 3.7: Reconstructed relative height profile of the Siemens star sample. Using the complex-valued reconstruction, shown in Fig. 3.5, the relative height could be retrieved. Note, that the total height from the ground is not meaningful here due to possible phase jumps.

3.3 Summary

Phase resolved lensless imaging of buried specimen in the silicon window is of crucial interest in semiconductor research and industry. Here, CDI allows in principle single-shot insights in already fully processed dies with nano-scale resolution and material contrast. The use of reflection geometries enables additionally the reconstruction of layer morphologies. Here, a gold structure, buried in a silicon matrix, could be retrieved in near-normal incidence with high resolution. The phase retrieval allowed inferences about relative heights in the object plane. In this way, the roughness of the buried layer could be determined to 0.37 nm RMS and shows that CDI has the capability for non-invasive nano-scale roughness measurements of buried structures. Roughness measurements of buried layers were already done with transmission electron diffraction [64] or tomography [65] but require a transparent substrate. Coherence Scanning interferometry is also capable of measuring the roughness of buried layers [66], but suffer from missing lateral resolution, as it is defined by the focal spot size. Therefore, reflection mode CDI of buried layers for roughness measurements in the XUV with high lateral resolution is presented here for the first time to the best of one's knowledge. However, these technique is limited by the wavelength due to ambiguous solutions caused by phase jumps. To get rid of these ambiguities, well-defined reference layers can be implemented to get a more precise layer allocation comparable to coherence tomography [14]. Tomographic techniques such as ptychographic X-ray tomography [55] allow full 3D reconstructions but call out for a more sophisticated level of pre-processing, e.g. cutting the die. A future application could benefit from reconstructions with different AOIs of the same specimen to narrow down the number of possible solutions in height. In this way, a full 3D surface measurement would be possible. Finally, it is worth to say that these processes could be implemented in-situ. Hence, this enables structural measurements e.g. during layer constructions via chemical vapor deposition.

Chapter 4

Imaging with a laser-driven soft X-ray source in the water-window

Imaging in the water window exploits high contrast pictures of biological samples as mentioned in chapter 3. The main requirement of any microscopic technique, whether lensless or not, is a suitable source. The used source in the previous chapter was the Synchrotron *PETRA III* beamline *P04* with excellent beam quantities but with the huge withdraw of limited and costly accessibility and a strict location. A compact source with comparable parameter in the high energy spectral range is desirable for lab-scale research but difficult to implement. A high-flux HHG based source emitting in the water window as a possible candidate is hard to achieve due to the limited cut-off frequency and the low conversion efficiency. A more convenient technique for high yields with energies above 200 eV is recombination-based emission of laser-excited liquid targets [67]. Beside the yield, this technique offers high repetition rates with low debris emission preserving the focusing optics [68]. Using the Lyman-alpha Ly_α transition of a hydrogen-like laser-excited nitrogen jet, the emitted wavelength can be shifted to the high energy end of the water window, where the carbon-oxygen contrast maximizes. In the present chapter, this promising approach for compact XUV sources will be analyzed with regard to lensless imaging. The source, constructed and operated at the Berlin Laboratory for innovative X-ray Technologies *BLiX*, is typically used for zone-plate based imaging with nano-scale resolutions, which will be investigated in the following section. Human kidney cells, labeled with iron-oxide spheres, will be directly imaged to gain information

about the resolving power of the setup and the possibility to determine the exact position of the spheres, coupled to certain cell receptors. Imaging with zone-plates requires an incoherent or partially coherent source to direct image the object onto a 2D detector. Lensless imaging however, calling out for the highest coherence possible. This discrepancy seems incongruous at a first glimpse, though beam shaping allow to bridge these gap. But first, the raw parameter of the emitting plasma has to be confined. Therefore a procedure was developed, which allows the reconstruction of important beam and source parameters using only a single long exposed diffraction pattern. The simplicity of capturing the data makes the procedure suitable for most kind of sources, despite low flux.

4.1 Experimental setup

The radiation source itself consists of a dense nitrogen plasma, pumped with a sub-nanosecond laser. Therefore a liquid nitrogen jet of few tens of μm thickness and a speed of $\sim 100\text{ m s}^{-1}$ is directed from the top into a vacuum chamber. A perpendicular directed laser beam with 450 ps pulse duration and 130 W average power at 1064 nm wavelength and 1.3 kHz repetition rate excites the nitrogen to hydrogen- and helium-like states, emitting at 2.478 and 2.879 nm. For a further description of the laser system and beam shaping, see [69]. While electrically gas discharge plasma sources show a dominant He_α emission at 2.879 nm [70, 71], laser based plasma sources with high repetition rates emit more efficiently at the hydrogen-like Ly_α line at 2.478 nm with $\lambda/\Delta\lambda = 1000$ [72]. Nevertheless, the nearby He_α line is still emitted but not desired. A beamstop, as seen in Fig. 4.1, blocks the direct radiated emission of the plasma source, whereas the Ly_α line can pass the beamstop via reflection at a Cr/V multilayer mirror of 54 mm diameter and 350 mm radius of curvature with a reflectivity of 0.4 % resulting in a conical illumination with a hollow core. The mirror images the plasma source with a magnification of 2 onto the sample plane, resulting in a spot size of $\sim 40\ \mu\text{m}$. Filters of different materials can be applied between the beamstop and the sample plane for blocking straylight of the He_α line and scattered

infrared radiation. The optional zone-plate allows direct imaging of samples and has to be placed a few hundred micrometer behind the sample.

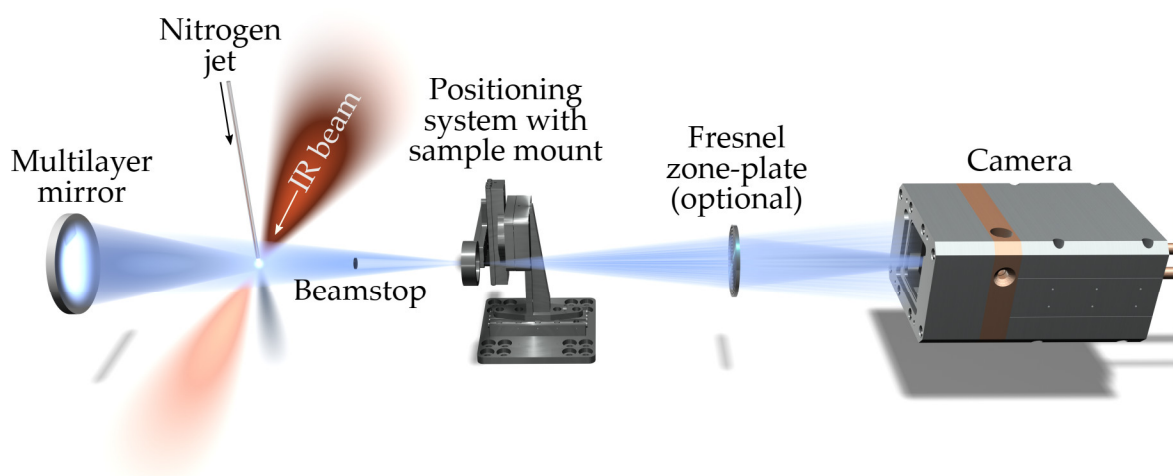


FIGURE 4.1: Schematic of the BliX beamline. 450 ps short 1064 nm infrared pulses with an average power of 130 W are focused onto a perpendicular flowing liquid nitrogen jet. The 4π emitted 2.48 nm (Ly_α transition) radiation gets captured by a Cr/V multilayer mirror and focused down to a 40 μm spot at the samples position. The additionally emitted He_α line is blocked by a beam block. The optional Fresnel zone-plate allows direct imaging of arbitrary transmission samples.

4.2 Labeled bio-imaging with zone-plates

The spectral range of 533 to 282 eV (4.4 to 2.3 nm) wavelength, the so-called water window, enables high contrast bio-imaging due to high absorption of carbon below 4.4 nm (K-edge) and high transmission of oxygen above 2.3 nm (K-edge). Water, with oxygen as the main scatterer, is therefore nearly transparent, whereas carbon-based matter (organic molecules) is highly absorbing. The high flux at the energetic upper end of the water window suits this source well for biological investigations on the nano-scale. The contrast between carbon and oxygen in this spectral range enabling material resolved bio imaging, distinguishing between functional components of a specimen. Before using the introduced XUV source with regard to lensless imaging, biological samples in form of HEK293 cells [73]¹, provided by Prof. Dr. Stefan Heinemann et al. (CMB Jena), were imaged. These cell line has artificially added cancerous characteristics and is widely used for vaccine research and

¹Human Embryonic Kidney cells, 293rd experiment

virology [74]. Adding iron-oxide spheres with diameters of 1 and 2.8 μm with a receptor coating leading to accumulation of these spheres at specific positions of the cell membrane [75]. Whereas the biological and medical significance should not be discussed in this work, prepared specimen like these are suitable objects for testing the capabilities of imaging systems. Due to the harsh environment and the rather high energy of the radiation, living cells cannot be imaged, apart from a few exceptions using specialized mounts [76]. Therefore the cells have to be fixated (plastination or freezing) to preserve their structure during the measurement. The HEK293 cells used in this experiment had been fixated after growing on 100 nm thin silicon membranes using para-formaldehyde. After fixation the samples were stored in a phosphate-buffered saline (PBS). Before applying the samples onto the mount, they had to rinse with ultra-pure water to avoid crystallization of PBS on and around the cells. PBS crystals are highly absorptive ($<0.5 \mu\text{m}$ absorption length²) for the used wavelength, therefore PBS contaminated cells would be hardly visible. To get the direct projected images in the detector plane, the zone-plate had to be mounted in $\sim 900 \mu\text{m}$ distance to the sample. The NA of the zone-plate (approx. 0.05) roughly matches the NA of the multilayer mirror enabling Köhler illumination.

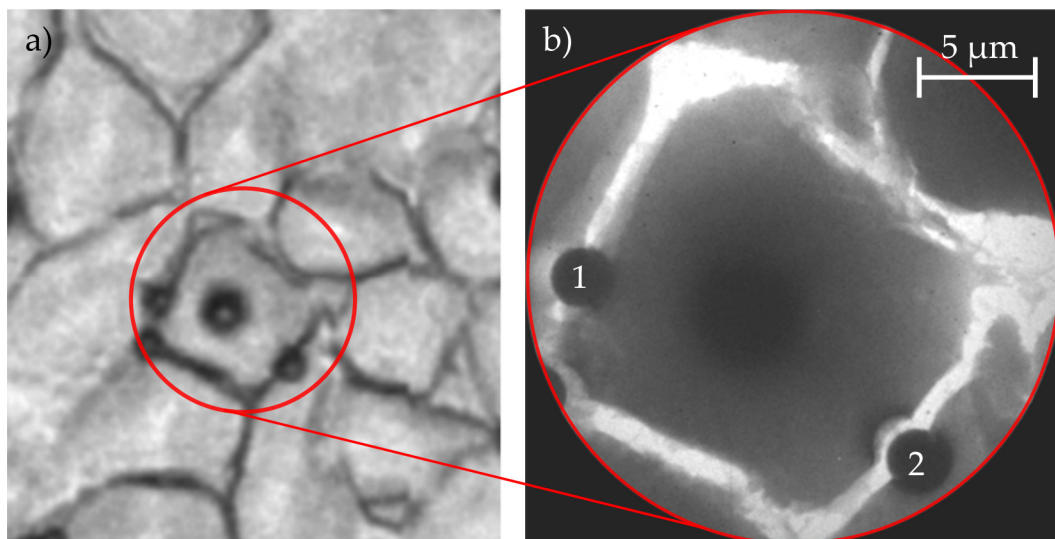


FIGURE 4.2: Image of a HEK293 cell with attached 2.8 μm Fe_3O_4 spheres. A microscopic image a) was captured with visible light and a magnification of 400 and shows a single cell with attached spheres. The XUV image b) reveals additional information about the sphere bonding. Whereas one sphere is attached to the cell (1), another seems repelled (2).

²CXRO X-ray database: absorption of NaCl (major component)

Fig. 4.2 shows a first picture of the labeled cells, taken with the water-window microscope with 60 s exposure time. The pixel resolution can be estimated with 16 nm. The real resolution will differ due to aberrations caused by the zone plate and slight misalignment. However, the higher resolution reveal the bounding behavior of the iron-oxide beads. The repulsion of some spheres become visible using the BliX setup in contrast to the image taken in the visible spectrum. The material contrast in Fig. 4.2 is quite low and only allows a determination of the cell boundaries. Cell structures remains hidden. A second cell, labeled with 1 μm spheres, was investigated to check the material contrast again.

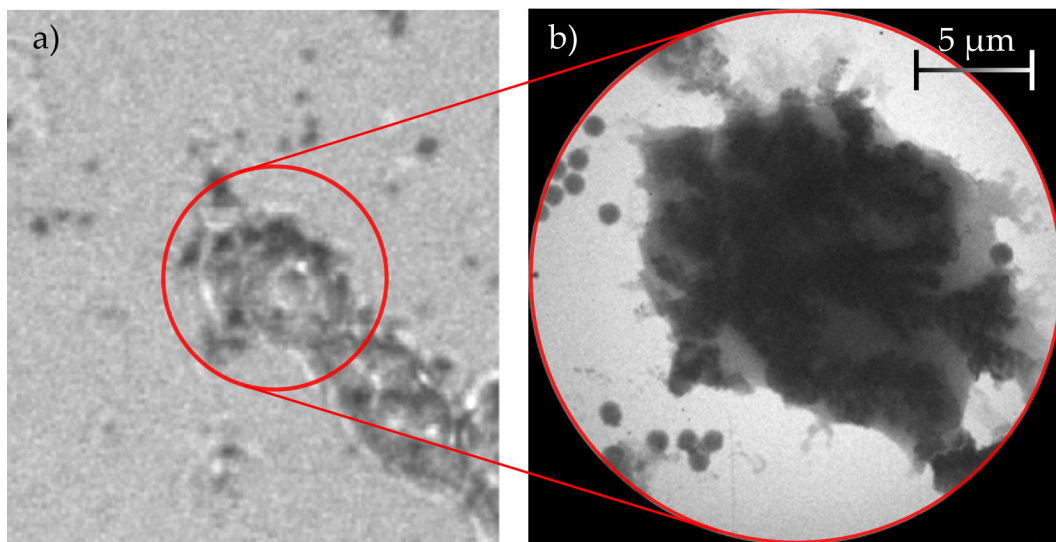


FIGURE 4.3: Image of a HEK293 cell with attached 1 μm Fe_3O_4 spheres. A microscopic image a) was captured with 400x magnification, like in Fig. 4.2, The XUV image b) show carbon rich inner cells structures invisible in a). The cell shape deviate from the one shown in Fig. 4.2.

The cell shown in Fig. 4.3 differs in shape and inner structure to the one shown in Fig. 4.2. The visible dark dendritically structures beside the spheres are likely to be carbon-dense vesicles [57], small intracellular parts of the cells, responsible for different task e.g. storage of proteins. However, carbon-dense vesicles, together with the frayed shape, are indicators for starving or damaged cells. Due to the rather high absorption of the specimen and the zone-plate, exposure times of 120 s were necessary to record moderate contrast images and sufficiently resolving the smaller spheres of 1 μm . Calculating the accumulated dose as the absorbed energy

per mass [77]

$$D = nE \frac{n\mu}{V\rho} \quad (4.1)$$

with nE as the number of photons carrying the energy E , V, ρ as the volume and density of the specimen and μ as the absorption coefficient, can give a hint to the origin of damage. With a total flux of $\sim 1.4 \times 10^{10} \text{ ph s}^{-1}$ (see next section), an approx. volume of HEK293 cells of $2000 \mu\text{m}^3$, a density of 1.35 g cm^{-3} and a linear absorption coefficient of an average protein of $1.25 \times 10^{-4} \text{ cm}^{-1}$ [78] leading to approx. $6.22 \times 10^6 \text{ Gy}$. Compared to previous measurements of radiation damages on biological samples [79, 80] it can be concluded, that the dose is sufficient low enough to results in a low carbon-bond break rate [79] and therefore low damage through radiation. Hence, the carbon accumulation seems to results from the time between growing and fixation. However, water window imaging enables resolving small features and defects, invisible using conventional microscopy. After testing the setup in this way, the zone-plate was removed and the biological tissue was replaced by a simple binary structure for direct source diagnostics shown in the following section.

4.3 Source characterization with a single diffraction pattern

The objective of the beamtime was a characterization of the source in terms of flux, stability and coherence to check its suitability for CDI and Ptychography. First tests with an improved SCIMITAR³ setup [81], to measure directly the spatial coherence, were not successful due to the high required distance between the hole pair and the detector. A technique combining sophisticated far field simulations with diffraction measurements was used instead to reveal the parameter of interest: A well defined sample⁴ was placed near the focus. The zone-plate and beamblock were removed to ensure highest intensities. Instead, a pinhole with $20 \mu\text{m}$ in diameter was placed directly in front of the sample to ensure a well defined spot. A long exposed diffraction pattern is then compared to simulated diffraction patterns with different combinations of possible parameters. First, the total flux was analyzed to ensure

³Scanning Interference Measurement for Integrated Transverse Analysis of Radiation

⁴Quantifoil™, Type R1/2

not generating mixed-state diffraction patterns. With removing the beamblock, also the He_α line can correspond to the diffraction pattern, which is unwanted and not included by the numerical model. Therefore the total flux of the Ly_α and He_α line had to be calculated.

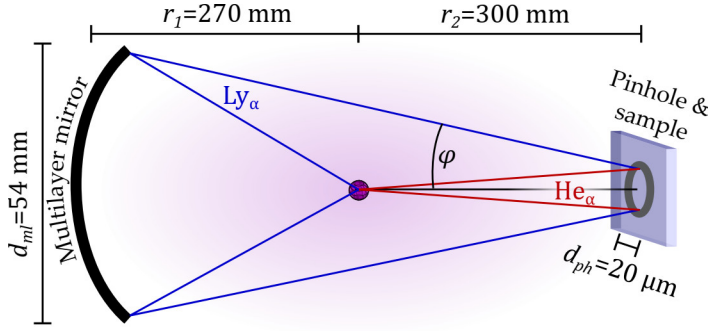


FIGURE 4.4: Scheme for total flux calculation. The multilayer mirror only reflects the Ly_α line, whereas He_α gets fully absorbed. The total flux reaching the pinhole can be calculated via illuminated areas.

Starting with the total emitted intensity of the plasma for Ly_α of $1.40 \times 10^{14} \text{ ph s}^{-1} \text{ sr}^{-1}$ and, with a spectral ratio $I_{\text{Ly}_\alpha}/I_{\text{He}_\alpha}$ of 0.8 [16], $1.12 \times 10^{14} \text{ ph s}^{-1} \text{ sr}^{-1}$ for He_α , one can derive the reflected intensity of Ly_α to

$$A_{r_1, sr} = r_1^2 = 7.29 \times 10^4 \text{ mm}^2 \quad (\text{Steradian area}) \quad (4.2)$$

$$A_{ml} = \pi(d_{ml}/2)^2 = 2.29 \times 10^3 \text{ mm}^2 \quad (\text{Mirror area}) \quad (4.3)$$

$$I_{ml, \text{Ly}_\alpha} = 0.004 \cdot I_{\text{Ly}_\alpha} \cdot \frac{A_{ml}}{A_{r_1, sr}} = 1.4 \times 10^{10} \text{ ph s}^{-1} \quad (4.4)$$

Where the direct radiation is negligible due to the small solid angle. The intensity of the direct radiation of the He_α line at the pinhole however calculates to:

$$A_{r_2, sr} = r_2^2 = 9 \times 10^4 \text{ mm}^2 \quad (\text{Steradian area}) \quad (4.5)$$

$$A_{ph} = \pi \cdot (d_{ph}/2)^2 = 3.14 \times 10^{-4} \text{ mm}^2 \quad (\text{Pinhole area}) \quad (4.6)$$

$$I_{ph, \text{He}_\alpha} = I_{\text{He}_\alpha} \cdot \frac{A_{ph}}{A_{r_2, sr}} = 2.7 \times 10^5 \text{ ph s}^{-1} \quad (4.7)$$

The 5 magnitudes lower Intensity of the He_α line at the position of the pinhole therefore should not influence the diffraction pattern, assuming the pinhole is closely attached to the sample and comparable quantum efficiencies of the detector⁵. Due to

⁵ 90 % quantum efficiency for both lines, Datasheet Andor Ikon L SO

the small wavelength of ~ 2 nm, the diffraction for rather large sample features (several μm) is weak, resulting in small scattering angles. Therefore the camera had to be placed 33 cm behind the sample to enable sufficient sampling resulting in a NA of 0.04. An exposure time of 1200 s was necessary to saturate the electron capacity wells of the pixels under restriction of the lowered dynamic due to the increased background.

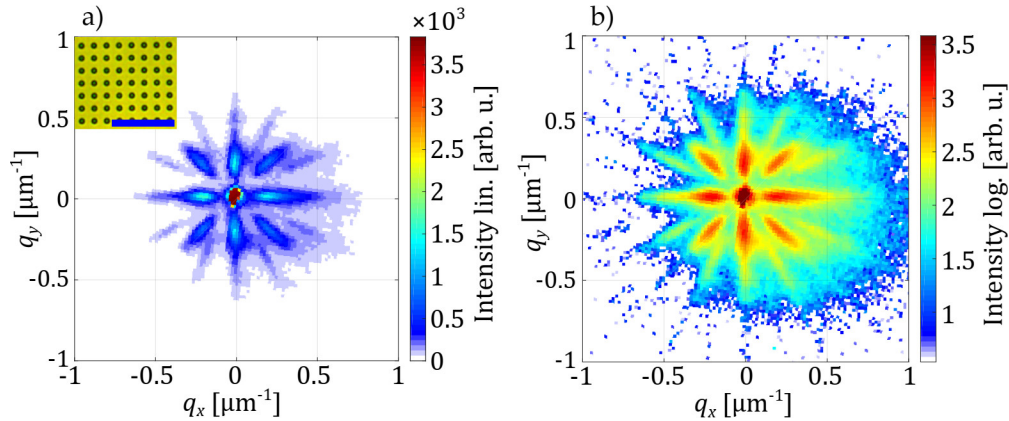


FIGURE 4.5: Long time exposure diffraction pattern using N_2 -plasma based soft X-ray source. The linear scale (a) show warping artifacts due to wavefront curvature changes during exposure. The \log_{10} scale (b) reveal a horizontally drifted diffraction signal and low-coherence-based blurring. The inset shows a microscopic image of the sample. The length of the blue bar represents $10 \mu\text{m}$

The pattern, shown in Fig. 4.5, reveals several artifacts caused by different effects: The sample consists of periodic holes, leading to a period dot pattern in k -space for stable, monochromatic illumination. The warping-like effects of the diffraction signal origins either from temporal incoherence or from fluctuating wavefront curvatures. The flux calculation above shows, that only the Ly_α line corresponds to the diffraction signal and the spectral width of Ly_α (1000) can be neglected. Hence, only wavefront curvature changes during the exposure can be responsible for the warping effect. Curvature changes can be attributed to an axial focal jitter and therefore an axial jitter of the plasma or size variations of the plasma itself. Due to the highly stable driving laser, the latter point seems unlikely. However, axial jitter can emerge from an unstable nitrogen jet, which was observed beforehand. Spatial incoherence lead to blurring of diffraction pattern's features and an increased background signal, which can be simulated and compared to the measurement. By comparing simulation and measurement, the mentioned hidden parameter can be revealed. The

following numerical framework is capable of computing spatial coherence and axial jitter. Astigmatism, pre-plasma or a radial shift of the source are currently not supported.

To simulate the observed effects in Fig. 4.5, variable partially spatial coherence with diameter ζ_t and axial jitter j have to be implemented numerically. Before propagating the illuminated object onto the detector plane, an illumination function including partially coherence and wavefront curvature has to be formed. First a Gaussian intensity profile with curved phases was created to mimic a perfect coherent phase front with a distance d to the source.

$$\hat{\Psi}_{\text{gauss}}(x, y) = E_0 \frac{w_0}{w_z} e^{\left(\frac{x^2 + y^2}{w_z^2} \right)} e^{\left(i \frac{2\pi}{\lambda} \left(\frac{x^2 + y^2}{2r_z} + z \right) - i \arctan \left(\frac{z}{z_r} \right) \right)} \quad (4.8)$$

with x, y as the grid coordinates, w_0 as the radius of the focal spot, w_z the beam waist in dependence of the propagation length z and r_z as the curvature of the wavefront:

$$w_z = w_0 \sqrt{1 + \left(\frac{z}{z_r} \right)^2} \quad (4.9)$$

$$r_z = z \left(1 + \left(\frac{z}{z_r} \right)^2 \right) \quad (4.10)$$

$$z_r = \sqrt{2} \frac{w_0}{\tan(\varphi)} \quad (4.11)$$

Here, z_r defines the Rayleigh length in dependence of the divergence angle φ . The spatial coherence was then applied via combining the curved illumination $\hat{\Psi}_{\text{gauss}}$ with random phases with decreasing variance to the center:

$$\hat{\Psi}_{\text{illu}}(x, y) = \hat{\Psi}_{\text{gauss}} e^{\left(i \left(1 - \left(\frac{\ln(2)(x^2 + y^2)}{c^2} \right) \right) \hat{\Xi}(x, y) \right)} \quad (4.12)$$

Where $\hat{\Xi}(x, y)$ is a random number generating function with values between 0 and 2π . Now, the Hadamard product of $\hat{\Psi}_{\text{illu}}$ and the object function $\hat{\Psi}_{\text{obj}}$ can be fourier-based propagated to the detector plane. Partially spatial coherence is then reached

by superposing several propagations using updated illumination functions with different random phases and unchanged remaining parameters:

$$\hat{\Psi}_{\text{det}} = \frac{1}{t} \sum_t |\mathfrak{F}(\hat{\Psi}_{\text{illu}} \odot \hat{\Psi}_{\text{obj}})|^2 \quad (4.13)$$

Where $\mathfrak{F}(\hat{\Psi})$ is a Fourier-based propagator for an arbitrary complex-valued field [82] and t is the number of pattern to average over. This procedure imitates the time averaging of a measurement using partially coherent light, blurring out diffraction features and leading to a Gaussian-like background [83]. Implementing the warping effect can now be achieved by averaging between diffraction patterns with different curvatures used in the illumination.

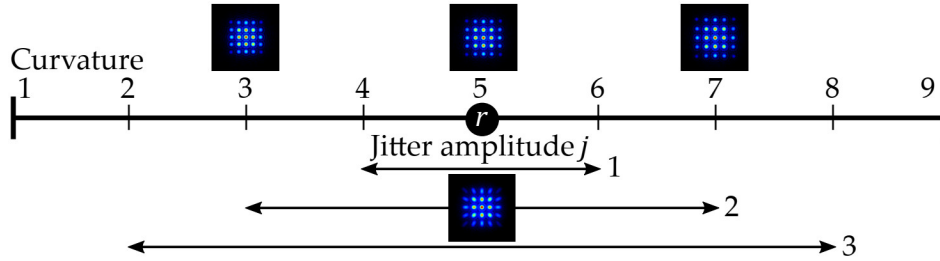


FIGURE 4.6: Principle of axial jitter decomposition. Starting from a rest position r , the jitter amplitude j can be decomposed into several overlaid curvatures, equally distributed around r . Combining diffraction patterns with different curvatures lead to warping effects. As an example, a jitter amplitude 2 (arb. u.) is decomposed to curvatures from 3 to 7 (arb. u.). Superposing the corresponding diffraction pattern results in a warped pattern.

Fig. 4.6 shows the principle of superposing different curvatures into a warped diffraction pattern with axial jitter based warping. Diffraction patterns were created for different curvatures. Around a defined rest position r , diffraction pattern were superposed to a warped pattern with respect to the jitter amplitude. This procedure can be done for every coherent diameter, creating the diffraction matrix $\hat{\mathbf{D}}(\zeta_t, j, r, q_x, q_y)$ shown in figure 4.7.

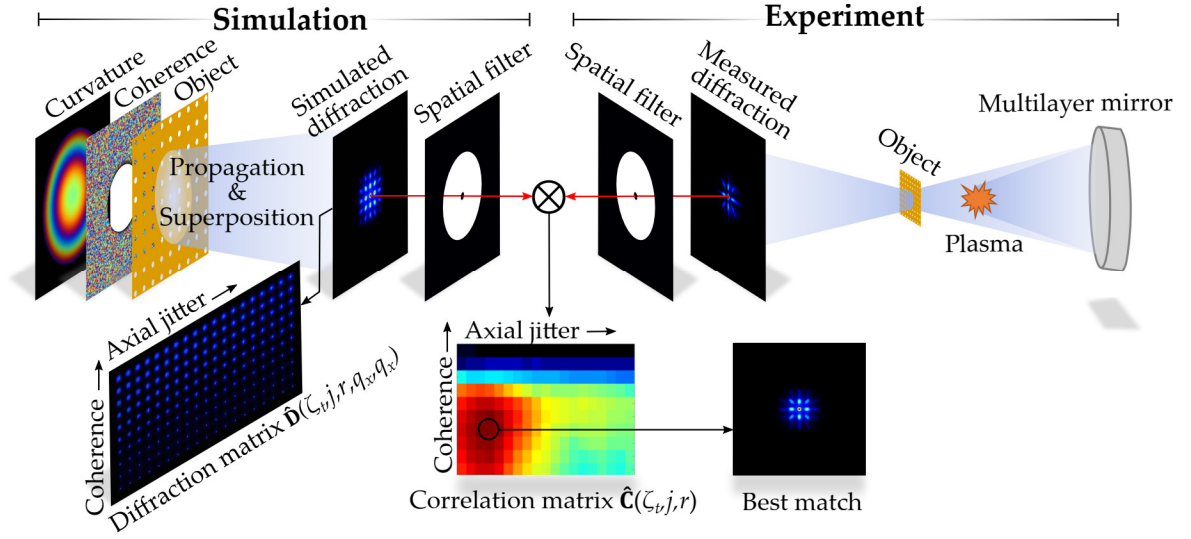


FIGURE 4.7: Schematic of the single-shot beam analyzing algorithm. A complex-valued illumination function is formed by overlaying a curved wavefront with a ring of random phases to simulate a partially coherent source with axial jitter. The far-field diffraction pattern of the illuminated object for a fixed curvature and coherence is first buffered in a 4D matrix (not shown here). By superposing diffraction patterns for a fixed coherence diameter ζ_t , fixed rest positions r and with different axial jitter amplitudes j , the diffraction matrix $\hat{\mathbf{D}}(\zeta_t, j, r, q_x, q_y)$ is formed. Every element (ζ_t, j, r) of $\hat{\mathbf{D}}$ is then filtered by a ring-filter to neglect unwanted signal. Correlating the filtered simulated pattern with the filtered measurement generates the correlation matrix $\hat{\mathbf{C}}(\zeta_t, j, r)$. The maximum of $\hat{\mathbf{C}}(\zeta_t, j, r)$ reveals the parameter with the highest probability to be accountable for the measured diffraction pattern. Time averaging for gaining partial incoherence, superposing of the simulated pattern and disassembling of the jitter is not shown for the sake of clarity.

Finally the calculated warped diffraction pattern can be compared to the measurement using a 2D correlation after filtering the measurement and simulation results with a ring filter. The filter prevents disturbance due to noise at high momentum $q_{x,y}$ and the slightly overexposed central region at zero momentum of the measurement. The algorithmic procedure can be summarized as follows:

- 1) Define axial jitter amplitude j and coherence diameter ζ_t limits and assume a starting rest position r .
- 2) Decompose a jitter amplitude j into several equally distanced wavefront curvatures around r (Fig. 4.6).
- 3) For every curvature, simulate several patterns with different random phases with coherence diameter ζ_t (Eq. 4.12) and sum up over the complex-valued diffraction pattern (Eq. 4.13).

- 4) Sum up over diffraction patterns of every curvature for fixed coherence, retrieved in step 3, to obtain the diffraction pattern for the axial jitter j and coherence diameter ζ_t .
- 5) Filter the measured and simulated pattern with a ring filter to neglect high- q signal such as noise and the overexposed center.
- 6) 2D correlate the simulated pattern with the measured one for generating the correlation matrix $\hat{C}(\zeta_t, j, r)$.
- 7) Find maximum of $\hat{C}(\zeta_t, j, r)$ to get parameter ζ_t, j, r obtained during the experiment.

The boundaries of jitter and coherence can be obtained by simple forward testing simulations and comparing them to the measurement by eye. The curvature limits can be estimated via simulating two patterns, matching the inner and outer points (minimal / maximal q) of a warped feature of the measurement. The coherent diameter limits can be evaluated by comparing the highest visible transferred momenta. The axial jitter amplitude can be seen as a deflection from the rest position of the focal spot and therefore of the plasma. Hence, a center curvature can be geometrically calculated and the deflection can be expressed as a shift of wavefront curvature around the rest position, which is assumed to be in the center of curvature limits. Due to the small Rayleigh length of $\sim 600 \mu\text{m}$, the relation between curvature and focal distance becomes linear and the focus center curvature is equal to the distance focus-sample. For a better estimation of the real rest position, the merging of the simulated diffraction patterns start at different positions (rest position) around the assumed one. Every correlation matrix $\hat{C}(\zeta_t, j)$, in dependence of the rest position, shows its own global maximum (see Fig. 4.8). With evaluating the highest maximum of every correlation matrix, the most likely rest position can be found. The following results were taken with the jitter amplitude limits $j_{\min} = 0 \mu\text{m}$ to $j_{\max} = 1500 \mu\text{m}$ in 20 equally spaced steps. The coherence diameter limits were chosen to be $c_{\min} = 1 \mu\text{m}$ to $j_{\max} = 20 \mu\text{m}$ in 20 equally distance steps. The rest position was varied from 2.3 to 2.7 mm distance between focus and sample in 20 steps. The measurement was oversampled by a factor of 4 to enhance the correlation quality.

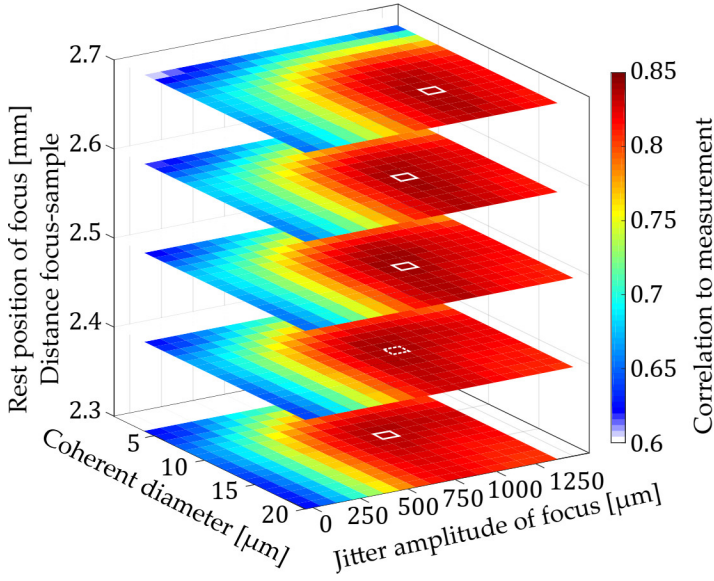


FIGURE 4.8: Stack of correlation matrices. With different rest positions of the focus, the maxima (white solid squares) of the corresponding correlation matrices $\hat{C}(\zeta_t, j, r)$ shift. Finding the global maximum (white dashed square) reveals the experimental parameter. For the sake of clarity, only five rest positions are shown.

Evaluating the correlation matrix stack, seen in Fig. 4.8, enables the determination of the experimental parameter. The correlation matrix calculated at 2.4 mm rest position shows a maximum at 11 mm coherent diameter and 820 μm jitter amplitude. Due to the similarity of adjacent pixel, a jitter error of $\pm 60 \mu\text{m}$ and an error of the coherence diameter of $\pm 1 \mu\text{m}$ can be estimated. The jitter of the focus must now be converted to the plasma's jitter j_p via the lens equation:

$$j_p = \frac{d_i f_{\text{ml}}}{d_i - f_{\text{ml}}} - \frac{(d_i - j) f_{\text{ml}}}{(d_i - j) - f_{\text{ml}}} \quad (4.14)$$

With the focal length of the multilayer mirror $f_{\text{ml}} = 175 \text{ mm}$ and the image distance $d_i = r_1 + r_2 = 0.57 \text{ m}$. Due to the small jitter in comparison to the rather large image distance, the dependence between them can be assumed to be linear. Fig. 4.9 shows the correlation matrix of the best matching rest position with overlaid simulated diffraction pattern. The best matching simulated pattern is compared to the measurement and is generated with $(11 \pm 1) \mu\text{m}$ coherent diameter and a focus jitter of $(820 \pm 60) \mu\text{m}$, which correspond to $\sim (160 \pm 10) \mu\text{m}$ axial jitter of the plasma. Fig. 4.9 shows the best matching pattern to the simulation. Whereas most of the diffraction features are well reconstructed, the shifted background is still under investigation and might allow inferences to the plasma's shape or the mirrors alignment. Here, the shape of illumination was declared to be symmetrically. Previous simulations with asymmetrical illuminations showed deviating diffraction pattern

due to the transfer of asymmetry during the propagation.

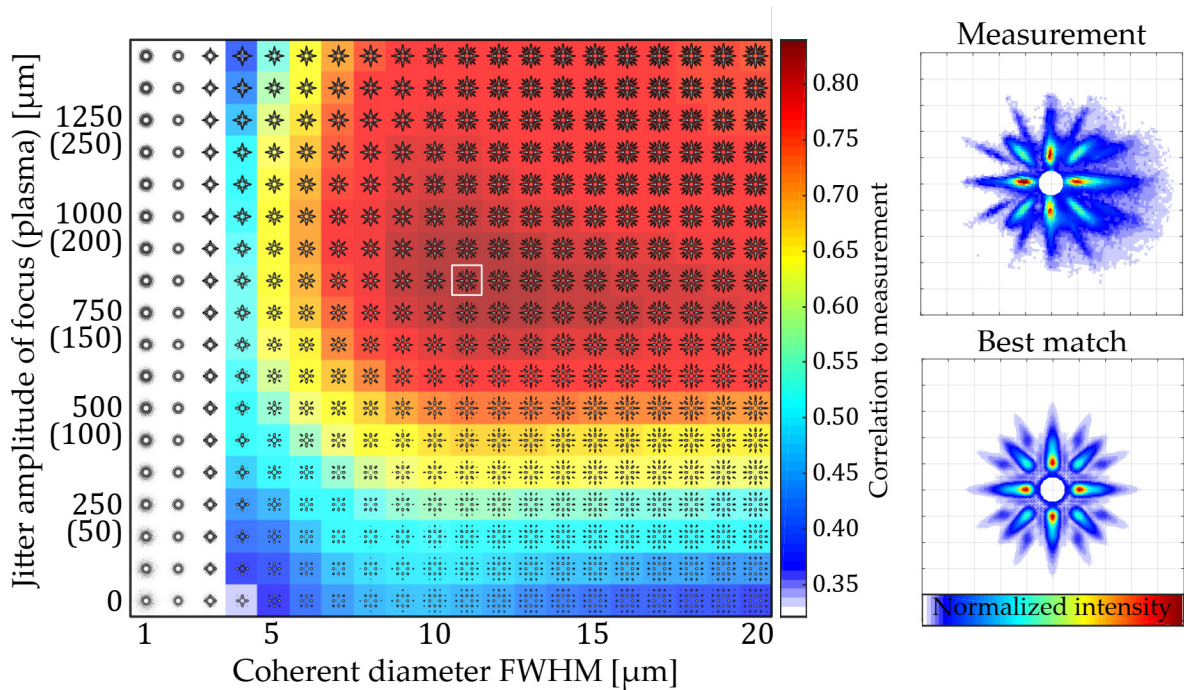


FIGURE 4.9: Correlation matrix of the best matching rest position. The correlation values are overlaid with the corresponding simulated diffraction pattern. The maximum (white square) of 84 % correlation reveals a parameter set of 820 μm jitter and 11 μm coherent diameter for 2.4 mm average distance between focus and object. The best matching pattern reveals similar diffraction features in comparison to the measurement except the shifted background.

The relatively low coherence of the source of 7.5 % (coherent area) in comparison to the LOA-SXRL (32 % coherent area) (see chapter 5) or *PETRAIII* (35 % coherent area) (see chapter 3) requires beam-shaping apertures to enable diffraction imaging to suppress an incoherent background. Cutting the beam to increase the spatial coherence to an HHG-SXRL-like niveau (30 %) would decrease the intensity on the sample by approx. 2 magnitudes, resulting in higher exposure times. The axial jitter would then lead to the warped pattern, which must be numerically compensated afterwards. However, the axial jitter becomes neglectable when using a zone-plate for direct imaging as shown in the previous section with directly recorded images under equal conditions of the source.

4.4 Summary

Compact laser-driven plasma sources emitting in the water window are capable of delivering high flux and energies distributed in a rather large solid angle. The large plasma source of several 10 μm and the incoherent emission scheme however restrict the efficiency for diffraction-based imaging methods. Whereas zone-plate based imaging is not affected by incoherence and is more insensitive to jitter, lensless imaging becomes inapplicable. Different techniques are suitable for characterizing XUV sources but have to be adapted to e.g. the flux or coherence. For example, Hartman-Shack wavefront sensors [84] can be used for determining the phase profile, but require a rather high spatial coherence, as they work with diffraction. The SCIMITAR method [81] becomes non applicable at high energies due to the low diffraction angle. Increasing the angle via closing the apertures would decrease the flux and, therefore, increase the exposure time to an impractical amount. The method developed in this work shows the benefit that it only requires a focusing system. A well-known sample is illuminated via a multilayer mirror with an image of the source. The resulting diffraction, as weak as it can go, is captured by a CCD. Long exposure images incorporate the source's jitter as warping like effect, monochromatic light assumed. Comparisons with sophisticated simulations, including manifold beam parameters, reveal the source's parameter during the exposure. The so determined lateral coherence diameter and jitter behavior of the source can be used for evaluating different imaging techniques in terms of their suitability. Furthermore, the jitter of the source can be further reduced by closed-loop measurements to enhance the image quality of the conventional zone-plate setup.

Chapter 5

Beam diagnostics of a seeded SXRL for ultrafast XUV imaging

As mentioned in the previous chapters, successful reconstructions are mainly based on the quality of the recorded diffraction patterns. Proper pre-processing is necessary and enables the reconstruction algorithm to converge in the first place (see appendix A). Nevertheless the best prerequisite regarding high quality diffraction images is a light source with excellent coherent conditions. Pure HHG-based light sources maintain a sufficient high spatial coherent area of roughly 60% but only a flux of $\sim 10^5$ ph s⁻¹ for orders near the cut-off frequency due to the low conversion efficiency and the discrete spread spectrum. As a result, they are well suited for generating high contrast diffraction patterns under the constraint of long exposure times. This in turn calls out for a high stable source regarding pointing, beam profile and wavefront aberrations.

Plasma based XUV sources relying on the scheme of ASE however working under the principle of recombination of discrete atomic transitions in a plasma. In the pumped optical gain medium with population inversion, spontaneous emission occurs randomly. Photons directed along the optical axis can induce stimulated emission. ASE occurs in every gain medium and is the starting condition for lasing processes, if the medium is enclosed by a cavity and the lasing threshold is reached. For non-cavity solid state amplifiers, the spectrum is broadened due to the missing cavity feedback and the fluorescence characteristics of the medium. Deexcitation of discrete atomic states in a plasma however lead to a discrete spectrum with narrow

bandwidth and therefore to high temporal coherence of the emitted radiation. Theoretically, the flux of such a super-luminous light source is limited by the amount of excited states during the process of deexcitation. In conclusion ASE based plasma sources are capable of emitting high brilliant radiation. However, due to the intrinsic randomized generation of photons in the first place, the wavefront fluctuates, resulting in high divergence, low transversal coherence and strong pointing [52], which does not suit the requirements of high contrast diffraction imaging.

To combine the benefits of these two worlds, HHG and ASE, the HHG-seeded SXRL at the Laboratoire d'optique appliquée (LOA, Palaiseau, France) was developed: A laser-driven plasma amplifier relying on the ASE scheme gets seeded by a high optical quality HHG beam [85]. This unique combination allows a high stable, high energy output at 32.8 nm wavelength with 60% coherent area and a flux up to 3×10^{11} ph s⁻¹. In the following sections, the setup of the SXRL and the surrounding experiment will be explained first. Afterwards, single shot diffraction experiments will show its capabilities of ultrafast complex-valued imaging with high resolution. Ptychography, used to retrieve the illumination function, will give access to the ionizations dynamics of the plasma amplifier via complex-valued backpropagation to the source and comparison to Maxwell-Bloch-simulations.

5.1 Experimental setup

All experiments in this chapter were performed at LOA using the 2J “Salle jaune” Ti:Sapphire laser operating at 813 nm central wavelength and 30 fs pulse duration. To create a waveguide and pumping the plasma amplifier, the main pulse is split into several sub-pulses: First a Krypton plasma channel, which acts as a waveguide and the gain medium is created by a pulse train consisting of a ignition pulse (130 mJ, 30 fs) followed by a heater pulse (690 mJ, 600 ps) via optical field ionization (OFI). Due to the limited propagation of the IR pump-pulse in a near-critical density plasma, the waveguide is one of the most crucial parts. Refraction, diffraction and self-focusing would otherwise limit the amplifying length to a few hundred micrometers [85]. As a lasing transition, the $3d^94d_{(J=0)} \rightarrow 3d^94p_{(J=1)}$ (total momentum

J) transition of Nickel-like Krypton (Kr^{8+}) at 32.8 nm is chosen (Fig. 5.1). To obtain population inversion of the $3d^9 4d$ state via collisional pumping directly or by relaxation of the $3d^9 4f$ state, a pump pulse (1.36 J, 30 fs) is focused in the plasma channel using an Axicon. The excited $3d^9 4d_{(j=0)}$ state depletes with a lifetime of ~ 20 ps [84] and corresponds to the narrow bandwidth of the SXRL. The natural lifetime of the lasing transition would limit the shortest pulse length of the XUV output in the ASE scheme. Here, a third IR pulse (20 mJ, 30 fs) is focused into a Argon gas cell to obtain a high quality HHG pulse. Instead of letting the plasma freely radiate through spontaneous emission, the 25th harmonic of the driving laser is used for amplification as it matches the lasing transition of Kr^{8+} at 32.8 nm. The injection time has to be synchronized to the gain periode of the lasing ion to force depletion to the ground state via stimulated emission. Due to the sudden depletion of the excited atomic level below the fluorescence timescale and the corresponding ionization gating, the duration of the XUV pulse could be shrunk to ~ 450 fs (FWHM) [86], which paves the way for ultrafast high resolution dynamic imaging.

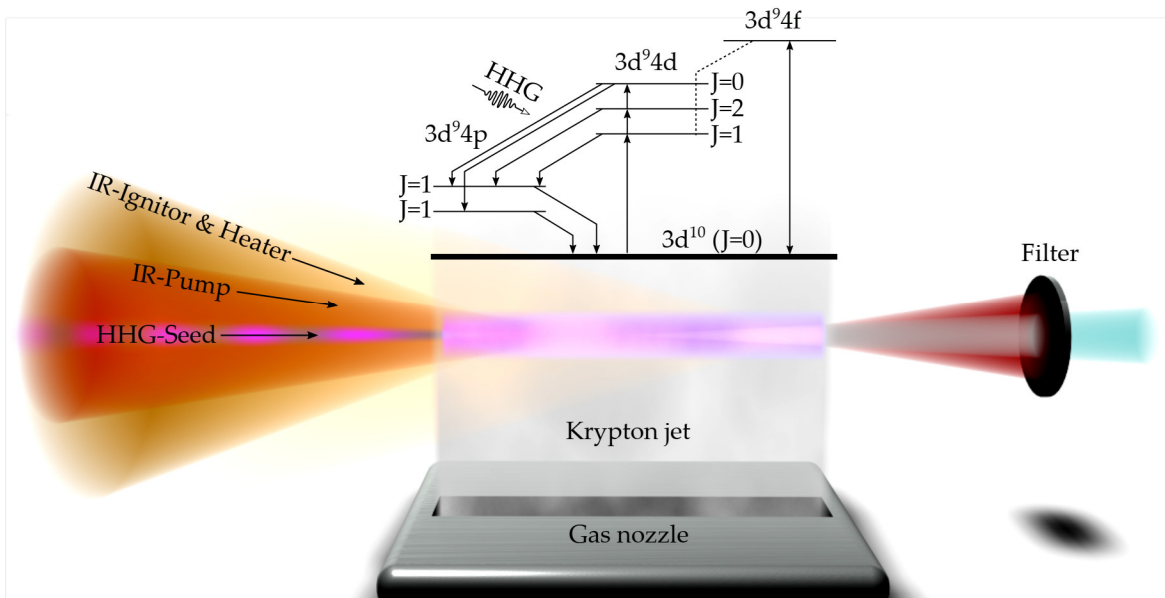


FIGURE 5.1: Exciting of the laser plasma amplifier and lasing scheme. An IR ignitor- and heater-pulse creates the plasma channel via OFI. The Kr^{8+} lasing ion reaches population inversion via collisional pumping by a second IR pulse. Either the $3d^9 4d$ state is directly pumped or reached via relaxation of the $3d^9 4f$ state [84]. The now excited $3d^9 4d_{J=0}$ states getting depleted by a HHG seed of 32.8 nm, matching the transition energy.

The XUV pulse has to be separated from the IR residuals by using aluminum filters of 500 nm thickness before it passes several switchable analysis tools for beam pointing and profiling. The chamber itself is shown in Fig. 5.2 and is mounted in a distance of roughly 4.5 m from the plasma channel to the entrance flange. The chamber consists of a stainless steel frame with interchangeable aluminum walls to ensure maximum flexibility during the experiment and is leakage proofed down to 5×10^{-7} mbar.

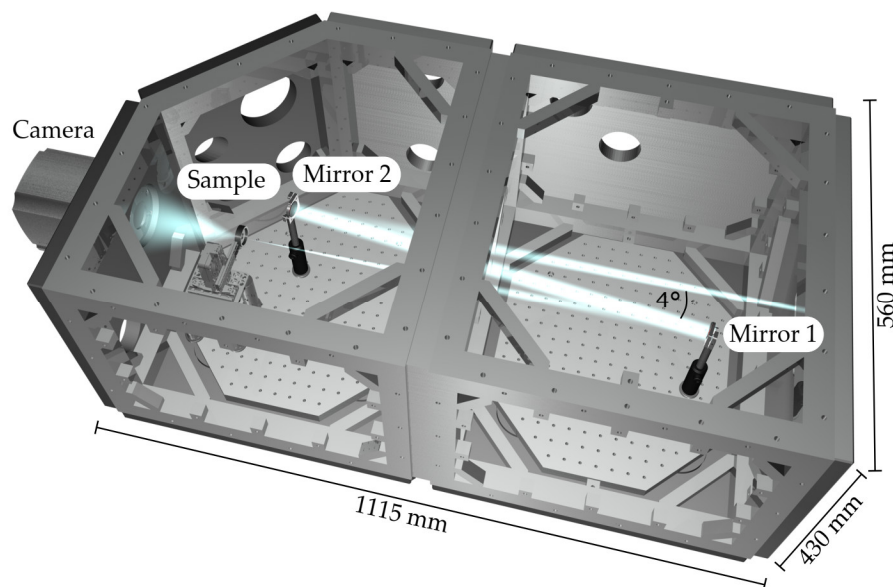


FIGURE 5.2: Imaging chamber used for diffraction experiments with indicated beam path. The beam enters from right, hitting mirror 2 and mirror 1 under an AOI 4° , before it is focused onto the sample. The small AOI (4°) of the mirrors require a long optical path and corresponding large vacuum chamber to avoid clipping and aberrations.

The XUV beam is imaged onto the sample by a system of two spherical multilayer mirrors designed for 32.8 nm with 1.2 nm bandwidth under 4° AOI. The beam gets collimated by mirror 2¹ ($f = 5$ m) and is then focused onto the sample by mirror 1 ($f = 0.5$ m) resulting in a demagnification of 10. The sample is mounted on a high precision 3D Slip-Stick positioning system with sub nanometer resolution and 10 nm repeatability. The positioner was mounted as close as possible to the CCD of the camera (Andor iKon L 4k). Due to the depth of the connector, a minimum distance of 55 mm could be realized. Thus, resulting in a NA of 0.24, allows a theoretical resolution of 70 nm.

¹The labeling was chosen because of the backpropagation procedure and is therefore numbered against the beam direction

5.2 Single-shot ultrafast lensless diffraction imaging with binary samples

Due to the ionization and seeding processes in the plasma waveguide, the pulse duration of the emitted XUV radiation can be as short as 450 fs. In this range, high speed dynamics such as electron-phonon scattering [87] or chemical reactions [88] occur. This processes not only happen on a short time scale, but also on a small volume, requiring high spatial resolution imaging. A tabletop ultrafast XUV source seems to be a convenient tool if combined with a matching imaging system. To test the coherence properties, binary samples were used to neglect phase shifting effects, which would complicate the reconstruction. The samples, shown in Fig. 5.3, consists of a 3 mm in diameter, 200 μm thick silicon wafer with etched 200 nm thin Si_3N_4 membranes and plated with 200 nm gold, structured with a focussed ion beam (FIB). The transmission of 200 nm Si_3N_4 at 32.8 nm wavelength can be assumed to $T = 2\%^2$. The gold plating therefore enhances the edge contrast and lead to nearly perfect binary sample. Due to the anisotropic etching mechanism in mono-crystalline silicon, the characteristic frustum under 54.7° is formed.

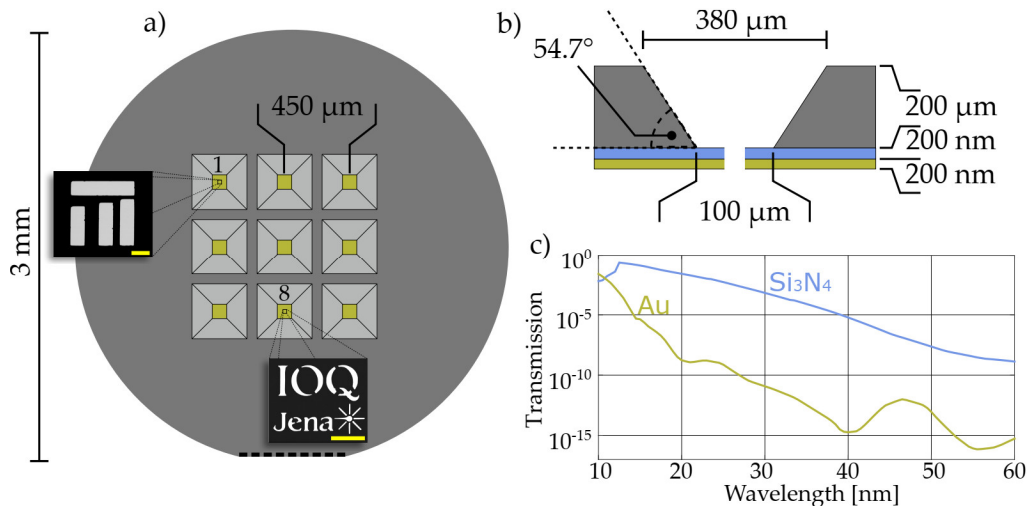


FIGURE 5.3: Structure and dimensions of the sample. Nine windows are etched in a 3 mm SI100 silicon wafer (a). The flat is marked with a dashed line. The membranes containing the binary structure consist of 200 nm Si_3N_4 coated with 200 nm gold (b). Due to the high absorption of the material combination in the XUV (c), the object can be considered as binary. The used samples in this chapter are window 1 and 8. The yellow bar corresponds to 1 μm .

²Source: Center for X-ray Optics (CXRO), Database for solid transmissions

To ensure a sufficient sampling of the object, the coherent spot size has to be well known. Also for the following section, the spot diameter will play an important role for determining the ptychographic scanning map. A good approximation for the total spot size can be derived using the emitting source diameter of 80 to 100 μm FWHM [86] and a demagnification factor of 10 to approx. 10 μm . The coherent part of the beam, however, is lower. An object with several windows containing a regular hole structure in 50 nm copper plated carbon (1 μm hole diameter, 2 μm pitch)³, normally used as transmission electron microscope (TEM) sample carriers, was used for first CDI imaging experiments to get an estimate of the coherent diameter by analyzing the reconstructed holes. The holes itself act as isolated objects smaller than half the spot size and therefore fulfill the Nyquist constraint. As the results of CDI reconstructions are Hadamard products of the illumination function with the object, using a binary object therefore simplifies estimations about the illumination itself. As opposed to the following experiments, this diffraction pattern was recorded with several shots and stitched together to increase the signal. Counting holes is indeed the most simple procedure but also the most imprecise one. Better results are achievable by fitting a 2D Gaussian function as an envelope to the reconstructed hole pattern and derive the FWHM. Fig. 5.4 shows the diffraction pattern with the corresponding reconstruction after 1000 iterations using error reduction (ER) and RAAR. The fitted gaussian envelope delivers a FWHM of 5.6 μm assuming a symmetrical beam profile. Presuming the worst case of a total illumination diameter of 10 μm FWHM, approx. 32 % of the illuminated area can be considered to be coherent. An unseeded SXRL like the Molybdenum based SXRL of the Max-Born-Institute Berlin [52] reaches comparable parameters regarding flux, wavelength and temporal coherence, but offers only 4 % (FWHM) of the illuminated area as coherent.

The following experiments were done in single shot mode with approx. 450 fs pulse duration realized at 1.2 ps delay between pump- and seed pulse. The samples correspond to the composition seen in Fig. 5.3. The chosen binary sample structures match the coherent spot size regarding the Nyquist theorem and the isolation constraint. Before any reconstruction taking place, the transversal beam jitter in phase

³Quantifoil™, Type R1/2

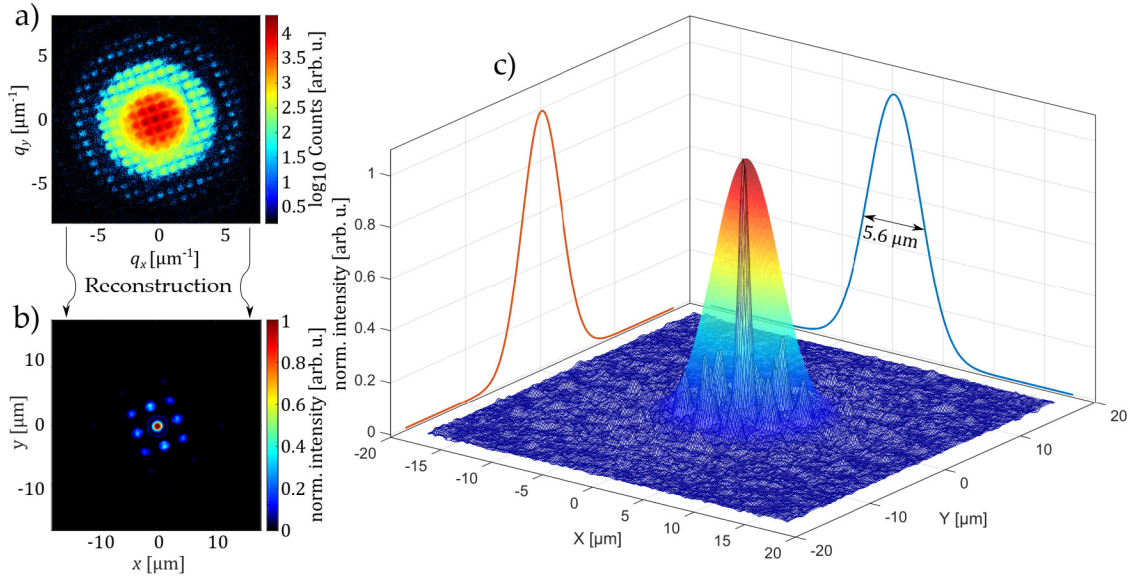


FIGURE 5.4: Reconstruction of regular hole pattern for determination of the transversal coherence. The preprocessed diffraction data in a) was reconstructed using the ER and RAAR algorithm (b). The reconstruction shows the Hadamard product between the binary structure and the coherent part of the illumination function. By fitting a Gaussian envelope (c) to the reconstructed object, the coherent diameter can be read out.

Reconstruction parameter			
Update function:	ER + RAAR, $\beta = 0.9$	Support:	Static, disc, $10 \mu\text{m}$
Iterations:	1000	Constraints:	Positivity

and intensity had to be analyzed. The sample “IOQ logo” (Fig. 5.3, window 8) with an overall size of $\sim 3 \mu\text{m}$ and features down to 100 nm should serve for jitter diagnosis. Therefore a series of 100 consecutive single shots were taken to observe potential beam distortions. If the illumination jitters in phase and amplitude, the diffraction patterns changes as a response. Sufficient small shot-to-shot variations still enabling coherent merging of the single diffraction pattern and allowing a reconstruction of the stack.

A simulation of the expected diffraction pattern was generated with the “k_mask” code (see appendix B) and compared to the measured diffraction pattern of the shot series. Fig. 5.5a show the shot series pictured as 2D array of stitched patterns and how it get compared to the simulation in b). The comparison process itself is done via an image correlation coefficient I_{CC} :

$$I_{CC} = \frac{2(\max(R_{A,B}) - \overline{R_{A,B}})}{\max(R_{A,A}) - \overline{R_{A,A}} + \max(R_{B,B}) - \overline{R_{B,B}}}, I_{CC} \in [0, 1] \quad (5.1)$$

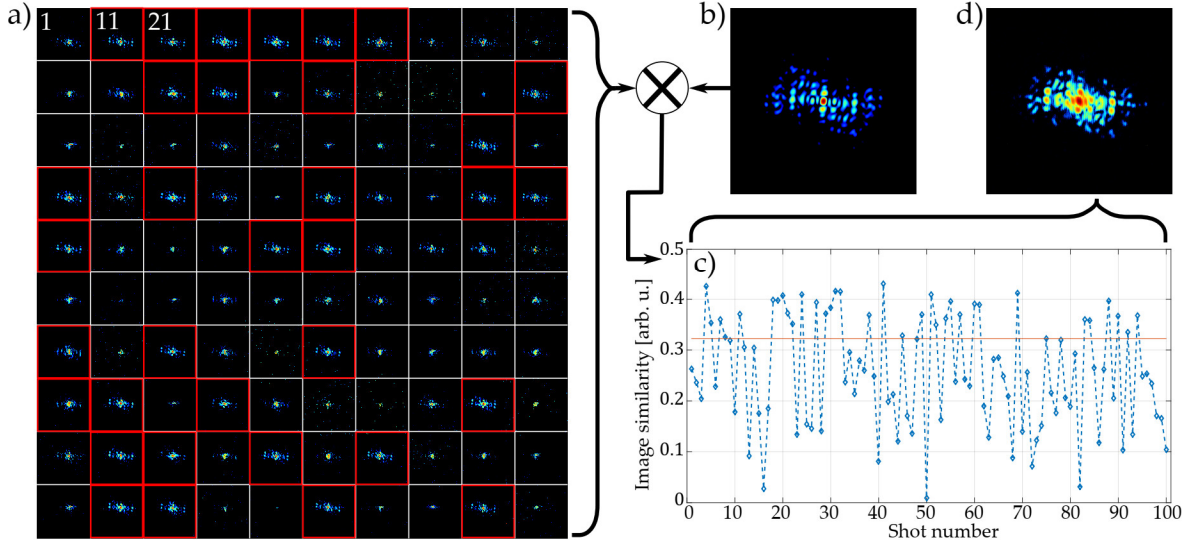


FIGURE 5.5: Analysis of pattern integrity for coherent merging. The single-shot diffraction pattern of the shot series (a) are compared to the simulated pattern (b) and results in corresponding correlation coefficients (c). Patterns with more than 75% accordance to the best matching pattern (Nr. 41) can be merged to a superimposed diffraction pattern (d). Matching patterns are marked with a red square in a). The dashed line should serve as a guide for the eye and does not indicate a physical connection.

Where R is the 2D real cross correlation

$$R_{A,B}(m,n) = \sum_x^{X-1} \sum_y^{Y-1} A(x,y)B(x-m,y-n) \quad (5.2)$$

with $m \in [-X + 1, X - 1]$, $n \in [-Y + 1, Y - 1]$, between the input images A and B . This metric allows the comparison between two images independent of lateral shifts. The results are depicted in Fig. 5.5c: 35 images (red squares in Fig. 5.5a) show a higher or equal I_{CC} than 75% of the best match (pattern #41), which was set as the criterion for a sufficient integrity enabling coherent merging of the diffraction pattern (Fig. 5.5d). Due to the natural differences between a simulation and experimental data, the image correlation coefficient cannot reach 1, therefore the data has to be normalized to the best match. The best and the merged stack of diffraction pattern were reconstructed to observe potential image degradation or enhancements. Additionally the PRTF gives information about the phase jitter. Small variations in the pattern due to incoherent merging lead to distortions in the stack causes nonphysical solutions. A perfect stable beam should not degrade the PRTF as the diffraction pattern not changes and increase the dynamic. Hence, the maximum useful momentum transfer decreases (see appendix A).

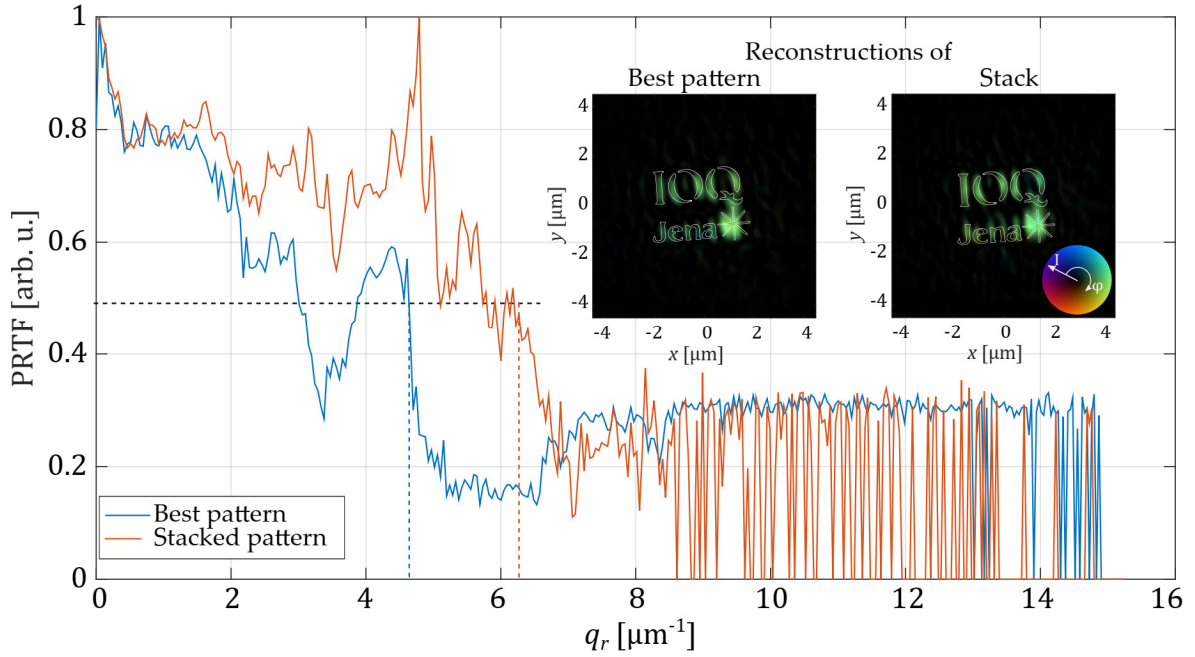


FIGURE 5.6: PRTF of a single diffraction pattern and the merged stack. The most similar diffraction pattern (Nr. 41) to the simulation was chosen for reconstruction shown in the inset. After the reconstruction of the stack, the PRTF of both were compared. Due to the coherent stacking of similar diffraction pattern, the maximum momentum q_{max} could be increased from 4.8 to $6.3 \mu\text{m}^{-1}$. As q_r rises above $8 \mu\text{m}^{-1}$, the PRTF begin to jitter due to low signal strength. As a guide for the eye, the contour of the object is marked in white.

Reconstruction parameter			
Update function:	ER + OSS, $\beta = 0.9$	Support:	Dynamic, autocorrelation
Iterations:	1000	Constraints:	Positivity

The merging of slightly different diffraction pattern lead to unpreventable smoothing of fine features. This is represented by a smoothed PRTF in Fig. 5.6. Due to the coherent stacking of the diffraction pattern above 75 % similarity to the best pattern, the 50 % PRTF limit yield in approx. $4.8 \mu\text{m}^{-1}$ (best diffraction pattern) respectively $6.3 \mu\text{m}^{-1}$ transferred momentum which corresponds to a resolution of 200 to 160 nm. This rather low resolution, compared to the Abbe-limit, explains the artifacts in the reconstruction of Fig. 5.6. The small features such as the star shape or small letters are not resolvable. Here the resolution can be increased by performing high dynamic range (HDR) capturing of diffraction patterns. This again calls out for consecutive taken shots, which increases the risk of merging wavefront distortions regarding Fig. 5.6. HDR-CDI is therefore only an option, if the images are merged after sorting out degraded diffraction pattern. This keeping in mind, a different object was used to capture single shot diffraction images. An irregular bar-like structure was used with an overall size of approx. $3.5 \mu\text{m}$ as seen in Fig. 5.3,

window 1. It has the same layer structure than the previous samples and was also FIB-written. To ensure the highest possible quality of the diffraction pattern, a shot series of 100 subsequently taken single shot diffraction pattern was recorded as seen above. This time, the best diffraction pattern was not chosen via image correlation, because the sample should be considered as unknown. The image comparison procedure request knowledge about the sample to simulate the diffraction pattern. The best diffraction pattern was chosen as the one with highest overall signal and visual integrity. As seen in Fig. 5.7a, after preprocessing, the highest momentum signal visible reaches nearly the edges of the detector, promising high resolution.

The highest counts are measured in the center with 60000 and nearly saturate the CCD. Nevertheless, analyzing the PRTF (Fig. 5.7d) reveals a half-maximum momentum of $\sim 5 \mu\text{m}^{-1}$, which corresponds to a resolution of 200 nm. Here, one must take into account, that the residual signal is still high and using a different criterion (e.g. 1/e) would results in a higher resolution. Therefore, an analysis of an edge was performed (Fig. 5.7b,e). A lineout profile was taken and fitted by an error-function. Using the 10/90 criterion results in 194 nm resolution. Note, that the shrink wrap support was relaxed during the reconstruction, meaning that the measured edge was not influenced by the support sharp cut. The complex presentation of the object in Fig. 5.7c has a non-zero area around the object, showing the loosened support. A closer look to the complex-valued object reveals interference-like fringes. Due to the high aspect ratio of the sample, accuring of waveguiding effect are likely [89]. Different approaches of reconstructions (different starting conditions) lead to similar results. Thus, the reconstructions can be seen as stable and reproducible.

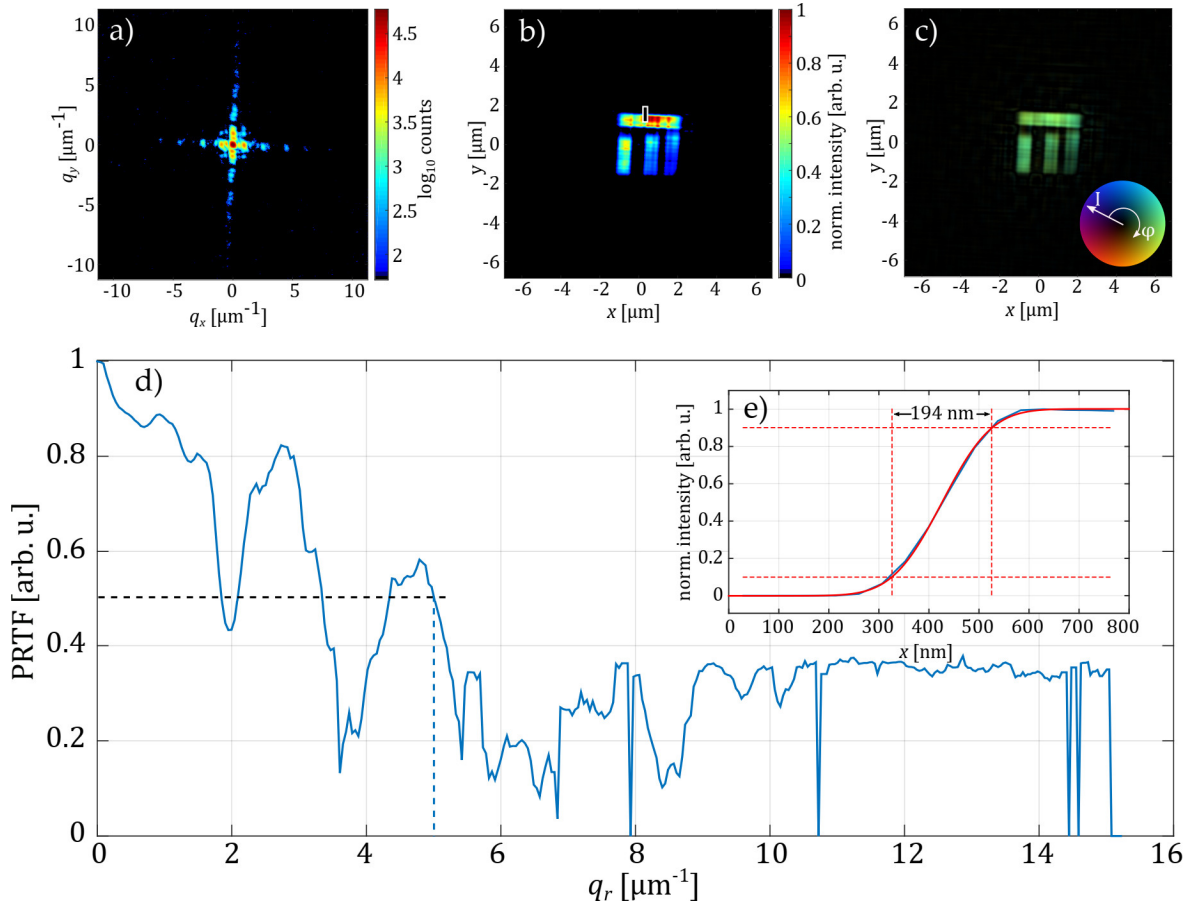


FIGURE 5.7: Analysis of the single-shot bar structure. The preprocessed diffraction pattern shows visible signal until the edges of the detector and highest counts up to 60000 counts per shot for the DC part. The reconstruction reveals the intensity (b) and the complex-valued object function (c). The intensity shows a non-uniform distribution, leading to the conclusion of a slightly misaligned object of beam drift. The phase of the exit wave is nearly flat, which can be derived by the homogeneous colors of (c). The PRTF (d) reaches its half maximum at $\sim 5 \mu\text{m}^{-1}$, which corresponds to a resolution of 200 nm. This can be confirmed by an analysis (e) of the edge, marked with the white-black line in (b) using the 10/90 criterion (blue: measurement, red: fit).

Reconstruction parameter			
Update function:	RAAR + OSS, $\beta = 0.9$	Support:	Dynamic, autocorrelation
Iterations:	1000	Constraints:	Positivity

5.3 Plasma investigations via ptychographic reconstructions

From fusion dynamics in stars, over terrestrial lightning events, to new prospects of energy production [90, 91] or novel light sources [52, 86, 92], hot dense plasmas are of importance for an array of physical phenomena. Highly ionized plasma, where the ions are multiply charged and the degree of ionization rises above the sub-percentage regime, are, therefore, an important current research topic [93, 94]. Determining important plasma parameters such as electron density and temperature profile in a hot plasma is of widespread importance, for instance in nuclear fusion research, uniform shockwave formation in z-pinch experiments [91] or stable confinement conditions in temperature-based fusion setups [90]. Table-top particle accelerators based on the plasma wake-field effect have the ability to implement high energy research to the lab-scale and pave the way to easy access particle and radiation sources for materials science or medicine where optimized spatio-temporal ionization profiles in the host plasma lead to large accelerating gradients [95]. Furthermore, plasma-based radiation sources provide a wide array of radiation from the visible to the X-ray regime and enable applications from spectroscopy [96] to lithography [97]. The properties of the radiation depend on the generation process of the plasma. Spatially and temporally highly coherent and directed radiation [52, 86, 92], as well as diffuse incoherent illumination [72, 98, 99] can be achieved. Understanding and classifying the inherent effects taking place in this extreme kind of matter is, therefore, a crucial part of exploring the surrounding nature or enhancing technology. While plasma generation is in most cases straight-forward, analyzing its composition is non-trivial. Due to the plethora of internal processes taking place (excitation, recombination, collision, etc.) and the turbulent nature of the gaseous media, the observation methods have to be highly adapted to the plasma conditions. An insight with conventional methods like interferometry [100] or shadowgraphy [101, 102] become increasingly difficult with higher temperature and density due to a higher number of free charges. Electromagnetic waves with frequencies below the plasma frequency cannot percolate the plasma and getting reflected and absorbed,

because of the in-phase oscillating free electrons. Higher frequencies however getting transmitted, if there are no absorption resonances of inner atomic shells. In this case, the wave can pass through the medium and experiences phase shifts dependent on the local plasma density. Interferometric techniques couple to this effect to reveal an electron density profile using Abel inversions assuming constraints like radial symmetries and a certain ionization states [103, 104]. These approaches use a pump-probe-like setup with a plasma creating beam and a probe beam, which passes the plasma and getting recorded by a 2D sensor. A full characterization of the ionization states in their spatial distribution is hardly realizable with these techniques. However, the following procedure uses the emitted light of the seeded SXRL to reconstruct the inner structure of the plasma channel. The seed, acting as a probe and traveling through the channel adopts the effects taking place and changes correspondingly. Determining the complex-valued emitted light field and comparing it to Maxwell-Bloch simulations validate the model and gives access to the ion and electron distributions in the channel. The main principle is pictured in Fig. 5.8 and works as follows:

Ptychography allowing the reconstruction of the complex valued illumination and therefore free-space propagation of the field. By using as less well-known optics as possible, the illumination can be back propagated to its source with low errors. In the moment, the propagated wavefront reaches the outer shell of the plasma source, the propagation has to stop, because of the unknown zoo of wave-changing effects taking place in the hot, dense regime. At this point, the measured exit-wave of the emitter is fixed. With the starting conditions (pumping conditions, seeding), the inner processes of the plasma channel can be calculated via 4D Maxwell-Bloch simulations, resulting in a simulated exit-wave. By comparing the simulations to the measurement, it is possible to reconstruct the inner, spatially resolved ionization states and electron densities.

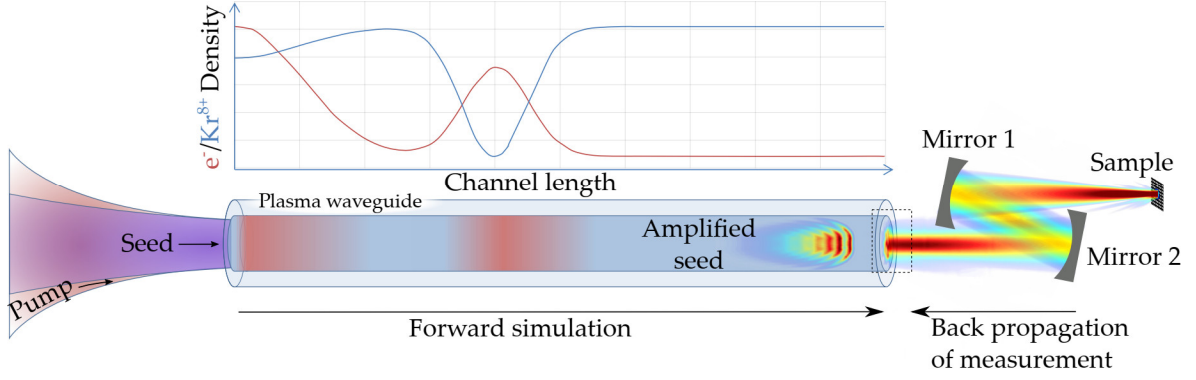


FIGURE 5.8: Principle of the backpropagation experiment. The reconstructed illumination function at the position of the sample is backpropagated through freespace over two mirrors, ending at the position of the laser plasma amplifier. The so gotten measured exit wave is compared to the simulated exit wave in forward direction. The simulated exit wave is the time-accumulated seed, which interacts with the plasma conditions during forward propagation. The e^- and Kr^{8+} density has no physical meaning here and only serve as an example.

To implement Ptychography successfully, the coherent beam diameter has to be known to derive a sufficient scan map. Here, results of the previous single-shot experiments were used to create a spiral-shaped map with 30 scanning points assuming $5.6 \mu\text{m}$ coherent diameter resulting in 90% overlap between neighboring illumination spots. A spiral map is necessary to avoid the so-called *raster-grid-pathology*, which leads to interference between the Cartesian computing grid and a rectangular scanning grid [25]. For easier beam alignment and a larger FOV, the QuantfoilTM-sample of the previous coherence measurement was used. Due to the beam fluctuations, the sample was scanned five times, independently reconstructed and the illumination function were averaged as follows:

$$\bar{\hat{\mathbf{P}}} = \frac{1}{5} \sum_{n=1}^5 \hat{\mathbf{P}}_n \exp(i\phi_{n,\text{offset}}) \quad (5.3)$$

An offset phase $\phi_{n,\text{offset}}$ has to be added to every illumination $\hat{\mathbf{P}}_n$ to avoid vanishing of the real part. The illumination function, shown in Fig. 5.9b, has, from a first view, a Gaussian-like profile with modulations. The FWHM of $(5.3 \pm 0.1) \mu\text{m}$ agrees with the previous measurement of $5.4 \mu\text{m}$. With a view to chapter 6, the probe and object was analyzed regarding its physical reliability to ensure stable results.

To retrieve the exit wave of the laser plasma amplifier, backpropagation has to be performed. Using an adaptive angular spectrum propagator [82], the field can be

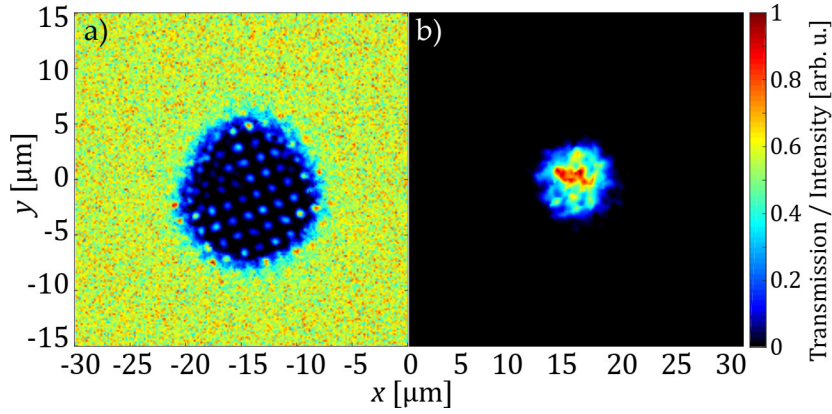


FIGURE 5.9: Reconstructed object (a) and probe (b). The noisy data around the object with the hole pattern arises during the reconstruction. The algorithm assuming a random complex-valued field to as a starting condition. The reconstructed and averaged probe shows a complex structure. An azimuthal average of the probe enables FWHM measurements, resulting in $5.3 \pm 0.1 \mu\text{m}$.

Reconstruction parameter			
Update function:	ePIE, $\alpha = \beta = 0.9$	Probe:	Start after 5I, update every 10I
Iterations:	1000	Constraints:	Positivity

free-space propagated. The two mirrors were applied as phase shifts: The curvature r as a radial phase shift overlaid with a phase ramp equivalent to the tilt of $\alpha = 4^\circ$:

$$\Phi_{\text{mirror}} = \exp\left(i\frac{2\pi}{\lambda}\sqrt{r^2 - x^2 - y^2}\right) \exp\left(i\frac{2\pi}{\lambda}\tan(\alpha)x\right) \quad (5.4)$$

A critical step is to finding the absolute position of the exit wave. After applying the last phase shift (mirror 2), the beam propagates convergently until it reaches the virtual focal point, where the phase shifts by π (Guoy phase) and the beam starts to diverge. Near the virtual focal point, the complex field was propagated in slices of 10 mm, to match the physical focal point, where the field reaches its most compact form (Fig. 5.10). Independently done precision measurements of the mirror-source distance confirm the overlap of numerical and physical focal point.

Due to the lateral extension of the field with increasing propagation distance, the FOV had to be adapted dynamically. Therefore, the distance between the signal and the edge of FOV was measured. If the distance falls below a certain threshold, the propagation stops, the FOV was extended via zero padding and the propagation starts again from the new position. This procedure loops until the desired

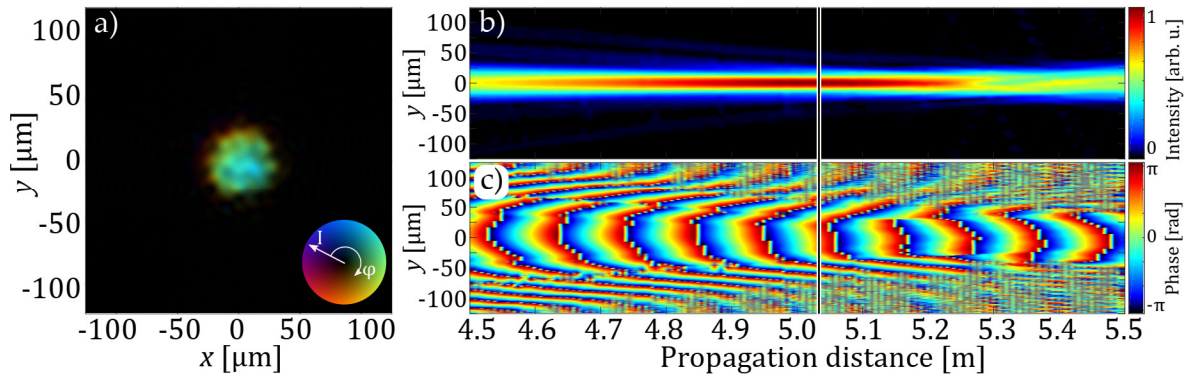


FIGURE 5.10: Backpropagated probe. The complex-valued exit wave (a) was determined using sliced propagation. In a vicinity of 0.5 m around the numerical focal point, the field was propagated in 10 mm slices to obtain the slice with the most compact intensity distribution in the y direction (b). A phase plot (c) of the propagation show the transition from convex to concave wavefronts near the chosen slice, marked by the black bar. Note: The observable wavelength in the phase plot of 0.1 m emerges of an aliasing-like effect and does not represent the real wavelength.

propagation length is reached. The now won exit wave of the laser plasma amplifier has to be compared to forward simulations. Spatial and temporal Maxwell-Bloch-simulation were used to model the propagation of the seed beam through the highly excited plasma. The amplification of the HHG-seed was modeled using the 3D Maxwell-Bloch code *DAGON* [105]. Using the slowly varying envelope approximation, the code is able to solve the Maxwell wave equation for the paraxial electric field. *DAGON* uses additionally polarization depended rate equations for the upper and lower level populations for the lasing ion. The temporal behavior of the pumped plasma is derived using the collisional-radiative code *OFIKinRad* [106] with particle-in-cell (PIC) modeling [107, 108] using *WAKE-EP* [109] and *Calder-CIRC* [110]. The profile of the plasma waveguide was derived from previous experimental results [86] combined with hydrodynamic simulations [107] using *ARWEN* [111]. The simulation assumes radial-symmetric ion and electron distributions. Therefore, the following results are pictured in a coordinate system, containing the channel length z and the radial dimension r .

Fig. 5.11 shows the results of the electron and lasing ion distributions along the plasma channel. Higher electron densities corresponds to higher ionization states explaining the lower Kr^{8+} abundance in the center of the plasma channel, where the electron-density peak arises. The sudden rise of the electron density marks the position of the pump pulse. The modeling of the plasma waveguide assuming a

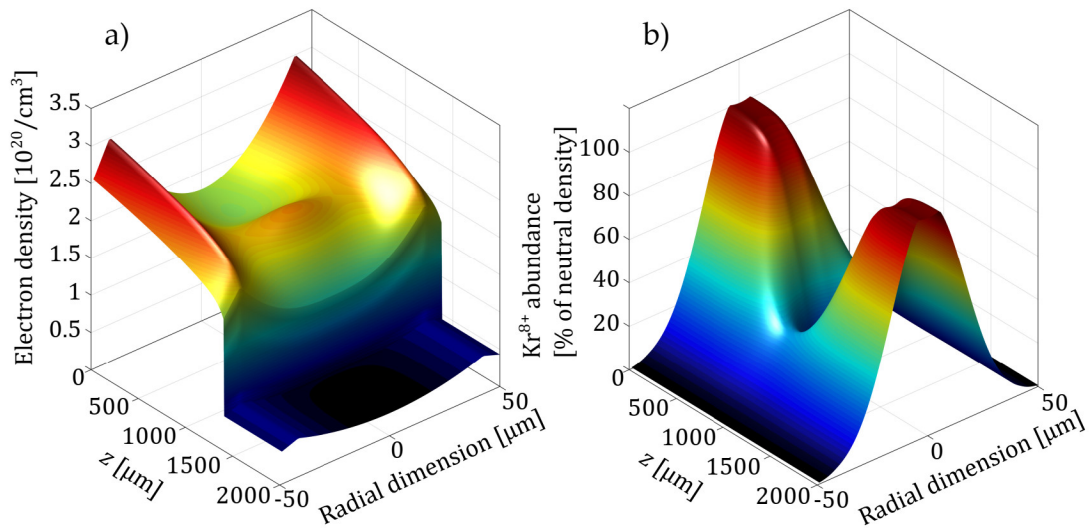


FIGURE 5.11: Spatial distribution of electrons and lasing ions in the plasma amplifier following the NIR pump pulse. Electron density profile of the plasma waveguide after propagation of the pump pulse to $z=1200\ \mu\text{m}$ a). Lasing ion (Kr^{8+}) abundance in the plasma in percent of neutral density after complete propagation through the channel. The lasing ion is depleted at $z=1000\ \mu\text{m}$ at the radial center due to overionization. Thus, the electron density profile shows a corresponding peak in this region. Furthermore, b) point out a groove of decreased ion abundance for $r=0\ \mu\text{m}$, resulting in an attenuated amplification, explaining the dip in intensity observed in the experiment (Fig. 5.13).

radial Gaussian profile for the ion abundance with a flat top near the center of the plasma channel, as given by the PIC simulations, resulting in a overionization. Self-focusing effects in some regions increase the intensity of the pump beam, attaining the threshold to generate higher charge ions. Thus, Kr^{8+} is depleted in this regions with a corresponding higher electron density. To get a artificial exit wave to compare to the measured one, a simulated seed has to propagate through the previous modeled plasma. The duration of the simulated HHG-seed is $\sim 300\ \text{fs}$, matching previous measurements [86]. The propagated XUV seed at the end of the channel in Fig. 5.12 becomes richly structured induced by the inhomogeneities of the plasma. Temporal oscillations (Rabi oscillations between $3d^94d$ and $3d^94p$ states) with a period of $80\ \text{fs}$ are visible as well as intensity isocontours with curved profiles, induced by the radial distribution of the plasma waveguide.

The projection in Fig. 5.12 in the propagation direction is done by accumulating the signal in the corresponding direction and represents the radial profile of the expectable exit wave. Instead of a Gaussian profile, the accumulated signal shows a

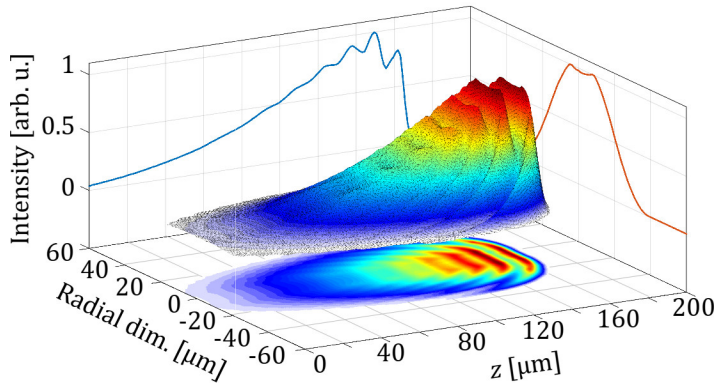


FIGURE 5.12: Simulated propagated seed at the end of the plasma amplifier. The projected profiles represent the accumulated intensities over the corresponding direction. The projection in the radial direction therefore represents the expectable radial profile of the exit wave and shows a dip in the center. The beam shows a rich structure with temporal (Rabi) oscillations.

dip in the central part. The parabolic radial profile along with the overionization in the plasma channels center leading to this two-peaked structure. This data can be compared to the measured one to validate the plasma conditions during the experiment. Therefore radial profiles of phase and intensity of the measured exit wave are taken to compare it to the accumulated seeds profile.

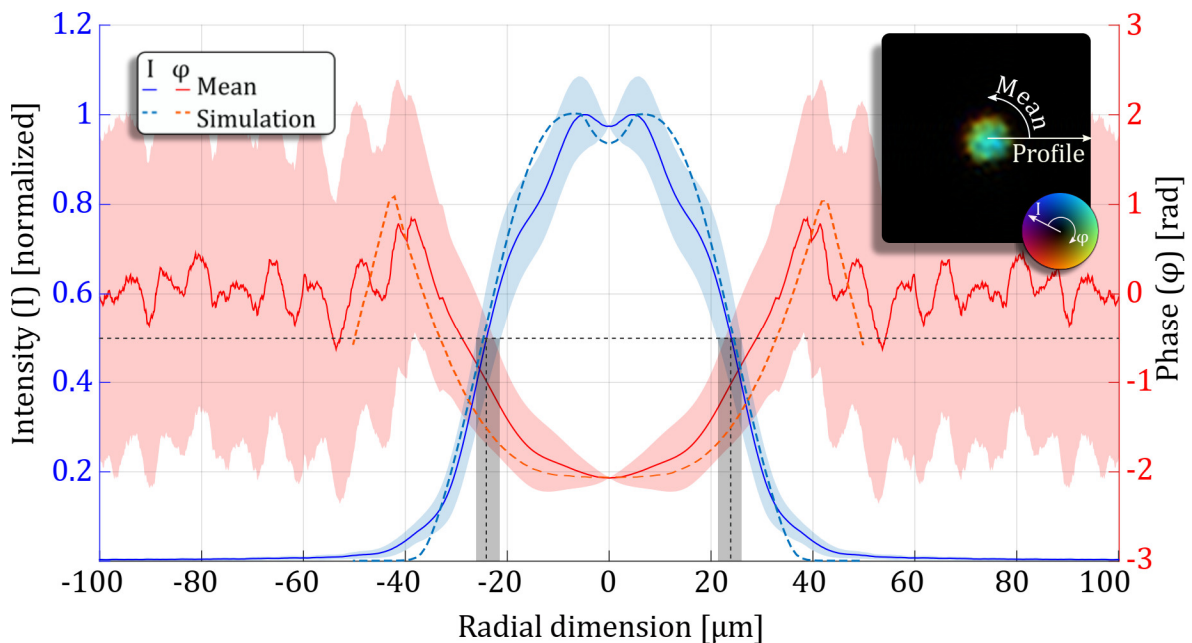


FIGURE 5.13: Comparison between measurement and simulation. Radial profile were taken from the intensities and phases. The inset show the method of gathering the radial profiles via azimuthal averaging. The derived FWHM of the measured plasma channel of $52 \pm 4 \mu\text{m}$ matches the FWHM of the retrieved probe comprehending demagnification of 10. The high standard deviation of phases above $+40 \mu\text{m}$ radial coordinate emerges from the algorithm due to low intensities. Pale colors indicate errors.

Fig. 5.13 shows the overlaid profiles. The central dip of the simulated profile appears also in the measured data due to overionization of the central part of the

channel. The parabolic phase emerges from the radially decreasing electron density and the accompanying decreasing refraction index.

It is important to say, that the whole procedure only capture the coherent parts of the radiation. The reconstruction of the probe only register the coherent illumination, therefore the backpropagated exit wave also only considers coherent radiating parts of the plasma. This goes hand in hand with the need of the angular spectrum propagator for well-defined phases and was considered by the simulation. The complete diameter of the plasma channel was measured before to $\sim 100 \mu\text{m}$. Hence, effects leading to non-coherent radiation are not included.

5.4 Summary

In this chapter, a HHG-seeded SXRL was used on the one hand as an highly coherent source for performing ultrafast single shot diffraction imaging and on the other hand as a test system for a sophisticated method of characterizing ionization states in a high density plasma. The first section verified important beam characteristics for diffraction imaging such as wavefront stability and lateral coherence. Fitting a 2D Gaussian function to a reconstructed object, consisting of regular holes, give access to the lateral coherence parameter of $5.6 \mu\text{m}$ FWHM in the focus. This equates to 40 % of the overall illuminated area. This value define the maximum size of the later objects used for non-scanning CDI, to not violate the Nyquist limit. A beam stability analysis using image correlation show beam distortions during subsequently taken shots. Only 34 out of 100 recorded diffraction patterns were suitable for further image processing and reconstruction. Within the 75 % criterion, valid images can be coherently stacked and increase the FWHM of the corresponding PRTF from 4.8 to $6.3 \mu\text{m}^{-1}$ transferred momentum. Afterwards performed single shot measurements without correlation for complete unknown samples result in stable reconstructions. The resolution measured in the object space (edge fitting, 10/90 criterion) matched the resolution measured in k-space using the PRTF (FWHM criterion) to $\sim 200 \text{nm}$. Here one has to say, that the two used criteria are just commonly used ones and are not somewhat connected. Using the 1/e criterion for the PRTF measurement would

result in Abbe-limited resolution of ~ 70 nm due to the high transferred momentum. The same apply for the 10/90 criterion in the object space. The high coherence of the source, in comparison to other table-top, high flux, plasma based XUV sources [16, 52], enables it to be a well-suited test system for plasma characterization experiments. Using the ptychographic reconstructed, complex-valued illumination function and guided backpropagation, the exit wave at the end of the plasma channel could be retrieved. Sophisticated forward simulations were used to model the plasma channel and propagate a HHG-seed pulse through it, to compute a corresponding lasing output. With matching exit waves, the inner ionizational structure can be derived. While spatial filtering by the amplifier gain is usually expected to clean up the beam profile, here a modulated wavefront is observed, indicating an inhomogeneous distribution of the gain medium. The central dip in the measured radial intensity could be traced back to an overionization in the plasma channel, leading to a decrease in the amplifying Kr^{8+} ion density to $0.4 \times 10^{10} \text{ cm}^{-3}$ and local increase of the electron concentration. This overionization limits the upscaling of this SXRL concept. More general spoken, the results state boundaries for laser-based generation of hot dense plasmas with well-defined ion compositions. The experimental validation of the used models holds great promise to employ these numerical methods to predict future laser-plasma-amplifiers and SXRL schemes. Finally, the observed Rabi oscillations in the LPA lead to strong modification of the temporal structure of seed pulses. This approach of modulating XUV pulses could open possibilities for e.g. Qubit state control [112] or tracking of electronic [113] or molecular [114] dynamics and is highly stable due to the fixed transition dipole moment.

Chapter 6

Ptychographic imaging of periodic structures

As ptychography allows imaging with wavelength-scale resolution in a wide spectral range, it has been successfully applied to image a huge variety of samples including periodic structures such as photonic crystals [115], to unwrap its lattice structures [116], and optical components like zone plates [117]. Due to the arbitrarily large field of view combined with the possibility of material sensitive reconstruction using wavelengths near absorption edges [61] or relative phase shifts [118], ptychography became also an interesting technique for imaging semiconductor devices [55]. Ptychography is not only useful to image the already processed wafer but, more recently, it has been used to inspect the lithographic mask, looking for defects on the size of the mask's smallest structures [119]. For all of these examples, as well as for recently done experiments within the scope of this work [89], it is necessary to reliably reconstruct periodic objects. It is well known in the literature, due to the quasi-periodicity of these structures, artifacts in the reconstruction can occur [120][121]. However, there exist techniques to get rid of these reconstruction artifacts [122] using additional knowledge either about the object or the illumination function. In the last year a tremendous growth of experimental work reporting on imaging of periodic samples with tabletop light sources in a wide spectral range has been noticed. All of them aim for high quality reconstructions requiring an estimation of the achievable resolution and criteria for judging the reliability of the reconstruction. Fig. 6.1 point out the problem concerning periodic structures. The

translation invariance of the Fourier transform causing identical diffraction pattern under a shift of the illumination function on highly periodic objects. Hence, the reconstruction converges quite fast under appearance of artifacts in the reconstructed probe and position refinement algorithms [24],[123] are no longer capable of determining the real scan positions. In this chapter, the limitations of ptychographic reconstructions for identifying small defects within otherwise periodic samples under realistic conditions, such as deviations of the scan points from the assumed positions, are investigated. The validity of solutions are checked by cross correlating the reconstruction with the original object and compare the reconstructed probes with the original ones. It was found, that small defects are only visible in the reconstructions, if the size of the defect is larger than the structure's period and the scan point deviations remains small in comparison to the defect size.

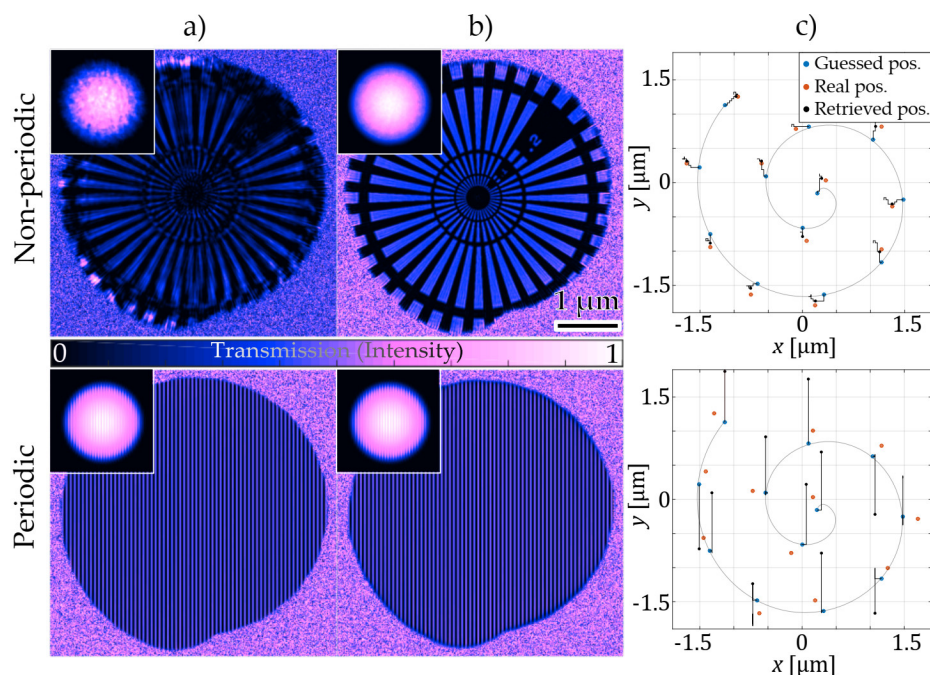


FIGURE 6.1: Motivation for a closer investigation of periodic structures in ptychography. If the positions of the illumination function (red in c) on the sample differs from the presumed ones (blue) during the reconstruction, the transmission of non-periodic objects and the corresponding illumination functions begin to blur (periodic, a). Position refinement algorithms like [24] are capable of adapting the presumed points to the real ones to ensure a successful reconstruction (periodic, b) (the scan sequence is indicated with a gray spiral). The reconstructions of perfectly periodic objects however are independent from position displacements (non-periodic, a,b) and position refining become not indicative (Non-periodic, c). Additionally, artifacts in the illumination function show up (insets in non-periodic,a,b). Here, the illumination functions (insets) are scaled down by a factor of 2.

6.1 Numerical model and methods

Imaging of objects larger than the coherent part of the illumination function is not possible for non-scanning CDI due to the violation of the isolation constraint [124] [34]. Ptychography imposes no limitations for the sample size because redundant data are obtained by multiple diffraction patterns recorded for different overlapping positions of the illuminating beam. However, new limitation can occur if the samples are periodic or the scan position is not precisely known and/or controlled. For example, the computing grid can interfere with the scan pattern resulting in artifacts, summarized under the *raster-grid-pathology* [25]. Similar difficulties arise for reconstructing large periodic samples due to the translation invariance of the Fourier transform. For an arbitrary large object illuminated with a well-defined beam, the intensity distributions of the diffraction patterns remains nearly constant under shifting the object within the illuminated area [34], if the period is smaller than the probe. For a ptychographic measurement of periodic samples, this effect implies similar diffraction patterns independent of the scan position. Additionally, in real experiments, the coordinate of each scan point is a crucial input parameter. The real position can differ from the assumed one due to the limited position accuracy of the sample holder, thermal drifts and vibrations in the setup or beam jitter. In general, determining and holding the exact scan position can only be ensured with enormous technical efforts. To account for these statistical deviations in the following simulations map distortions as position shifts between the points used for generating the diffraction pattern and the points used for reconstruction were introduced. Especially non-periodic objects are highly sensitive to this deviation, seen in Fig. 6.1 as the algorithm tries to overlay non-matching parts of the structure. For the simulation presented in this chapter, also the extended ptychographic iterative engine (*ePIE*) due to its robustness [38] was used. To compare the findings to previous experimental results [89], the following parameters were chosen: the photon energy is 68.6 eV, the distance from the sample to detector is about 23 mm, assuming a 2D detector consisting of 2048×2048 pixel with a size of $13.5 \mu\text{m}$, the reconstructed real space pixel size corresponds to 17.6 nm.

Similar to experimental situations an illumination beam with a Gaussian intensity distribution and FWHM width of $5\ \mu\text{m}$ and soft cutoff to zero outside of the probe's area was used, to mimic a cutoff pinhole right in front of the sample. For creating the data-set, a spiral shaped scanning pattern was created seen in Fig. 6.2 with an overlap between consecutive scan points of 90%. The above mentioned map distortion was realized by shifting a scan point of the map to an arbitrary position within a circle with a fixed radius r around the original position with a randomly chosen angle θ as seen in Fig. 6.2. The reconstruction needs a first guess of the probe, which is in this case a disc function with a diameter of $7\ \mu\text{m}$, which enables the probe reconstruction to shrink down. For the algorithm, the feedback factors α and β [38] (see Eq. 2.31 and 2.32) were set to 0.9 and claim the real space feedback between two subsequent iterations of object and probe reconstruction.

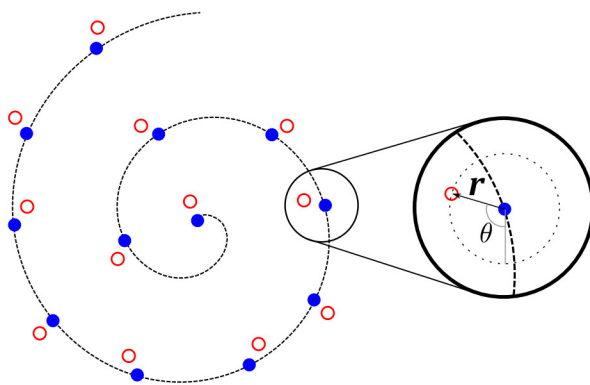


FIGURE 6.2: Principle of simulated map distortion. Every point of the scanning map (blue dots) is shifted by a distortion vector \mathbf{r} with a randomly chosen angle θ and a fixed length $|\mathbf{r}|$ and represent a distorted scanning point (red circle) for generating the diffraction pattern.

As a measure for the quality of a reconstruction, the sum squared error metric (SSE) (Eq. 2.25) was used.

6.2 Simulation results

To point out the reconstruction differences between non-periodic and periodic objects, a binary Siemens star as an example for a non-periodic object due to its wide range of structural varieties and the possibility to compare the finding with previous works was chosen. In the object, the structure size varies from $1\ \mu\text{m}$ down to $10\ \text{nm}$ over a total possible field of view of $40\ \mu\text{m}$. Fig. 6.3 shows the reconstruction of a Siemens star sample recorded under the conditions described above. The presented results demonstrate the importance of the accurate knowledge of scan positions for

the quality of the reconstructed object. With increasing map distortion, the reconstruction quality of the retrieved object decreases rapidly. It is also remarkable, that increasing the number of iterations will not improve the error anymore, pointing out a converged algorithm and therefore a stable solution.

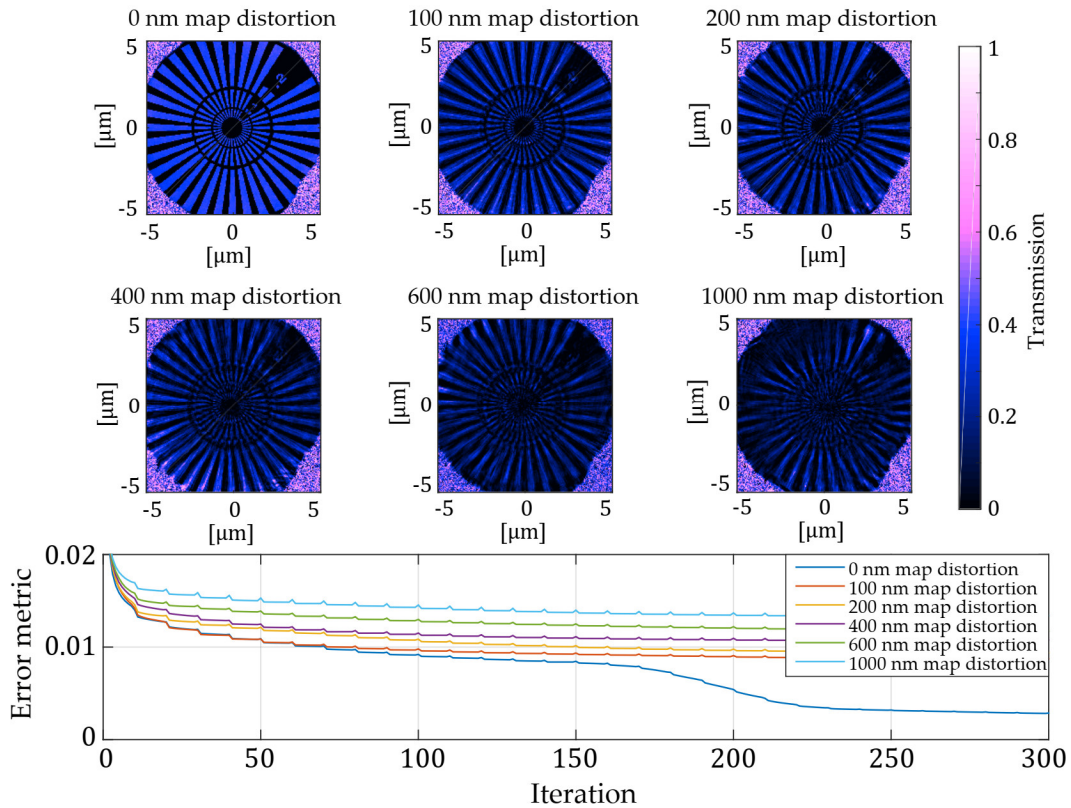


FIGURE 6.3: Reconstruction of a Siemens star with increasing map distortion. The error metric shows the decreasing convergence of the algorithm with increasing map distortion matching the structural decay of the object function.

The algorithm tries to enforce the reconstruction of a part of the object at a wrong place. In the next iteration, this part of the object will be overwritten by another misaligned part, which results in vanishing of the complex valued object function until a stable solution is reached. To conclude, already rather small map distortions around 100 nm lead to a different convergence behavior (Fig. 6.3. bottom graph) and to a lower image contrast. In a next step the influence of map distortions on the reconstruction of periodic objects are evaluated. As a periodic test pattern, a binary grid with a 200 nm period p was assumed. Simulation results for the periodic sample using the same set of experimental parameters as for the non-periodic case are shown in Fig. 6.4. Due to the translation invariance similar diffraction patterns

can be obtained and the algorithm is always capable of matching different parts of the objects, independent of the magnitude or direction of the actual map distortion. For a more general discussion, the map distortion is specified in multiples of the period p .

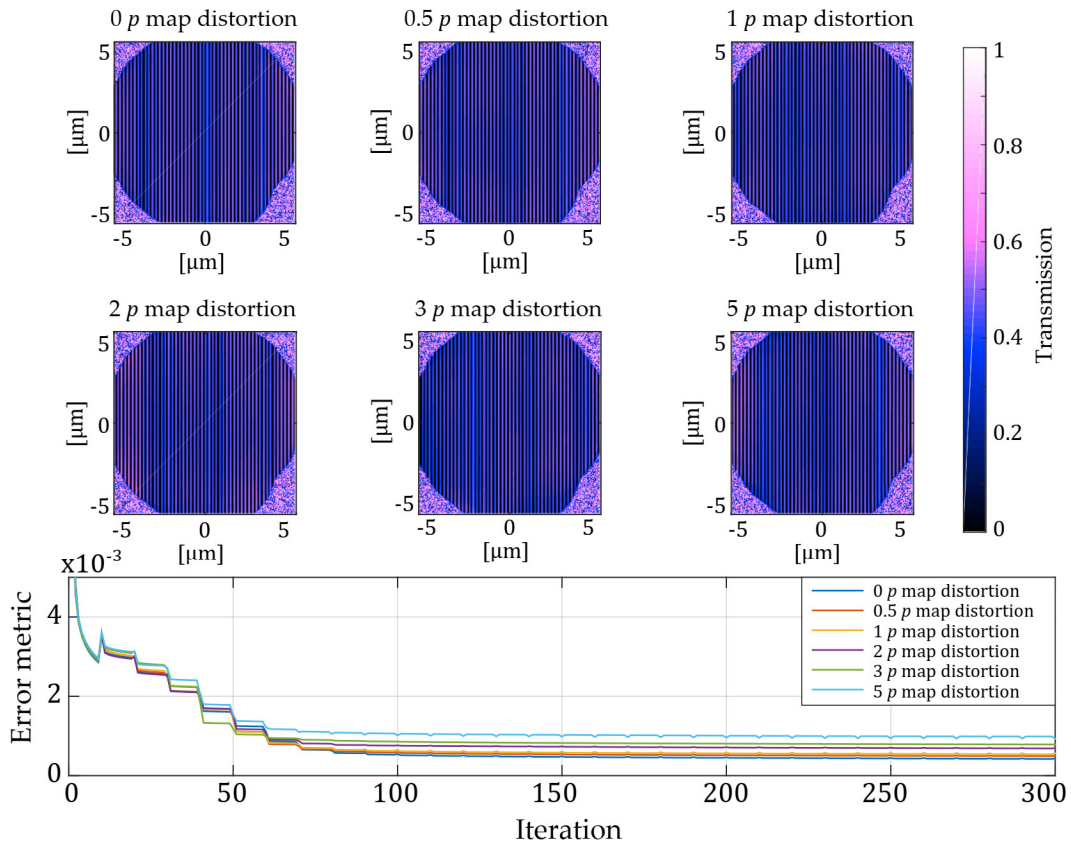


FIGURE 6.4: Reconstruction of a grid with 200 nm period assuming map distortions in multiples of the grid period p . Due to the periodicity, the reconstruction is independent of the map distortion. The error metric shows a similar convergence behavior with minor variations.

Fig. 6.4 shows the reconstruction behavior of the algorithm assuming map distortions. The convergence behavior does not change with the magnitude of the map distortion and reaches the minimal error after approximately 100 iterations. In comparison to the Siemens star sample, where the error metrics decrease with the deviation indicating a map distortion, for the periodic sample the evolution of the error metrics do not provide a hint on positioning faults. The indistinguishable reconstructions of periodic objects in ptychography leads to the question, whether the reconstruction reflects the correct image of the sample or not.

To answer the question above, a closer look will be necessary not only to the reconstructed object, but also to the reconstructed probe. Fortunately the *ePIE* algorithm is capable to provide the illumination function (probe), too. The probe and object reconstructions are coupled numerically due to the update functions [38] (Eq. 2.31 and 2.32). Based on this approach, it can be concluded that an insufficiently reconstructed object leads to a disintegrating probe beam reconstruction and vice versa. This can be used to validate the retrieved object transmission functions. Using the Siemens star of Fig. 6.3 as an object, Fig. 6.5 reveals an increased divergence of the reconstructed probes with the map distortion. To quantify the distortion, the image comparison coefficient (*ICC*), introduced in chapter 5 can be used, which compares two images and maps the similarity between 0 (no agreement) and 1 (full agreement).

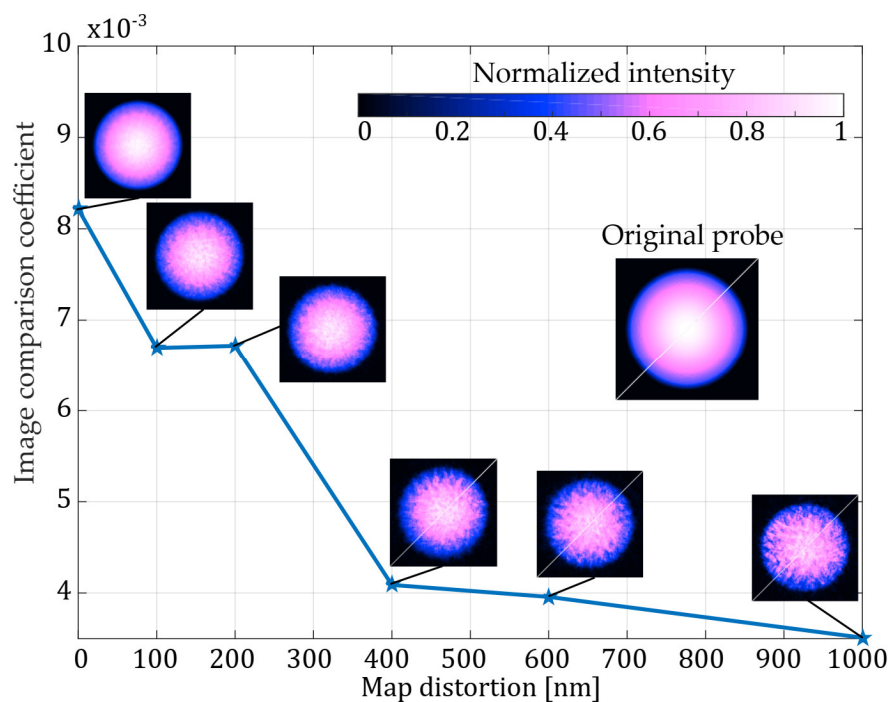


FIGURE 6.5: Comparisons between reconstructed probes of Fig. 6.3 and the original one. This comparison shows a dependency on the map distortion which, in turn, correlate to the contrast decay in Fig. 6.3.

A comparison of reconstructed probes of Fig. 6.4 lead to an imperceptible decrease in the ICC (compare to Fig. 6.1). Since for periodic objects the reconstruction quality does not change when distorting the scan map, the question rises how meaningful

ptychography with periodic objects is. To further address this problem, imperfections with increasing size were added to the otherwise purely periodic object to investigate if these small imperfections can be resolved. The addition of imperfection (defects) however may lead to small traces usable for the algorithm to converge to reliable solutions.

6.3 Defects

After the investigation of the influence of map distortions, it will be investigated whether small defects in otherwise periodic objects can be detected or not. After the first study regarding the influence of map distortions to periodic samples, the survey now is fixed on detection of defects with sizes in the order of the grid period. As shown above, the *ePIE* algorithm always converges to a stable solution for periodic objects. However, real life periodic structures often contain wanted or unwanted defects or imperfections such as dust particles on a lithographic mask or crystallographic perturbations. If the algorithm always retrieves a perfect grid, small defects may remain undiscovered. Especially for real life applications, it is indispensable to know the limitations of the chosen microscopy approach such as the minimum detectable size of defects with or without map distortions present. For testing the ability of the algorithm to detect defects, absorbing particles of different sizes on a periodic sample were assumed. Initially, disc like defects were placed on the grid and the diffraction pattern were recorded assuming an otherwise perfect experiment, i.e. no map distortions and all other parameters were stable. Fig. 6.6 shows an absorbing imperfection on a grid with 200 nm periodicity. Defects smaller than the period of the grid lead to absorption artifacts, but are not correctly reconstructed as objects anymore. The line outs of Fig. 6.6 show the decreasing transmission of the grid, where the defect is located. Note that the resolution according to the simulations settings is 17 nm, which is high enough to resolve all used defects.

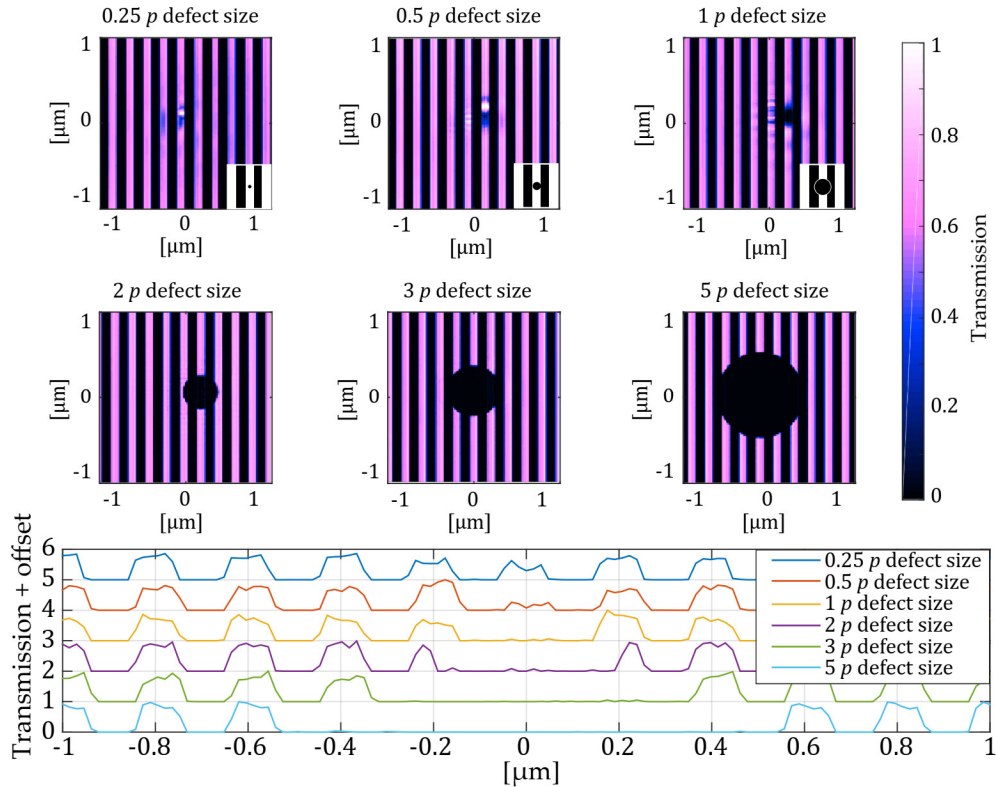


FIGURE 6.6: Reconstruction of different imperfections on a grid with 200 nm period assuming no map distortions. Defects smaller than the grid period are barely visible. The insets in the upper reconstructions show the objects used for the simulation as a guide for the eye. The line outs (bottom) show a reduced transmission at the smaller defects positions. The insets in the top row show the placement of defects for the simulation. Note, that the offset was chosen to separate the normalized line outs for a better visibility.

As described in the previous section, a convincing reconstruction of the object corresponds to a correct reconstruction of the probe beam. To quantify the quality of the image, the retrieved probe was compared with the input probe. Full agreement between the reconstructed and the real probe is nearly impossible due to the fact, that the reconstructed probe is the average over all scanning points and the measurement of the diffraction pattern can be only performed with a limited bandwidth. Thus, even for a perfect scanning map, one cannot expect an ICC value of 1. Therefore, the relative change of the ICC need to be evaluated to quantify the reliability of the reconstruction.

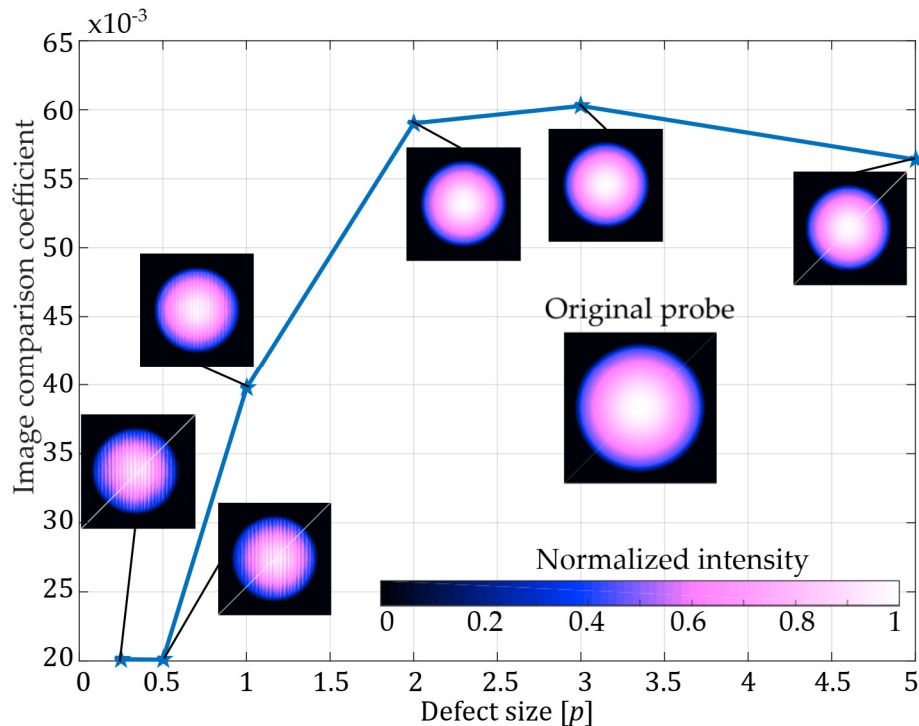


FIGURE 6.7: Comparison between the reconstructed probes used for Fig. 6.6 and the original probe. The probe reconstruction for small defects smaller than 100 nm (the grating period) show modulations, which results from the grid structure itself.

Fig. 6.7 shows the comparison between the reconstructed probes and the original one. Together with Fig. 6.6, one can see that the visibility of defects corresponds to the calculated ICC. If the defect is smaller than the grating period, the probes show modulations corresponding to the grating structure. For defects larger than the grating period (compare Fig. 6.6), the retrieved probes converge to the initial one without aforementioned modulations, implying a meaningful reconstruction of the object. Here, the strong diffraction signal of the periodic structure overlay the weak diffraction pattern of the defect, demanding a high signal-to-noise ratio (SNR) [125]. For real life samples, one can e.g. conclude that defects smaller than the wire size and period of an IC-bus are very difficult to detect with ptychographic methods or small variations in the crystalline grid may vanish during the reconstruction. Up to now the role of scan map distortion and local defects for the reconstruction of periodic objects were independently discussed. In a next step, the algorithms ability to converge if both of them are present simultaneously will be examined. Here, a defect with 200 nm diameter imposed on a periodic structure with 100 nm grid period is assumed. Note that this corresponds to a 400 nm defect on a 200 nm grid as

discussed before. The smaller grid period was chosen because it enhances the visibility of reconstruction artifacts due to a higher grid density for a constant field of view. With this setup, the algorithm's ability to retrieve images of defects assuming distorted scanning maps could be tested.

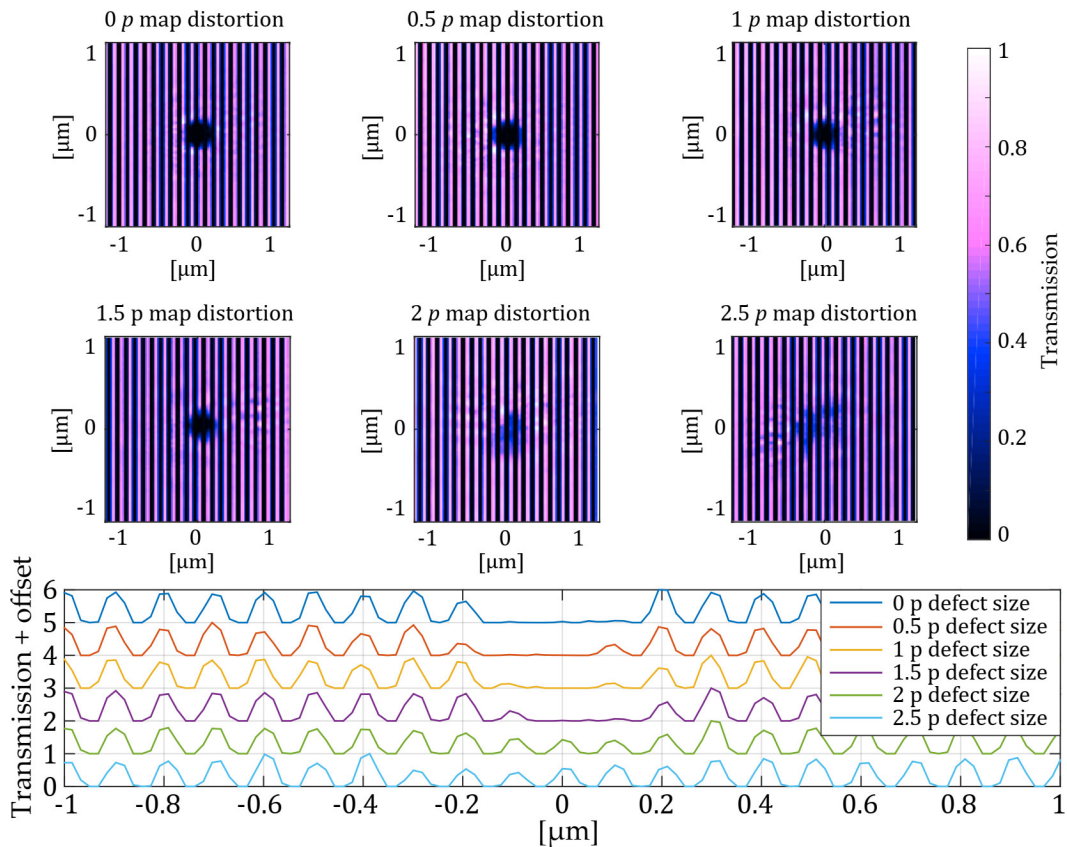


FIGURE 6.8: Reconstruction of the 100 nm period grid with a small defect of 200 nm with different map distortions. The defects starts to vanish when the map distortion reaches the defect size ($2p$), as a result, the reconstructed object appears quasi defect-free for large map distortions.

The simulation results as shown in Fig. 6.8 reveal that the grid structure in the vicinity of the defects remains unchanged, whereas the defect becomes almost invisible, if the map distortion reaches the size of the grid defects. The observation can be understood as follows. The algorithm matches patterns by using existing structures of the previous iteration. If the map misalignment reaches the size of the defect, there are no patterns from the previous iterations to match, resulting in a mixture between the grid structure with the defect and the misaligned scanning points, which appears like a defect-free grid due to the reduced contrast. Thus, under realistic

conditions with no precisely known scan point positions, such defects cannot be detected with standard ptychography algorithms. A test with position refinement also stops to converge (see Fig. 6.1), if the map distortion reaches the size of the defect. Fig. 6.9 shows the similarities between the probes of the reconstructed dataset of Fig. 6.8 to the original one. The ICC starts to decrease, if the map distortion reaches the size of the object, matching the loss of defects information in Fig. 6.8.

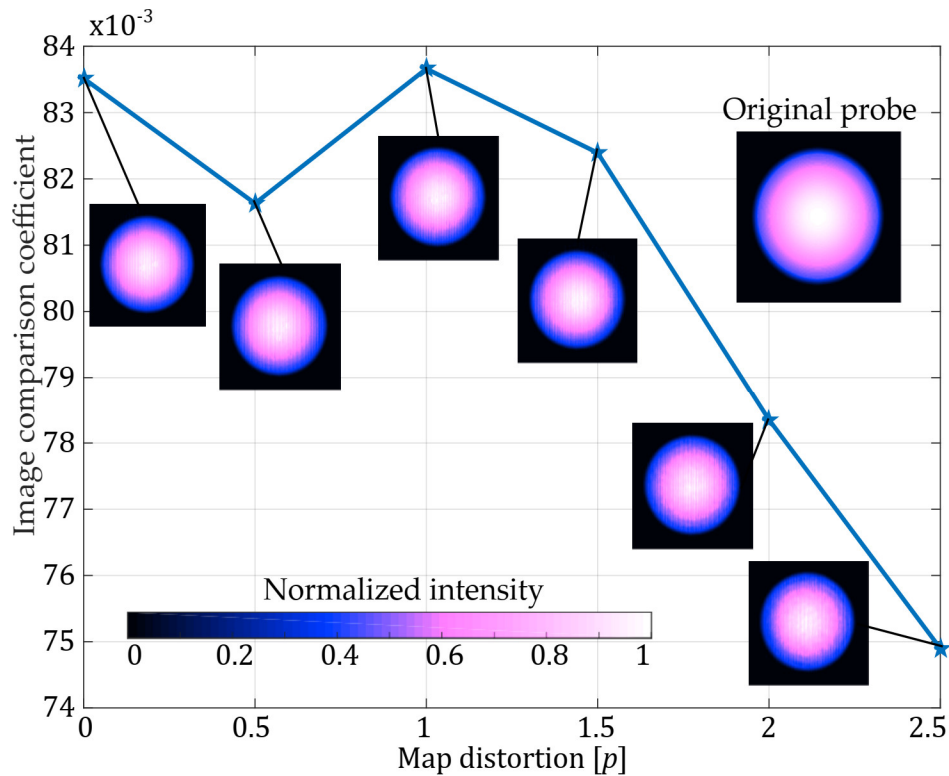


FIGURE 6.9: Comparison of the reconstructed probes with the assumed input probe for generating the dataset. The ICC starts to decrease, if the map distortion reaches the size of the defect. This behavior matches the structural decay of the objects in Fig. 6.8.

6.4 Summary

Ptychography is a powerful state-of-the-art lensless imaging method for short wavelengths illumination which is applicable to many different real world objects in science and technology. However imaging samples containing periodic structures can end in erroneous reconstruction results which can be identified by the appearance of modulation in the retrieved probe beam. Considering the coupled update functions Eq. 2.31 and Eq. 2.32, a reconstruction of the object is valid, if the reconstructed probe beam is comparable to the real probe beam, i.e. it should have the same intensity distribution and curvature of the wave front. In this way these findings are similar to previously reported approaches, like in [122]. There, a far field measurement of the probe was used as a-priori knowledge, to converge the algorithm on periodic objects. However, perfectly ptychographically reconstructed periodic samples suggest highest resolutions due to the apparently high contrast, despite scan map distortions. If the reconstruction is not reliable, a resolution measurement could also be corrupted. Therefore, a comparison of reconstructed and measured probe has to be taken into account as a criterion for validating the reconstruction.

This chapter highlighted the role of scan map distortions, due to e.g. thermal drifts and/or imperfect positioning of the sample, for the correct reconstruction. Non-periodic objects show immediate degradation of the image quality for scan map distortions. On the contrary, periodic objects can be well reconstructed which can be understood by similar scan-to-scan-diffraction patterns. For real life quasi-periodic samples, a reconstruction seems always possible, but the validity of the reconstruction must be verified independently. This has been demonstrated by placing imperfections with different sizes in an otherwise periodic structure. To derive a criterion for a valid solution, the above-mentioned method of comparison for evaluating the quality of the reconstructed probe was applied. For different defect sizes, it was shown that the size of the distortion has a direct influence on the validity of the retrieved image. Despite the algorithms capability of resolving structures down to 17 nm for the mentioned experimental setting [89], defects within periodic structures have to be larger than half of the period to appear in the reconstructed object.

The situation becomes even worse, if defects in periodic structures are imaged in the presence of scan map distortions. For scan map distortions in the range of the periodicity, the defect becomes immediately invisible and only the defect-free periodic structures were reconstructed. In this case, even a map refinement algorithm like in [123] would not find a correct solution anymore and the object would not be reliable.

Summing up, imaging periodic structures with ptychography need particular attention regarding imperfections and map distortions due to the algorithms inclination towards physically invalid solution. A comparison between the reconstructed probe and a known one gives a criterion for valid object reconstructions. As a rule of thumb, defects have to be larger than the periodicity to be properly reconstructed and map distortions have to be minimized to a fraction of the periodicity to observe the non-periodic features in experimental setups like [89]. Real-life application often demand imaging of objects embedded in highly periodic structures. Here, an approach for imaging small imperfections could be using a dual-wavelength setup for separating the scattering signal of periodic and non-periodic parts. High dynamic range recording of diffraction patterns can also used to improve the SNR to amplify weak scattering signals of imperfections [125] under stable illumination.

Chapter 7

Synopsis

7.1 Conclusions

Beginning with the widespread use of lensless XUV imaging, the imaging of nano-scale objects, this work dealt with the full reconstruction of hidden structures and ultra-fast imaging of artificial samples with a few hundred femtoseconds of exposure time. Concerning the first point, CDI in reflection geometry was performed in a spectral range of 290 eV, in which the attenuation length of silicon exceeds 120 nm. Here, the spectral range was limited by the synchrotron itself in turn of well-controllable beam parameter. However, the attenuation length allows the detection of hidden layers at a depth of also 120 nm. The here used solid gold layer in a star-shaped pattern could be recovered with low distortion by the overlaying material with a lateral resolution down to 110 nm, dependent on the resolution criterion. The complex-valued reconstruction allowed roughness measurements of the hidden layer with sub-nanometer resolution due to the used small wavelength of 5 nm. Lensless imaging in reflection geometry of hidden structures in silicon therefore allows metrological measurements on integrated circuits and optoelectronics after processing and applying of e.g. passivation layers.

Using new approaches for tabletop XUV sources call out for determining their possibilities for lensless imaging procedures. Beside the high flux and overall coherence of a seeded SXRL, developed at *LOA*, extreme short XUV pulse lengths of 450 fs under maintenance of the brilliance is an additional highlight, calling out for lensless imaging applications. These properties allowing dynamic imaging on shortest timescales of e.g. macro-molecule clusters or electron migration. However, this

SXRL operate in single-shot mode with a frequency up to 10 Hz. For testing its abilities for high dynamic range imaging, binary, artificial structures were reconstructed in multi shot mode and reveal a shot-to-shot stability of 35 %. This knowledge was later used for determining the scan parameter for ptychographic experiments mentioned below.

Lensless imaging in the XUV offers more than just a pure reconstruction of the object with high resolution. The complex-valued object- and illumination functions reveal possibilities for sophisticated diagnostics usable in applied and fundamental science. During this work, different techniques were presented for characterizing the light emitting source to take conclusions about their inner and outer dynamics. Starting from a reconstruction of the lateral coherence and jitter of the Nitrogen-plasma of a water window source, it could be shown, that a single diffraction pattern enables conclusions about the mentioned parameters. Therefore, the long-exposed diffraction pattern was compared to simulations, considering the coherence and movement of the source. However, knowledge about the source is still necessary. To mention an example, the warping effects of the diffraction pattern can also occur from temporal incoherence. Therefore, it is required to ensure the responsibility of only one parameter for the effects, otherwise the solutions become ambiguous. Due to the physics of the used source, it is known, that the spectral width is rather small, so temporal incoherence could be neglected. With the presented method, the longitudinal jitter amplitude of the plasma could be determined to $(160 \pm 10) \mu\text{m}$, whereas the spatial coherence at the position of the sample could be calculated to $(11 \pm 1) \mu\text{m}$ (7.5 % of the total illuminated Area). This knowledge enables the pre-selection of objects, suitable for CDI and allow the construction of a scan patterns for ptychographic applications. However, a single CDI reconstruction of a known object would also lead to a rough estimate of the spatial coherence, though it requires a stable source. In this case, the warping effect would make false implication using CDI reconstructions. Going further and gathering an insight into the plasma, the basic principle of measurements and comparison to well-adapted simulation were

enhanced using a seeded SXRL. The seed itself served as a probing pulse, traveling through a highly excited Krypton plasma and experiencing different ionization states. These ionization imprints the seed like a stamp and changes its projection onto a detector accordingly. By using ptychographic imaging of an object, illuminated with the propagated seed, the complex-valued longitudinal projection could be retrieved. Backpropagation to its origin generate a picture of the exit wave at the surface of the plasma in the seed's direction. Comparing the amplitude and phase with the outcome of 4D Maxwell-Bloch calculations, the inner ionization states of the high density plasma could be retrieved and reveal overionized parts, which limits the rates of stimulated emission and therefore the maximum gain achievable with this SXRL concept. It shows that pure increased pumping not allowing to drive the yield accordingly and that e.g. enhanced geometries have to take place. Beside the outcome regarding the SXRL concept in particular, the presented technique allows gathering insight in many types of plasma light sources using longitudinal probing. Finally, the use of periodic objects in Ptychography opens several questions regarding the reliability of the solutions. The translation invariance of the Fourier transform, combined with the strong Bragg-peaks in the diffraction patterns, leading to misinterpretations during the reconstruction. This, however, hampers e.g. the detection of small defects on periodic structured such as integrated circuit or lithographic masks. Without additional refinement, the behavior of artificial defects in a periodic surrounding during ptychographic reconstruction was analyzed and it was found, that the reliability of the reconstructed object is directly coupled to the reconstructed probe. This was used as a criterion for several experiments to validate the reconstruction and defining a termination criterion for the algorithms.

7.2 Overview of experimental data and results

	Synchrotron (Chapter 3)	LPP (Chapter 4)	HHG-SXRL (Chapter 5)
Geometry	Reflection	Transmission	Transmission
Numerical aperture	0.06	0.05 (Zoneplate) 0.04 (Characterization)	0.24
Wavelength	4.28 nm	2.48 nm	32.8 nm
Sample	Silicon-gold-silicon stack	HEK293 cells on silicon Holed gold-plated carbon	Structured gold-plated silicon-nitride Holed gold-plated carbon
Exposure times	120 s	60 to 1200 s	450 fs (effective)
Resolutions	179 nm (edge, 10-90) 330 nm (PRTE, FWHM) 110 nm (PRTE, 1/e) 160 nm (Periodic features)	~50 nm (zone-plate, pixel resolution)	194 nm (edge, 10-90) 200 nm (PRTE, FWHM)
Special feature	Buried sample Roughness measurement	Labeled bio-imaging Single-shot source characterization	Ultrafast single-shot imaging Ion-state reconstruction
Important results	0.37 nm RMS roughness of buried layer at high lateral resolution	Carbon-resolved imaging 7.5% lateral coherence area ~(160 ± 10) μm axial jitter of plasma	Up to 194 nm lateral resolution at 450 fs exposure time Overionization found Limitation of SXRL concept

7.3 Outlook

7.3.1 Ghost imaging assisted CDI

As described in the fundamentals, the first step in CDI is to find a suitable support to confine the objects shape and position in the reconstruction plane. However, there exist different techniques to derive the support either out of the diffraction pattern e.g. via auto-correlation or setting a static support. The better the support fits the final shape of the reconstruction, the faster and more reliable is the reconstruction process. The best support therefore would be a direct image of the object or, at least, its rough shape. In the XUV, one can use e.g. zone-plate microscopy to estimate the outline of the object. Whereas this is clearly possible for artificial and insensitive samples, biological specimen would suffer from radiation damage as shown in chapter 4. Ghost imaging, introduced in chapter 2.2.5, however is a promising candidate to gather a vague outline of the object within reasonable process time under use of low radiation exposure. The radiation will still be present during the recording of the diffraction pattern, but a well-known shape of the object can compensate lost features of the diffraction pattern due to a reduced exposure time. Therefore, the overall dose should be decrease via a combination of Ghost Imaging and CDI. The additional expenditure would this kind of assisted CDI mostly recommendable for very sensitive samples.

7.3.2 In-situ diagnostics

Using CDI in reflection geometry as shown in chapter 3 enable measurements during e.g. deposition processed to observe material changes due to inserted heat or stress. Requirement for this would be a sufficient transmission within the processing chamber to ensure a high photon count on the detector. As an example, which shall be mentioned here is the process of plasma enhanced chemical vapor deposition. In semiconductor industry and research, this is a common procedure to cover already processed wafer with a passivation layer. However, beside the control of the layer thickness, an observation of mechanical stress of underlying layers is crucial. This however is controlled after the deposition process mostly via electron microscopy

and require damaging the sample. Reflection CDI in an adapted wavelength regime enable a damage-free in-situ measurement of roughness and shape and can be implemented during the layer growing process.

Different disciplines working with coherent radiation rely on stable sources with constant yields. In the best case, implemented sensors deliver a real-time feedback of the parameter to stabilize to ensure a closed-loop control. One of the simplest examples is a beam pointing stabilization by quadrant photodiodes: A part of the beam is separated through a beam splitter and hits a quadrant photodiode. Minimal derivations of the position on the diode will trigger a piezo-motoric system to counteract the unwanted movement. The procedure presented in chapter 4 to retrieve beam jitter and coherence could be used in a similar way. Again, a part of the beam could be separated and used for generating a long-exposure diffraction pattern. With a high-speed implementation of the mentioned algorithm, the coherence can be measured in a few minutes. Source properties can be adjusted accordingly. Here, the feedback loop is delayed with minutes and only suitable either for low-changing parameters or automatic test series.

Appendix A

Pre-processing of diffraction data

Recording images via a CCD camera, used in all of the following experiments, also captures several artifacts from different origins. These artifacts directly influence the outcome of phase retrieval algorithms or image analysis later used in this work. Hence, it is of exceptional importance to separate the wanted signal from unwanted noise under conservation of the signal's integrity. Fig. A.1 shows the typical pre-processing workflow, every measured diffraction pattern must pass in order to get feed into later algorithms.

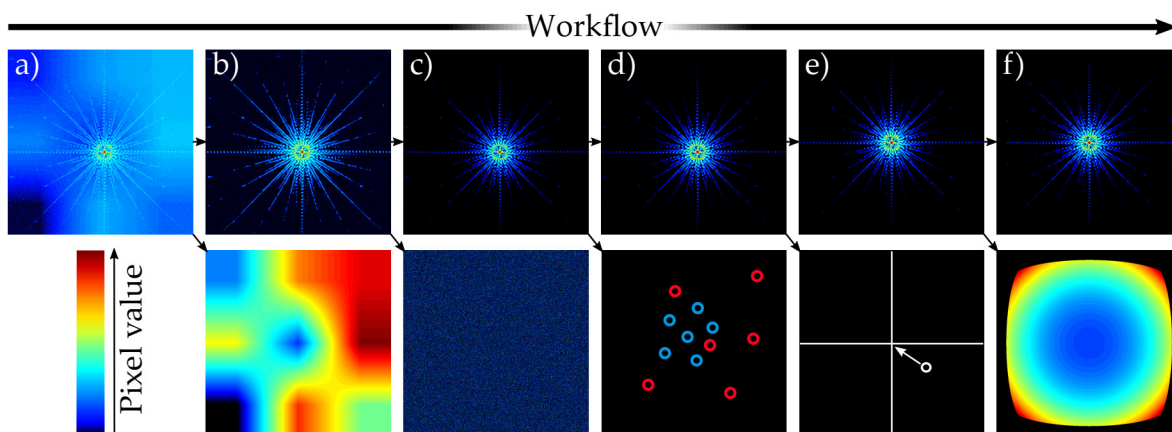


FIGURE A.1: Workflow for pre-processing diffraction data. The raw measured diffraction pattern a) first has to be disentangled from the complex-shaped background. The now background-free pattern b) has to be denoised (c) in order to find hot- and cold-pixels (d). After center the pattern (e), the intensity adaption and curvature respective tilted plane correction can take place (f).

Here, the order of sequence is of particular importance. Trying to e.g. centralize the pattern without preceding noise- and hot-pixel correction will lead to misinterpretations of the pattern's central position and curvature correction before centering will skew the diffraction pattern leading to distorted or impossible reconstructions. In

the next sections, every step of Fig. A.1 will be explained in detail.

A.1 Background correction

During the capture of an image, stray light from the main source or from an additional parasitical source can hit the detector, leading to a background signal. In a best case, the background signal is equally distributed over the detectors plane and can easily be subtracted. This flat background mostly occurs directly from the detectors bias (dark current, bias voltage etc.). Additionally to these flat backgrounds, parasitic light sources can generate a complex shaped background like in Fig. A.1b). These non-regularly offset must be identified and subtracted, otherwise it will be misinterpreted as spatial information [126]. The most intuitive way, to identify the complex background is to capture a dark-image with no signal but otherwise same parameters. However, stray light originating from the used source is mostly not covered by the dark-image. Therefore, in this work, a 2D surface is adapted to points of the image without wanted signal. This procedure requires either knowledge about the sample and therefore about the diffraction pattern, one can set a threshold value or the signal-less areas can be set manually. Points containing no signal are considered as background and are used for creating the 2D surface. The collected data points are used to interpolate the residual points on the grid using natural neighbor interpolation [127], also called voronoi- or dirichlet interpolation [128]. This kind of interpolation is preferable over simpler methods, such as nearest-neighbor interpolation, due to the smoother fit. It provides a fast interpolation without the need of finding a complex function, which is, indeed, advantageous in ptychographic application with large data sets.

A.2 Noise removal

Thermal and electronic noise, as well as defect pixels or cosmic radiation have several effects on the recorded pattern. Whereas thermal and electronic noise impact the image with a normal distributed noise floor with a certain range, defect pixels

are well-isolated and preserve either zero signal (cold pixel) or full signal (hot pixel) and are called in the next section. Cosmic radiation however lead to either single isolated spots or strains of overexposed pixel due to the high energy photons and must be separated manually. Goal of the noise correction should be cleaning the image without changing the wanted signal. Most of the normal distributed noise floor will be canceled by the background correction described before. The residual noise is removed by filtering high spatial frequencies with a Gaussian filter function, leading to smoothing of the image. Removing of high spatial frequencies can be seen equally as a convolution of the image with a Gaussian smoothing kernel [129], as described by the convolution theorem [130]:

$$A \odot f = \mathfrak{F}^{-1}(2\pi\mathfrak{F}(A)\mathfrak{F}(f)) \quad (\text{A.1})$$

With A as the diffraction data and f as the 2D Gaussian filter function with a certain variance. However, this procedure is only applicable, if diffraction features remain conserved and, therefore, oversampling is still provided. Hence, a trade-off between smoothing and feature loss is necessary and require manual balancing.

A.3 Hot- and Cold-pixel elimination

Defect pixels or perpendicularly incident cosmic radiation appear in the recorded pattern as pixels with zero intensity (in a non-zero vicinity), called coldpixel, or as pixel with values equal the dynamic limit of the detector (Hot-pixel). Naturally, cold-pixels are only detectable in areas, covered by signal and vanishing during the background correction. Hot-pixel however are visible over the whole image area. Due to the high contrast, these pixels can be localized by finding extrema of the horizontal and vertical gradients of the image [131]. Here, the order of consecutive extrema identify the type of pixel defect. If a maximum directly follows a minimum, a cold-pixel was found and vice versa for hot-pixel. In this way, every found pixel can be corrected by changing the value via linear interpolation of the surrounding pixels (see Fig. A.1d). However, a threshold has to be defined and adapted to every diffraction pattern, to ensure the conservation of high contrast diffraction features.

A.4 Centering

Not exactly centered diffraction patterns due to e.g. inaccuracies of the experimental setup, are equivalent to a non-perpendicular incident wave-vector to the detector plane. This, however, can be interpreted as an illumination of the object with a tilted wavefront. Hence, phase retrieval algorithms reconstruct non-centered diffraction pattern with a phase ramp in the best case. Insufficient oversampling combined with an off-center pattern however, become increasingly difficult to converge at all [126]. This unwanted effect can be avoided by aligning the diffraction pattern to the detector's center. Here, fast Fourier transform (FFT) enhanced auto-correlation, based on the Wiener-Khinchin-Theorem [35], is used to allocate the zeroth order of the diffraction pattern due to the increased computing speed. The inverse Fourier transform of the power-density-spectrum of the pattern equals to its auto correlation in the discrete form :

$$\hat{C}(m, n) = \sum_{m=1}^M \sum_{n=1}^N \hat{A}(x, y) \cdot \hat{A}^\dagger(x + m, y + n) = \mathfrak{F}^{-1}(|\mathfrak{F}(\hat{A}(x, y))|^2) \quad (\text{A.2})$$

Finding the coordinate of the maximum of $\hat{C}(m, n)$ enabling a shift to the detector's plane center.

A.5 Curvature and tilted plane correction

An object with the real-space coordinates x, y and the normal vector \mathbf{n}_o , illuminated with a plane wave under an angle of incident φ with the wave vector \mathbf{k}_i , scatters the wave in different solid angles with outgoing wave vectors \mathbf{k}_s . Due to energy conservation $|\mathbf{k}_i| = |\mathbf{k}_s|$, the scattered wave vectors \mathbf{k}_s point onto the Ewald sphere as seen in Fig.... In the Fourier- or momentum-space, the momentum transfer vector $\mathbf{q} = \mathbf{k}_s - \mathbf{k}_i$ is linearly distributed on a sphere with radius defined the distance object-detector. A flat detector with the size d_{det} and the normal vector \mathbf{n}_d record a skewed diffraction pattern because of the projection from the sphere onto the flat detector plane. The distribution of the momentum transfer becomes nonlinear. This skewed diffraction pattern lead to skewed objects after the reconstruction. To get

rid of these artifact, the nonlinear recorded momentum transfer has to be remapped onto the linear grid of the sphere. Furthermore, the projection onto the detector plane results in a decreased recorded intensity per pixel in dependence of q due to the constant energy transferred in a solid angle.

The projection from the plane onto the sphere can be done by calculating the non-linear grid for \mathbf{q} and defining map projection for the linear grid [132–134] or taking geometric considerations into account. In favor of fast calculations, here, the geometrical way will be followed.

One can derive the horizontal and vertical translations of the momentum transfer \mathbf{q} for remapping the detector plane to a sphere with a radius equal to sample-detector distance by interpreting the wavefront tilt as a horizontal shift of the detector plane with $\mathbf{n}_o = \mathbf{n}_d$ in real space. Here, the angle of incident φ is formed between the object's normal vector and \mathbf{r} pointing to the center of the detector. Thus, reflection can be reinterpreted as transmission under tilted illumination. In this way, the mapping can be simply calculated geometrically split in x and y component, suitable for a simple numeric implementation:

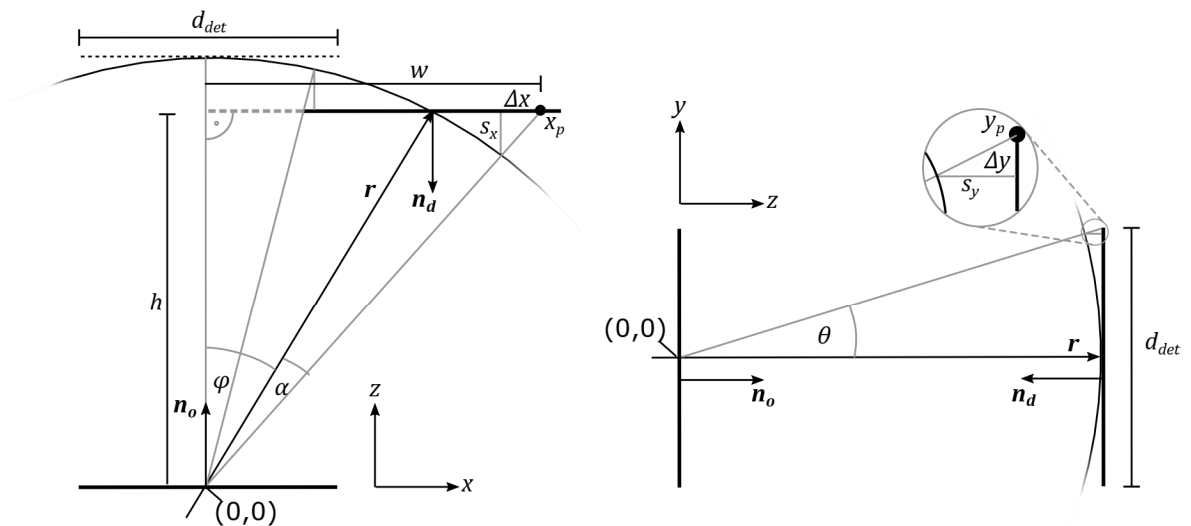


FIGURE A.2: Geometrical mapping of the detector onto a sphere. The necessary shift can be divided into x and y -components. The pre-calculated Ewald sphere $\hat{\mathbf{S}}(x, y)$ lead to connected equations for both components.

For the x -component:

$$h = \cos(\varphi)|\mathbf{r}| \quad (\text{A.3})$$

$$x = \sin(\varphi)|\mathbf{r}| + x_p \quad (\text{A.4})$$

$$\tan(\varphi + \alpha) = \frac{x}{h} = \frac{\Delta x}{\hat{\mathbf{S}}(x_p, y_p)} \quad (\text{A.5})$$

$$\Rightarrow \Delta x(x_p) = \tan(\varphi) - \frac{\hat{\mathbf{S}}(x_p, y_p)}{\cos(\varphi)|\mathbf{r}|} x_p \quad (\text{A.6})$$

for the y -component:

$$\tan(\theta) = \frac{\Delta y}{\hat{\mathbf{S}}(x_p, y_p)} = \frac{y_p}{|\mathbf{r}|} \quad (\text{A.7})$$

$$\Rightarrow \Delta y(y_p) = \frac{\hat{\mathbf{S}}(x_p, y_p)}{|\mathbf{r}|} y_p \quad (\text{A.8})$$

where $\hat{\mathbf{S}}(x_p, y_p)$ are the distances between the pixels x_p, y_p of the detector and the geometrical sphere in direction of \mathbf{n}_d presumed the center of the detector lying on the sphere:

$$\hat{\mathbf{S}}(x_p, y_p) = \Re \left(\sqrt{|\mathbf{r}|^2 - (x_p - \sin(\varphi)|\mathbf{r}|)^2 - y_p^2} \right) - |\mathbf{r}| \sqrt{1 - \sin(\varphi)^2} \quad (\text{A.9})$$

where the second term sets $\hat{\mathbf{S}}(0,0) = 0$ (no shift for $\mathbf{q} = 0$). The pixel coordinates x_p, y_p origin of the detector's center for a simpler implementation. For the y -component, y and y_p are identical. Due to the increasing distance of the sphere to the detector with increasing momentum transfer, the intensity of each pixel at the detector plane decreases due to the inverse-square scaling law. Hence, before the shifting getting applied, each pixel value has to be corrected via multiplication with its position depending intensity factor $1 + (x_p^2 + y_p^2)/|\mathbf{r}|^2$. After calculation of the shift matrices $\Delta x_p, y_p$ the intensity values of the diffraction pattern at position (x_p, y_p) were shifted to $(x_p + \Delta x_p, y_p + \Delta y_p)$, resulting in a projected pattern suitable for reconstruction. This procedure is also suitable for pure curvature correction for an AOI of 0° . Here Δx_p and Δy_p become only dependent on $|\mathbf{r}|$. For a numerical implementation, it is important to note, that the sampling onto the linear grid

demands a higher number of pixels and, therefore, an interpolation to conserve the oversampling ratio [134]. The sampling in reflection geometry becomes spatially dependent and increases with higher q_x [133]. The mapping onto a linear grid shrinks the more over-sampled parts to the oversampling ratio of low q_x and therefore requires a higher resolved grid.

A.6 Additional processing: High dynamic range

The decreasing flux with increasing spatial momentum q call out for long exposure diffraction pattern. The limited dynamic range of cameras (footnote: Typical 12 (0 to 255 counts) to 16 bit (0 to 65535 counts)) and the capacity well per pixel limits the intensity resolution and the total recordable flux. Higher flux leads to a saturation of pixel resulting in an overflow of charges to neighboring pixels. As a consequence, Low- q signals are lost in the oversaturation and are therefore not available for reconstructions. On the other hand, reducing the flux goes with loosing high- q signals. Hence, single shot diffraction pattern with recording of the highest momentum signals is somewhat challenging and requires high capacity CCDs with a high dynamic resolution. A well-known technique to overcome these restrictions is the combination of high exposure time images with low exposure images, containing mostly low- q information, to a HDR image. The long exposure images can be recorded using an additional beamstop to block the high intensity zeroth diffraction order to prevent overflowing of charges. There exist different techniques to merge the images [135, 136] which rely on the same principle of masking, intensity adjustment and combining as seen in Fig. A.3.

First, the overexposed or beamstop covered signal of the long exposed image has to be marked by selecting pixel values greater than a threshold, resulting in a binary mask \hat{M}_{HDR} . This area has to be replaced by the intensity adapted short exposed signal. Therefore pixels have to be selected, which contain signal in both images. In this work, the pixels on a circle slightly larger than the overexposed areas are used for intensity adjustment. The intensity adjustment factor now can be calculated by

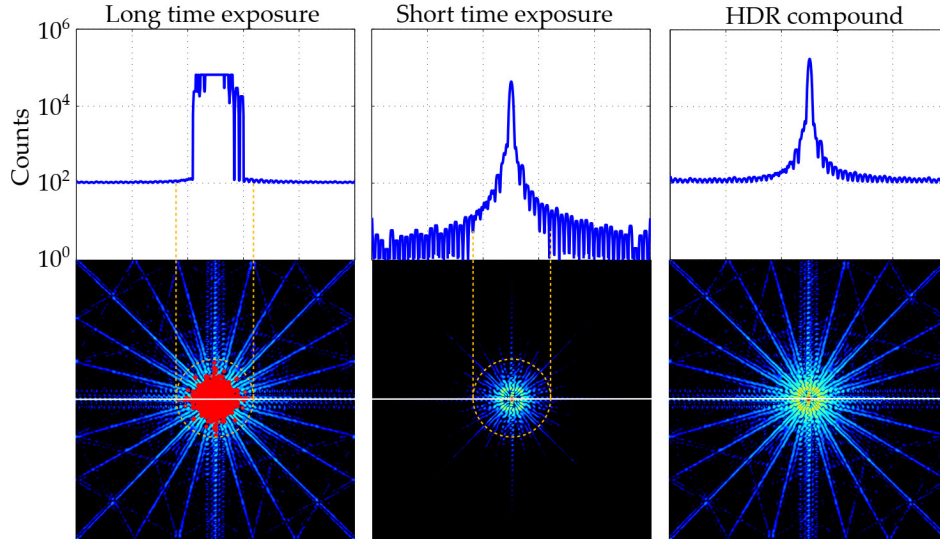


FIGURE A.3: Principle of HDR merging of diffraction pattern. The overexposed area (red) of the long exposure image (left) is used to create a mask $\hat{\mathbf{M}}_{\text{HDR}}$. Pixel values laying on a circle (yellow, dashed) slightly larger than the mask from both images are used for the intensity adjustment (eq.xxx). Afterwards, the images are merged to a HDR image (right). The lineouts (white lines) show the increase of the dynamic range. Here, a 16 bit dynamic of the recorded images were assumed. The HDR compound increases the dynamic to 17 bit

$$C_{\text{HDR}} = \frac{1}{N} \sum_{n=1}^N \frac{\hat{\mathbf{I}}_{\text{long}}(x_n, y_n)}{\hat{\mathbf{I}}_{\text{short}}(x_n, y_n)} \quad (\text{A.10})$$

Where, $\hat{\mathbf{I}}_{\text{long}}(x_n, y_n)$ and $\hat{\mathbf{I}}_{\text{short}}(x_n, y_n)$ are the pixel values laying on the circle, marking the intersection between short- and long exposure image, with coordinates x_n, y_n (indicated in Fig. A.3) and total pixel count N . The HDR image results of merging the measured diffraction patterns with

$$\hat{\mathbf{I}}_{\text{HDR}} = |1 - \hat{\mathbf{M}}_{\text{HDR}}| \hat{\mathbf{I}}_{\text{long}} + C_{\text{HDR}} \hat{\mathbf{M}}_{\text{HDR}} \hat{\mathbf{I}}_{\text{short}} \quad (\text{A.11})$$

Further improvements can be made by smoothing the boundary between the merged images to preserve a continuous intensity distribution.

Appendix B

Simulation of diffraction pattern

B.1 Framework

The presented procedures rely mostly on a precise simulation of diffraction data out of a given complex-valued aperture considering absorption and refraction. Beside numerical Fresnel- and Fraunhofer propagation of arbitrary fields using forth and back Fourier transforms, a more simpler methods was implemented to ensure high speed simulations. This, however, is only valid for far-field diffraction, which has to be consider during the experiments. The code "k_mask" basically rely on a single Fourier transform of the complex input. Taking into account, that the used fast Fourier transform (FFT) project the highest spatial frequencies to the outer edge of the output, one can simulate arbitrary distanced diffraction pattern by cropping or zero-padding the input field. Here, one pixel of the input matrix defines the highest possible resolution and is represented by $\lambda/2$ assuming an NA of 1. By adapting the perfect resolution to the experimental one via decreasing the input resolution, low-NA diffraction can be simulated. Therefore, only the wavelength, distance and the detector size is necessary for the processing. As a result, the quality of the outcome is only dependent on the input field.

Input : complex-valued field Φ_{in} , energy E , distance z , sample size a , detector size d , detector pixel count p , pixel threshold t

Output : complex-valued diffraction pattern Φ_{out}

Calculate numerical aperture $NA = \sin(\arctan(d/(2z)))$

Calculate resolution $r = (hc)/(2E * NA)$

Calculate overall dimension of down-sampled object $b = rp$

Calculate shrink factor $s = a/b$

if $s < 1$ **then**

 | Zero-pad Φ_{in} by factor s

else

 | Crop Φ_{in} by factor s

end

Calculate diffraction $\Phi_{out} = \mathfrak{F}(\Phi_{in})$

Simulate CCD sensitivity:

if $|\Phi_{out}| < t$ **then**

 | $|\Phi_{out}| = 0$

else

 | nothing

end

Generate result: $\Phi_{out} = |\Phi_{out}| * \exp(i * \arg(\Phi_{out}))$

Bibliography

1. De Broglie, L. *Recherches sur la théorie des Quanta* fr. PhD thesis (1924).
2. Knoll, M. & Ruska, E. Das Elektronenmikroskop. de. *Zeitschrift für Physik* **79**, 699–699. ISSN: 0044-3328 (Sept. 1932).
3. Liu, D. *et al.* Demonstration of a novel focusing small-angle neutron scattering instrument equipped with axisymmetric mirrors. en. *Nature Communications* **4**. Number: 1 Publisher: Nature Publishing Group, 1–5. ISSN: 2041-1723 (Sept. 2013).
4. Müller, E. W. Das Feldionenmikroskop. de. *Zeitschrift für Physik* **131**, 136–142. ISSN: 0044-3328 (Mar. 1951).
5. Abbe, E. Beiträge zur Theorie des Mikroskops und der mikroskopischen Wahrnehmung. de. *Archiv für Mikroskopische Anatomie* **9**, 413–468. ISSN: 0176-7364 (Dec. 1873).
6. Köhler, A. Ein neues Beleuchtungsverfahren für mikrophotographische Zwecke. ger. *Zeitschrift für wissenschaftliche Mikroskopie und für mikroskopische Technik* **10**, 28 (1893).
7. Heimstädt, O. Das Fluoreszenzmikroskop. *Zeitschrift für wissenschaftliche Mikroskopie und für mikroskopische Technik* **28**, 330 (1911).
8. Denk, W., Strickler, J. H. & Webb, W. W. Two-photon laser scanning fluorescence microscopy. en. *Science* **248**. Publisher: American Association for the Advancement of Science Section: Reports, 73–76. ISSN: 0036-8075, 1095-9203 (Apr. 1990).
9. Hell, S. W. & Wichmann, J. Breaking the diffraction resolution limit by stimulated emission: stimulated-emission-depletion fluorescence microscopy. EN. *Optics Letters* **19**, 780–782. ISSN: 1539-4794 (June 1994).
10. Snigirev, A., Kohn, V., Snigireva, I. & Lengeler, B. A compound refractive lens for focusing high-energy X-rays. en. *Nature* **384**. Number: 6604 Publisher: Nature Publishing Group, 49–51. ISSN: 1476-4687 (Nov. 1996).

11. MacDonald, C. A. *Focusing Polycapillary Optics and Their Applications* en. Review Article. ISSN: 1687-7632 Library Catalog: www.hindawi.com Pages: e867049 Publisher: Hindawi Volume: 2010. 2010.
12. Mohacsi, I. *et al.* Interlaced zone plate optics for hard X-ray imaging in the 10 nm range. en. *Scientific Reports* **7**. Number: 1 Publisher: Nature Publishing Group, 1–10. ISSN: 2045-2322 (Mar. 2017).
13. Bayer, A. *et al.* *Structural and chemical surface analysis with EUV/XUV radiation using a broadband laser plasma source and optics system in CLEO/Europe - EQEC 2009 - European Conference on Lasers and Electro-Optics and the European Quantum Electronics Conference* (June 2009), 1–1.
14. Fuchs, S. *et al.* Nanometer resolution optical coherence tomography using broad bandwidth XUV and soft x-ray radiation. en. *Scientific Reports* **6**. Number: 1 Publisher: Nature Publishing Group, 1–6. ISSN: 2045-2322 (Feb. 2016).
15. Sayre, D., Kirz, J., Feder, R., Kim, D. M. & Spiller, E. Potential operating region for ultrasoft x-ray microscopy of biological materials. eng. *Science (New York, N.Y.)* **196**, 1339–1340. ISSN: 0036-8075 (June 1977).
16. Legall, H *et al.* A compact Laboratory Transmission X-ray Microscope for the water window. *Journal of Physics: Conference Series* **463**, 012013. ISSN: 1742-6596 (Oct. 2013).
17. Fienup, J. Reconstruction of a complex-valued object from the modulus of its Fourier transform using a support constraint. *Optical Society of America* **4**, 521–553 (1987).
18. Goodman, J. W. & Lawrence, R. W. Digital image formation from electronically detected holograms. *Applied Physics Letters* **11**. Publisher: American Institute of Physics, 77–79. ISSN: 0003-6951 (Aug. 1967).
19. Gerchberg, R. W. & Saxton, W. O. A Practical Algorithm for the Determination of Phase from Image and Diffraction Plane Pictures. *Optik* **35**, 237 (1971).
20. Fienup, J. R. Phase retrieval algorithms: a comparison. EN. *Applied Optics* **21**, 2758–2769. ISSN: 2155-3165 (Aug. 1982).
21. Miao, J., Sayre, D. & Chapman, H. N. Phase retrieval from the magnitude of the Fourier transforms of nonperiodic objects. EN. *JOSA A* **15**, 1662–1669. ISSN: 1520-8532 (June 1998).

22. Sayre, D. Some implications of a theorem due to Shannon. en. *Acta Crystallographica* **5**. Number: 6 Publisher: International Union of Crystallography, 843–843. ISSN: 0365-110X (Nov. 1952).
23. Rodenburg, J. M. & Bates, R. H. T. The theory of super-resolution electron microscopy via Wigner-distribution deconvolution. *Philosophical Transactions of the Royal Society of London. Series A: Physical and Engineering Sciences* **339**. Publisher: Royal Society, 521–553 (June 1992).
24. Maiden, A. M., Humphry, M. J., Sarahan, M. C., Kraus, B. & Rodenburg, J. M. An annealing algorithm to correct positioning errors in ptychography. en. *Ultramicroscopy* **120**, 64–72. ISSN: 0304-3991 (Sept. 2012).
25. Thibault, P., Dierolf, M., Bunk, O., Menzel, A. & Pfeiffer, F. Probe retrieval in ptychographic coherent diffractive imaging. *Ultramicroscopy* **109**, 338–343. ISSN: 0304-3991 (Mar. 2009).
26. Valzania, L., Feurer, T., Zolliker, P. & Hack, E. Terahertz ptychography. en. *Optics Letters* **43**, 543. ISSN: 0146-9592, 1539-4794 (Feb. 2018).
27. Da Silva, J. C. *et al.* Overcoming the challenges of high-energy X-ray ptychography. en. *Journal of Synchrotron Radiation* **26**. Number: 5 Publisher: International Union of Crystallography, 1751–1762. ISSN: 1600-5775 (Sept. 2019).
28. Saleh, B. E. A. & Teich, M. C. *Fundamentals of Photonics* (John Wiley & Sons, Ltd, 1991).
29. Born, M. *et al.* *Principles of Optics: Electromagnetic Theory of Propagation, Interference and Diffraction of Light* en. ISBN: 9780521642224 9780521784498 9781139644181 Library Catalog: www.cambridge.org Publisher: Cambridge University Press. Oct. 1999.
30. Gu, M. *Advanced Optical Imaging Theory* en. ISBN: 978-3-540-66262-4 (Springer-Verlag, Berlin Heidelberg, 2000).
31. Ewald, P. P. Zur Theorie der Interferenzen der Röntgenstrahlen in Kristallen. *Physikalische Zeitschrift* **14**, 465–472 (1913).
32. Shannon, C. E. Communication In The Presence Of Noise. *Proceedings of the IEEE* **86**, 447–457. ISSN: 0018-9219 (Feb. 1998).

33. Miao, J., Ishikawa, T., Anderson, E. H. & Hodgson, K. O. Phase retrieval of diffraction patterns from noncrystalline samples using the oversampling method. *Physical Review B* **67**. Publisher: American Physical Society, 174104 (May 2003).
34. Bates, R. H. T. Uniqueness of solutions to two-dimensional fourier phase problems for localized and positive images. *Computer Vision, Graphics, and Image Processing* **25**, 205–217. ISSN: 0734-189X (Feb. 1984).
35. Serov, V. *Fourier Series, Fourier Transform and Their Applications to Mathematical Physics* English. Publisher: Springer. 2017.
36. Luke, D. R. Relaxed averaged alternating reflections for diffraction imaging. en. *Inverse Problems* **21**, 37–50. ISSN: 0266-5611 (Nov. 2004).
37. Zürich, M. *High-Resolution Extreme Ultraviolet Microscopy: Imaging of Artificial and Biologic Specimens with Laser-driven Ultrafast XUV Sources* (2015).
38. Maiden, A. M. & Rodenburg, J. M. An improved ptychographical phase retrieval algorithm for diffractive imaging. en. *Ultramicroscopy* **109**, 1256–1262. ISSN: 03043991 (Sept. 2009).
39. Chapman, H. N. *et al.* High-resolution ab initio three-dimensional x-ray diffraction microscopy. EN. *JOSA A* **23**, 1179–1200. ISSN: 1520-8532 (May 2006).
40. Howells, M. R. *et al.* An assessment of the resolution limitation due to radiation-damage in X-ray diffraction microscopy. en. *Journal of Electron Spectroscopy and Related Phenomena. Radiation Damage* **170**, 4–12. ISSN: 0368-2048 (Mar. 2009).
41. Chapman, H. N., Caleman, C. & Timneanu, N. Diffraction before destruction. eng. *Philosophical Transactions of the Royal Society of London. Series B, Biological Sciences* **369**, 20130313. ISSN: 1471-2970 (July 2014).
42. HANBURY BROWN, R. & TWISS, R. Q. A Test of a New Type of Stellar Interferometer on Sirius. *Nature* **178**, 1046–1048. ISSN: 1476-4687 (Nov. 1956).
43. Pelliccia, D., Rack, A., Scheel, M., Cantelli, V. & Paganin, D. M. Experimental X-Ray Ghost Imaging. *Physical Review Letters* **117**, 113902 (Sept. 2016).
44. Wiedemann, H. *Particle Accelerator Physics* (Springer International Publishing, 2015).

45. McPherson, A. *et al.* Studies of multiphoton production of vacuum-ultraviolet radiation in the rare gases. EN. *JOSA B* **4**. Publisher: Optical Society of America, 595–601. ISSN: 1520-8540 (Apr. 1987).
46. Ferray, M. *et al.* Multiple-harmonic conversion of 1064 nm radiation in rare gases. en. *Journal of Physics B: Atomic, Molecular and Optical Physics* **21**. Publisher: IOP Publishing, L31–L35. ISSN: 0953-4075 (Feb. 1988).
47. Hentschel, M. *et al.* Attosecond metrology. en. *Nature* **414**, 509–513. ISSN: 1476-4687 (Nov. 2001).
48. Keldysh, L. V. IONIZATION IN THE FIELD OF A STRONG ELECTROMAGNETIC WAVE. Russian. *Zh. Eksperim. i Teor. Fiz.* **Vol: 47**. Institution: Lebedev Inst. of Physics, Moscow (Nov. 1964).
49. Brabec, T. & Krausz, F. Intense few-cycle laser fields: Frontiers of nonlinear optics. en. *Reviews of Modern Physics* **72**, 545–591. ISSN: 0034-6861, 1539-0756 (Apr. 2000).
50. Liu, C. S., Tripathi, V. K. & Eliasson, B. *High-Power Laser-Plasma Interaction* en. Google-Books-ID: v3SmDwAAQBAJ. ISBN: 978-1-108-61822-9 (Cambridge University Press, May 2019).
51. Sebban, S. *et al.* Demonstration of a Ni-Like Kr Optical-Field-Ionization Collisional Soft X-Ray Laser at 32.8 nm. *Phys. Rev. Lett.* **89**, 253901 (Nov. 2002).
52. Zürich, M. *et al.* Transverse Coherence Limited Coherent Diffraction Imaging using a Molybdenum Soft X-ray Laser Pumped at Moderate Pump Energies. en. *Scientific Reports* **7**, 5314. ISSN: 2045-2322 (July 2017).
53. Helk, T., Zürich, M. & Spielmann, C. Perspective: Towards single shot time-resolved microscopy using short wavelength table-top light sources. *Structural Dynamics* **6**, 010902 (Jan. 2019).
54. Bahrtdt, J. *et al.* APPLE Undulator for PETRA III. en. *Conf.Proc.C* **0806233** (June 2008).
55. Holler, M. *et al.* High-resolution non-destructive three-dimensional imaging of integrated circuits. en. *Nature* **543**, 402–406. ISSN: 1476-4687 (Mar. 2017).
56. Shapiro, D. *et al.* Biological imaging by soft x-ray diffraction microscopy. en. *Proceedings of the National Academy of Sciences* **102**, 15343–15346. ISSN: 0027-8424, 1091-6490 (Oct. 2005).

57. Fogelqvist, E., Kördel, M., Carannante, V., Önfelt, B. & Hertz, H. M. Laboratory cryo x-ray microscopy for 3D cell imaging. *Scientific Reports* **7**. ISSN: 2045-2322 (Oct. 2017).
58. Banyay, M. *et al.* XUV metrology: surface analysis with extreme ultraviolet radiation in *Damage to VUV, EUV, and X-Ray Optics II* **7361** (International Society for Optics and Photonics, May 2009), 736113.
59. Pelka, J. B. *et al.* Damage in solids irradiated by a single shot of XUV free-electron laser: Irreversible changes investigated using X-ray microdiffraction, atomic force microscopy and Nomarski optical microscopy. en. *Radiation Physics and Chemistry* **78**, S46–S52. ISSN: 0969-806X (Oct. 2009).
60. Takahashi, Y. *et al.* Observation of electromigration in a Cu thin line by in situ coherent x-ray diffraction microscopy. *Journal of Applied Physics* **105**. Publisher: American Institute of Physics, 124911. ISSN: 0021-8979 (June 2009).
61. Rose, M. *et al.* Quantitative ptychographic bio-imaging in the water window. EN. *Optics Express* **26**, 1237–1254. ISSN: 1094-4087 (Jan. 2018).
62. Horstmeyer, R., Heintzmann, R., Popescu, G., Waller, L. & Yang, C. Standardizing the resolution claims for coherent microscopy. en. *Nature Photonics* **10**. Number: 2 Publisher: Nature Publishing Group, 68–71. ISSN: 1749-4893 (Feb. 2016).
63. Seaberg, M. D. *et al.* Tabletop nanometer extreme ultraviolet imaging in an extended reflection mode using coherent Fresnel ptychography. EN. *Optica* **1**. Publisher: Optical Society of America, 39–44. ISSN: 2334-2536 (July 2014).
64. Gibson, J. M., Lanzerotti, M. Y. & Elser, V. Plan-view transmission electron diffraction measurement of roughness at buried Si-SiO₂ interfaces. *Applied Physics Letters* **55**. Publisher: American Institute of Physics, 1394–1396. ISSN: 0003-6951 (Oct. 1989).
65. Hayashida, M., Ogawa, S. & Malac, M. Tomographic measurement of buried interface roughness. *Microscopy and Microanalysis* **21**. Publisher: Cambridge University Press, 2243–2244 (2015).
66. Yoshino, H. *et al.* Measurement of thin film interfacial surface roughness by coherence scanning interferometry. *Journal of Applied Physics* **121**. Publisher: American Institute of Physics, 105303. ISSN: 0021-8979 (Mar. 2017).

67. Johansson, G. A., Holmberg, A., Hertz, H. M. & Berglund, M. Design and performance of a laser-plasma-based compact soft x-ray microscope. *Review of Scientific Instruments* **73**. Publisher: American Institute of Physics, 1193–1197. ISSN: 0034-6748 (Mar. 2002).
68. Rymell, L., Berglund, M. & Hertz, H. M. Debris-free single-line laser-plasma x-ray source for microscopy. *Applied Physics Letters* **66**. Publisher: American Institute of Physics, 2625–2627. ISSN: 0003-6951 (May 1995).
69. Jansson, P. a. C., Vogt, U. & Hertz, H. M. Liquid-nitrogen-jet laser-plasma source for compact soft x-ray microscopy. *Review of Scientific Instruments* **76**, 043503. ISSN: 0034-6748 (Mar. 2005).
70. Benk, M., Bergmann, K., Schäfer, D. & Wilhein, T. Compact soft x-ray microscope using a gas-discharge light source. EN. *Optics Letters* **33**. Publisher: Optical Society of America, 2359–2361. ISSN: 1539-4794 (Oct. 2008).
71. Benk, M., Schäfer, D., Wilhein, T. & Bergmann, K. High power soft x-ray source based on a discharge plasma. *Journal of Physics: Conference Series* **186**, 012024. ISSN: 1742-6596 (Sept. 2009).
72. Legall, H. *et al.* Compact x-ray microscope for the water window based on a high brightness laser plasma source. EN. *Optics Express* **20**, 18362–18369. ISSN: 1094-4087 (July 2012).
73. Graham, F. L., Smiley, J., Russell, W. C. & Nairn, R. Characteristics of a human cell line transformed by DNA from human adenovirus type 5. eng. *The Journal of General Virology* **36**, 59–74. ISSN: 0022-1317 (July 1977).
74. Stepanenko, A. A. & Dmitrenko, V. V. HEK293 in cell biology and cancer research: phenotype, karyotype, tumorigenicity, and stress-induced genome-phenotype evolution. eng. *Gene* **569**, 182–190. ISSN: 1879-0038 (Sept. 2015).
75. Shukla, S. *et al.* In vitro toxicity assessment of chitosan oligosaccharide coated iron oxide nanoparticles. *Toxicology Reports* **2**, 27–39. ISSN: 2214-7500 (Nov. 2014).
76. Kimura, T. *et al.* Imaging live cell in micro-liquid enclosure by X-ray laser diffraction. en. *Nature Communications* **5**. Number: 1 Publisher: Nature Publishing Group, 1–7. ISSN: 2041-1723 (Jan. 2014).

77. Kirz, J., Jacobsen, C. & Howells, M. Soft X-ray microscopes and their biological applications. en. *Quarterly Reviews of Biophysics* **28**. Publisher: Cambridge University Press, 33–130. ISSN: 1469-8994, 0033-5835 (Feb. 1995).
78. Lo, Y. H. *et al.* In situ coherent diffractive imaging. en. *Nature Communications* **9**. Number: 1 Publisher: Nature Publishing Group, 1–10. ISSN: 2041-1723 (May 2018).
79. Marchesini, S. *et al.* Coherent X-ray diffractive imaging: applications and limitations. EN. *Optics Express* **11**, 2344–2353. ISSN: 1094-4087 (Sept. 2003).
80. Gianoncelli, A. *et al.* Soft X-Ray Microscopy Radiation Damage On Fixed Cells Investigated With Synchrotron Radiation FTIR Microscopy. *Scientific Reports* **5**, 10250 (May 2015).
81. Lloyd, D. T., O’Keeffe, K. & Hooker, S. M. Complete spatial characterization of an optical wavefront using a variable-separation pinhole pair. EN. *Optics Letters* **38**, 1173–1175. ISSN: 1539-4794 (Apr. 2013).
82. Delen, N. & Hooker, B. Free-space beam propagation between arbitrarily oriented planes based on full diffraction theory: a fast Fourier transform approach. EN. *JOSA A* **15**. Publisher: Optical Society of America, 857–867. ISSN: 1520-8532 (Apr. 1998).
83. Xiao, X. & Voelz, D. Wave optics simulation approach for partial spatially coherent beams. EN. *Optics Express* **14**. Publisher: Optical Society of America, 6986–6992. ISSN: 1094-4087 (Aug. 2006).
84. Jaeglé, P. *Coherent Sources of XUV Radiation* ISBN: 978-0-387-29990-7 (Springer International Publishing, 2006).
85. Zeitoun, P. *et al.* A high-intensity highly coherent soft X-ray femtosecond laser seeded by a high harmonic beam. en. *Nature* **431**, 426–429. ISSN: 1476-4687 (Sept. 2004).
86. Depresseux, A. *et al.* Table-top femtosecond soft X-ray laser by collisional ionization gating. en. *Nature Photonics* **9**, 817–821. ISSN: 1749-4893 (Dec. 2015).
87. Essert, S. & Christian Schneider, H. Electron-phonon scattering dynamics in ferromagnets on ultrafast timescales: Influence of the phonon temperature. *Journal of Applied Physics* **111**, 07C514. ISSN: 0021-8979 (Mar. 2012).

88. Nicholson, C. W. *et al.* Beyond the molecular movie: Dynamics of bands and bonds during a photoinduced phase transition. en. *Science* **362**. Publisher: American Association for the Advancement of Science Section: Report, 821–825. ISSN: 0036-8075, 1095-9203 (Nov. 2018).
89. Tadesse, G. K. *et al.* Wavelength-scale ptychographic coherent diffractive imaging using a high-order harmonic source. *Scientific Reports* **9**, 1735. ISSN: 2045-2322 (Feb. 2019).
90. Helander, P. *et al.* Stellarator and tokamak plasmas: a comparison. en. *Plasma Physics and Controlled Fusion* **54**, 124009. ISSN: 0741-3335 (Nov. 2012).
91. Li, Z. *et al.* Experimental investigation of Z-pinch radiation source for indirect drive inertial confinement fusion. *Matter and Radiation at Extremes* **4**, 046201. ISSN: 2468-2047 (July 2019).
92. Spielmann, C. *et al.* Generation of Coherent X-rays in the Water Window Using 5-Femtosecond Laser Pulses. *Science* **278**, 661 (Oct. 1997).
93. Cayzac, W. *et al.* Experimental discrimination of ion stopping models near the Bragg peak in highly ionized matter. en. *Nature Communications* **8**, 1–7. ISSN: 2041-1723 (June 2017).
94. Vinko, S. M. *et al.* Investigation of femtosecond collisional ionization rates in a solid-density aluminium plasma. en. *Nature Communications* **6**, 1–7. ISSN: 2041-1723 (Mar. 2015).
95. Joshi, C. *et al.* Ultrahigh gradient particle acceleration by intense laser-driven plasma density waves. en. *Nature* **311**, 525–529. ISSN: 1476-4687 (Oct. 1984).
96. Sullivan, J. V. & Walsh, A. High intensity hollow-cathode lamps. *Spectrochimica Acta* **21**, 721–726. ISSN: 0371-1951 (Apr. 1965).
97. Wagner, C. & Harned, N. Lithography gets extreme. en. *Nature Photonics* **4**, 24–26. ISSN: 1749-4893 (Jan. 2010).
98. Silfvast, W. Intense EUV incoherent plasma sources for EUV lithography and other applications. *IEEE Journal of Quantum Electronics* **35**, 700–708. ISSN: 0018-9197, 1558-1713 (May 1999).

99. Schmitz, C. *et al.* Compact extreme ultraviolet source for laboratory-based photoemission spectromicroscopy. *Applied Physics Letters* **108**, 234101. ISSN: 0003-6951 (June 2016).
100. Bukin, V. V., Garnov, S. V., Malyutin, A. A. & Strelkov, V. V. Interferometric diagnostics of femtosecond laser microplasma in gases. en. *Physics of Wave Phenomena* **20**, 91–106. ISSN: 1934-807X (Apr. 2012).
101. Gopal, A., Minardi, S. & Tatarakis, M. Quantitative two-dimensional shadowgraphic method for high-sensitivity density measurement of under-critical laser plasmas. EN. *Optics Letters* **32**, 1238–1240. ISSN: 1539-4794 (May 2007).
102. Sävert, A. *et al.* Direct Observation of the Injection Dynamics of a Laser Wakefield Accelerator Using Few-Femtosecond Shadowgraphy. *Physical Review Letters* **115**. Publisher: American Physical Society, 055002 (July 2015).
103. Cao, L. *et al.* Space-time characterization of laser plasma interactions in the warm dense matter regime. *Laser Part. Beams* 25(2007)2,239-244 **25** (Apr. 2008).
104. Schnell, M. *et al.* Deducing the Electron-Beam Diameter in a Laser-Plasma Accelerator Using X-Ray Betatron Radiation. *Physical Review Letters* **108**. Publisher: American Physical Society, 075001 (Feb. 2012).
105. Oliva, E. *et al.* DAGON: a 3D Maxwell-Bloch code in (eds Klisnick, A. & Menoni, C. S.) (Prague, Czech Republic, June 2017), 1024303.
106. Cros, B. *et al.* Characterization of the collisionally pumped optical-field-ionized soft-x-ray laser at 41.8 nm driven in capillary tubes. *Physical Review A* **73**, 033801 (Mar. 2006).
107. Oliva, E. *et al.* Hydrodynamic evolution of plasma waveguides for soft-x-ray amplifiers. *Physical Review E* **97**, 023203 (Feb. 2018).
108. Oliva, E. *et al.* Self-regulated propagation of intense infrared pulses in elongated soft-x-ray plasma amplifiers. *Physical Review A* **92**, 023848 (Aug. 2015).
109. Paradkar, B. S., Cros, B., Mora, P. & Maynard, G. Numerical modeling of multi-GeV laser wakefield electron acceleration inside a dielectric capillary tube. *Physics of Plasmas* **20**, 083120. ISSN: 1070-664X (Aug. 2013).

110. Lifschitz, A. F. *et al.* Particle-in-Cell modelling of laser–plasma interaction using Fourier decomposition. *Journal of Computational Physics* **228**, 1803–1814. ISSN: 0021-9991 (Mar. 2009).
111. Ogando, F. & Velarde, P. Development of a radiation transport fluid dynamic code under AMR scheme. *Journal of Quantitative Spectroscopy and Radiative Transfer* **71**, 541–550. ISSN: 0022-4073 (Oct. 2001).
112. Carlström, S., Mauritsson, J., Schafer, K. J., L’Huillier, A. & Gisselbrecht, M. Quantum coherence in photo-ionisation with tailored XUV pulses. en. *Journal of Physics B: Atomic, Molecular and Optical Physics* **51**. Publisher: IOP Publishing, 015201. ISSN: 0953-4075 (Nov. 2017).
113. Wituschek, A. *et al.* Tracking attosecond electronic coherences using phase-manipulated extreme ultraviolet pulses. en. *Nature Communications* **11**. Number: 1 Publisher: Nature Publishing Group, 1–7. ISSN: 2041-1723 (Feb. 2020).
114. Loriot, V *et al.* Resolving XUV induced femtosecond and attosecond dynamics in polyatomic molecules with a compact attosecond beamline. *Journal of Physics: Conference Series* **635**, 012006. ISSN: 1742-6588, 1742-6596 (Sept. 2015).
115. Lazarev, S. *et al.* Ptychographic X-Ray Imaging of Colloidal Crystals. en. *Small* **14**, 1702575. ISSN: 1613-6829 (2018).
116. Mancini, G. F. *et al.* Colloidal crystal order and structure revealed by tabletop extreme ultraviolet scattering and coherent diffractive imaging. EN. *Optics Express* **26**, 11393–11406. ISSN: 1094-4087 (Apr. 2018).
117. Thibault, P. *et al.* High-Resolution Scanning X-ray Diffraction Microscopy. en. *Science* **321**, 379–382. ISSN: 0036-8075, 1095-9203 (July 2008).
118. Shapiro, D. A. *et al.* Chemical composition mapping with nanometre resolution by soft X-ray microscopy. en. *Nature Photonics* **8**, 765–769. ISSN: 1749-4893 (Oct. 2014).
119. Helfenstein, P., Mohacsi, I., Rajendran, R. & Ekinci, Y. *Scanning coherent diffractive imaging methods for actinic EUV mask metrology in Extreme Ultraviolet (EUV) Lithography VII* (eds Panning, E. M. & Goldberg, K. A.) (SPIE, Mar. 2016).

120. Hovden, R., Jiang, Y., Xin, H. L. & Kourkoutis, L. F. Periodic Artifact Reduction in Fourier Transforms of Full Field Atomic Resolution Images. en. *Microscopy and Microanalysis* **21**, 436–441. ISSN: 1431-9276, 1435-8115 (Apr. 2015).
121. Truong, N. X. *et al.* Coherent Tabletop EUV Ptychography of Nanopatterns. *Scientific Reports* **8**, 16693. ISSN: 2045-2322 (Nov. 2018).
122. Gardner, D. F. *et al.* Subwavelength coherent imaging of periodic samples using a 13.5 nm tabletop high-harmonic light source. en. *Nature Photonics* **11**, 259–263. ISSN: 1749-4885, 1749-4893 (Mar. 2017).
123. Zhang, F. *et al.* Translation position determination in ptychographic coherent diffraction imaging. EN. *Optics Express* **21**, 13592–13606. ISSN: 1094-4087 (June 2013).
124. Khakurel, K. P. *et al.* Coherent diffraction imaging of non-isolated object with apodized illumination. EN. *Optics Express* **23**, 28182–28190. ISSN: 1094-4087 (Nov. 2015).
125. Nagata, Y., Harada, T., Watanabe, T., Kinoshita, H. & Midorikawa, K. At wavelength coherent scatterometry microscope using high-order harmonics for EUV mask inspection. en. *International Journal of Extreme Manufacturing* **1**, 032001. ISSN: 2631-7990 (Sept. 2019).
126. Latychevskaia, T. Iterative phase retrieval in coherent diffractive imaging: practical issues. EN. *Applied Optics* **57**. Publisher: Optical Society of America, 7187–7197. ISSN: 2155-3165 (Sept. 2018).
127. Park, S., Linsen, L., Kreylos, O., Owens, J. D. & Hamann, B. Discrete Sibson Interpolation. en. *IEEE Transactions on Visualization and Computer Graphics* **12** (2006).
128. Green, P. J. & Sibson, R. Computing Dirichlet Tessellations in the Plane. en. *The Computer Journal* **21**. Publisher: Oxford Academic, 168–173. ISSN: 0010-4620 (May 1978).
129. Wu, Q. *Microscope image processing* English. Publisher: Elsevier / Academic Press. 2008.
130. Serov, V. en. in *Fourier Series, Fourier Transform and Their Applications to Mathematical Physics* (ed Serov, V.) 23–25 (Springer International Publishing, Cham, 2017). ISBN: 978-3-319-65262-7.
131. Gallaway, M. *An Introduction to Observational Astrophysics* en. Google-Books-ID: n_XuCgAAQBAJ. ISBN: 978-3-319-23377-2 (Springer, Nov. 2015).

132. Sun, T., Jiang, Z., Strzalka, J., Ocola, L. & Wang, J. Three-dimensional coherent X-ray surface scattering imaging near total external reflection. en. *Nature Photonics* **6**, 586–590. ISSN: 1749-4893 (Sept. 2012).
133. Porter, C. L. *et al.* General-purpose, wide field-of-view reflection imaging with a tabletop 13  nm light source. EN. *Optica* **4**, 1552–1557. ISSN: 2334-2536 (Dec. 2017).
134. Gardner, D. F. *et al.* High numerical aperture reflection mode coherent diffraction microscopy using off-axis apertured illumination. EN. *Optics Express* **20**, 19050–19059. ISSN: 1094-4087 (Aug. 2012).
135. Rose, M. *et al.* High-dynamic-range water window ptychography. en. *Journal of Physics: Conference Series* **849**, 012027. ISSN: 1742-6588, 1742-6596 (June 2017).
136. Evans, K. & Beanland, R. High Dynamic Range Electron Imaging: The New Standard. en. *Microscopy and Microanalysis* **20**. Publisher: Cambridge University Press, 1601–1604. ISSN: 1431-9276, 1435-8115 (Oct. 2014).
137. Tuitje, F. *et al.* Nonlinear Ionization Dynamics of Hot Dense Plasma Observed in a Laser-Plasma Amplifier. *Light Science and Applications* **In peer review**.
142. Sun, Z., Tuitje, F. & Spielmann, C. Toward high contrast and high-resolution microscopic ghost imaging. EN. *Optics Express* **27**, 33652–33661. ISSN: 1094-4087 (Nov. 2019).
143. Sun, Z., Tuitje, F. & Spielmann, C. Improving the contrast of pseudothermal ghost images based on the measured signal distribution of speckle fields. *Optics Letters* **In peer review**.

List of Figures

2.1	Schematic to the Fresnel-Kirchhoff diffraction formula	12
2.2	Schematic to the Kirchhoff integral theorem	13
2.3	Schematic to the Fresnel/Fraunhofer approximation.	14
2.4	Principle of high harmonic generation	24
2.5	Average brilliance comparison of XUV sources	27
3.1	Transmission windows of different materials for 10 μm thickness . . .	28
3.2	Reflection mode CDI setup at <i>PETRA III</i>	30
3.3	Model of the buried sample structure	31
3.4	Comparison of diffraction pattern of the buried Siemens star in reflection mode.	32
3.5	Comparison of diffraction pattern of the buried Siemens star in reflection mode.	33
3.6	Circumference profiles of the reconstructed Siemens star sample . . .	34
3.7	Retrieved relative height profile of the Siemens star sample	35
4.1	Schematic of the BliX beamline	39
4.2	2.8 μm iron-labeled HEK293 cell.	40
4.3	1 μm iron-labeled HEK293 cell.	41
4.4	Scheme for total flux calculation	43
4.5	Long time exposure diffraction pattern using Nitrogen-plasma based SXRL	44
4.6	Principle of axial jitter decomposition	46
4.7	Schematic of the single-shot beam analyzing algorithm	47
4.8	Stack of correlation matrices	49
4.9	Correlation matrix of the best matching rest position.	50

5.1	Exciting of the laser plasma amplifier and lasing scheme.	54
5.2	Imaging chamber used for diffraction experiments with indicated beam path.	55
5.3	Structure and dimensions of the sample.	56
5.4	Reconstruction of regular hole pattern for determination of the transversal coherence.	58
5.5	Analysis of pattern integrity for coherent merging.	59
5.6	PRTF of a single diffraction pattern and the merged stack.	60
5.7	Analysis of the single-shot bar structure.	62
5.8	Principle of the backpropagation experiment.	65
5.9	Reconstructed object and probe of the SXRL experiment	66
5.10	Propagation of the exit wave trough the focus	67
5.11	Simulated electron and lasing ion density distribution.	68
5.12	Seed pulse after propagation trough the plasma amplifier.	69
5.13	Overlay of simulated and measured radial intensities of the SXRL experiment.	69
6.1	Motivation for a closer investigation of periodic structures in ptychography	73
6.2	Principle of simulated map distortion.	75
6.3	Reconstruction of a Siemens star with increasing map distortion. . .	76
6.4	Reconstruction of a grid with 200 nm period assuming map distortions.	77
6.5	Comparisons between reconstructed probes (Siemens star).	78
6.6	Reconstruction of different imperfections on a grid with 200 nm period assuming no map distortions.	80
6.7	Comparison between the reconstructed probes (defect size).	81
6.8	Reconstruction of the 100 nm period grid with a small defect of 200 nm with different map distortions.	82
6.9	Comparison of the reconstructed probes (map distortion).	83
A.1	Workflow for pre-processing diffraction data.	92
A.2	Geometrical interpretation of remapping the flat detector onto a sphere	96

A.3 Principle of HDR merging of diffraction pattern. 99

List of Abbreviations

- AOI** angle of incidence. 30, 32, 63, 114
- ASE** amplified spontaneous emission. 28, 59, 60
- CCD** charge coupled device. 16, 63
- CDI** coherent diffractive imaging. 4
- DOF** degrees of freedom. 31
- ER** error reduction. 65
- FFT** fast Fourier transform. 117
- FIB** focussed ion beam. 64
- FOV** field-of-view. 2, 37, 74, 76
- HDR** high dynamic range. 68, 115
- HHG** high harmonic generation. 25, 59, 60
- MOS** metal-oxide semiconductor. 29
- OFI** optical field ionization. 61
- PBS** phosphate-buffered saline. 42
- PIC** particle-in-cell. 77, 78
- RAAR** relaxed average alternating reflections. 65
- SNR** signal-to-noise ratio. 94

SXRL soft X-ray Laser. 7, 60, 61, 65

TEM transmission electron microscope. 65

XUV extreme ultraviolet. 3, 29, 31, 59

List of Symbols

λ	Wavelength
$\Delta\lambda$	Spectral width
\mathbf{k}	Wave vector
\mathbf{q}	Momentum transfer vector
ζ_t	Transversal coherence length
ζ_l	Longitudinal coherence length
O	Oversampling degree
U_i	Ionization potential
U_p	Ponderomotive potential
γ	Keldysh parameter
<u>Operators</u>	
\odot	Elementwise Hadamard product
$*$	Convolution
\mathfrak{F}	Fourier Transform
\mathfrak{F}^{-1}	Inverse Fourier Transform
\mathbf{a}	Vector
$\hat{\mathbf{A}}$	Matrix
\dagger	Complex conjugation
\sphericalangle	Angle between vectors
∇^2	Laplacian operator

Physical Constants

Speed of Light in vacuum	$c_0 = 2.997\,924\,58 \times 10^8 \text{ m s}^{-1}$
Planck constant	$h = 6.626\,070\,15 \times 10^{-34} \text{ J s}$
Vacuum permittivity	$\epsilon_0 = 8.854\,187\,812\,8 \times 10^{-12} \text{ A s V}^{-1} \text{ m}^{-1}$
Electron charge	$e = 1.602\,176\,634 \times 10^{-19} \text{ C}$
Electron mass	$m_e = 9.109\,383\,701\,5 \times 10^{-31} \text{ kg}$

Danksagung

Die Zeit des Doktorats ist geprägt durch Höhen und Tiefen und grade innerhalb dieser Extrema ist es unabdingbar, Menschen an seiner Seite zu haben, welche einem während der Tiefen beistehen und während der Höhen mit einem das metaphorische Glas heben. Innerhalb dieser Zeit lernte ich verschiedenste Menschen kennen, die dem Gelingen der Arbeit beigewirkt haben und meinen Dank von ganzem Herzen verdienen. Im Besonderen trifft dies auf die folgenden Personen zu:

- Meinen Betreuer Prof. Dr. Christian Spielmann, welcher mir die Freiheit gelassen hat, eigene Ideen zu verwirklichen und mich auch auf neue Pfade gesetzt hat, falls ich mich festgefahren habe. So manche Idee, wie bspw. das ghost imaging, wäre ohne seine Denkanstöße wohl nicht realisiert worden. Er stand stets hinter mir und meinen Kollegen, wofür ich sehr dankbar bin. Auch wenn ich unangekündigt in sein Büro platze, nahm er sich immer Zeit für meine Fragen.
- Tobias Helk, welcher mit mir zusammen in Paris und Berlin so manche Nachtschicht durchgezogen und im Jenaer Labor stets eine helfende Hand bereitgehalten hat. Wenn es um die Entwicklung neuer Experimente und die Datenanalyse ging, hat er immer ein offenes Ohr gehabt und machte mich auf so manche Probleme aufmerksam. Außerdem hielt er die Kaffeemaschine am Leben.
- Unserem Ingenieur Michael Damm, welcher selbst für die abstrusesten Aufbauten durchdachte Lösungen parat hatte. Durch seine Hilfe konnte so manches Bauteil in Rekordzeit in die Experimente einfließen und so der Zeitplan

eingehalten werden. Des Weiteren möchte ich mich für die vielen angeregten Diskussion bedanken, durch die ich wieder einen freien Kopf bekommen konnte.

- Sarah Dürer, welche mir für fast jede organisatorische Frage eine Antwort liefern konnte. Ohne sie wäre der Verwaltungsdschungel annähernd undurchdringlich.
- Prof. Dr. Michael Zürich, welcher mich während meiner Bachelorzeit an das Thema linsenlose Bildgebung herangeführt hat und mir auch während des Doktorats immer mit Rat und Tat zur Seite stand. Ohne ihn wäre das SXRL Experiment so nicht zustande gekommen.
- Richard Hollinger und Zhanna Samsonova, die immer für einen Plausch bei einer Tasse Kaffee auf dem AG-Sofa zur Verfügung standen.
- Das Team um Dr. Silvio Fuchs und Martin Wünsche, welche das Reflektions-CDI Experiment ermöglicht und bei der Auswertung der Daten für reichlich hilfreichen Diskussionsstoff gesorgt haben.
- Aurelie Dehlinger und Dr. Holger Stiel für das Bereitstellen und den Betrieb der Laser-Plasma Quelle am BliX. Sie haben uns nie im Regen stehen lassen und nach Problemen mit der Quelle so lange getüftelt, bis alles wieder reibungslos lief.
- Dem Team um Dr. Stéphane Sebban am LOA für die Möglichkeit, das SXRL Experiment durchführen zu können. Nach mehreren Stromausfällen in Palaiseau arbeiteten sie unermüdlich, um den Laser innerhalb unserer Strahlzeit wieder

betriebsbereit zu machen.

- Dr. Jan Rothhardt, Wilhelm Eschen und Getnet Tedesse für die vielen Diskussionen und experimentellen Daten rund um Ptychographie.
- Prof. Dr. Stefan Heinemann vom CMB Jena für die Bereitstellung der HEK293 Zellen für das LPP Experiment.
- Generell meinen Kollegen für die gute Zeit und die schönen Feierabende.
- Meinen Freunden, durch die Jena ein Zuhause wurde. Insbesondere Brain und Herr Sounsystem Bombe, die mich nicht nur als eine meiner besten Freunde, sondern auch als Kollegen tatkräftig unterstützt haben.
- Meiner Familie und vor Allem meinen Eltern, Frank und Sabine, ohne deren Hilfe und Geduld ich erst gar nicht zum Doktorat gekommen wäre, sei es durch die unzähligen Stunden Mathenachhilfe während meiner Schulzeit oder die immerwährende Unterstützung in belastenderen Zeiten. Danke, dass ihr immer hinter mir standet.
- Meiner Lebensgefährtin Jantje, welche immer für mich da war, wenn ich sie brauchte und auch dann, wenn ich es nur nicht wusste. Sie gab mir den Rückhalt, ohne den mein Lebensweg und damit diese Arbeit nicht möglich gewesen wäre.

List of scientific contributions

Publications

- Tuitje, F., Martinez Gill, P., Helk, T., Gautier, J., Goddet, J.-P., Tissandier, F., Guggenmos, A., Kleineberg, U., Sebban, S., Oliva, E., Spielmann, C. & Zürich, M. Nonlinear Ionization Dynamics of Hot Dense Plasma Observed in a Laser-Plasma Amplifier. *Light Science and Applications* **In peer review**
- Tuitje, F., Zürich, M., Helk, T., Gautier, J., Tissandier, F., Goddet, J.-P., Oliva, E., Guggenmos, A., Kleineberg, U., Stiel, H., Sebban, S. & Spielmann, C. *Ptychography and Single-Shot Nanoscale Imaging with Plasma-Based Laser Sources* en. in *X-Ray Lasers 2018* (eds Kozlová, M. & Nejd, J.) (Springer International Publishing, Cham, 2020), 155–162. ISBN: 978-3-030-35453-4
- Tuitje, F., Tuitje, F., Eschen, W., Eschen, W., Tadesse, G. K., Tadesse, G. K., Limpert, J., Limpert, J., Rothhardt, J., Rothhardt, J., Rothhardt, J., Spielmann, C. & Spielmann, C. Reliability of ptychography on periodic structures. *EN. OSA Continuum* **3**. Publisher: Optical Society of America, 1691–1702. ISSN: 2578-7519 (June 2020)
- Tuitje, F., Helk, T., Zürich, M. & Spielmann, C. *Extreme ultraviolet lensless imaging of biological specimen* in *Label-free Biomedical Imaging and Sensing (LBIS) 2019* **10890** (International Society for Optics and Photonics, Mar. 2019), 1089029
- Tuitje, F., Helk, T., Zürich, M., Gautier, J., Tissandier, F., Goddet, J.-P., Oliva, E., Guggenmos, A., Kleineberg, U., Sebban, S. & Spielmann, C. *Following the plasma dynamics in a seeded soft x-ray laser with lensless imaging* in *Real-time Measurements, Rogue Phenomena, and Single-Shot Applications IV* **10903** (International Society for Optics and Photonics, Mar. 2019), 109030A

- Tadesse, G. K., Eschen, W., Klas, R., Tschernajew, M., Tuitje, F., Steinert, M., Zilk, M., Schuster, V., Zürich, M., Pertsch, T., Spielmann, C., Limpert, J. & Rothhardt, J. Wavelength-scale ptychographic coherent diffractive imaging using a high-order harmonic source. *Scientific Reports* **9**, 1735. ISSN: 2045-2322 (Feb. 2019)
- Sun, Z., Tuitje, F. & Spielmann, C. Toward high contrast and high-resolution microscopic ghost imaging. EN. *Optics Express* **27**, 33652–33661. ISSN: 1094-4087 (Nov. 2019)
- Sun, Z., Tuitje, F. & Spielmann, C. Improving the contrast of pseudothermal ghost images based on the measured signal distribution of speckle fields. *Optics Letters* **In peer review**

Scientific presentations

- "Following the plasma dynamics in a seeded soft x-ray laser with lensless imaging", *Real-time Measurements, Rogue Phenomena and Single-Shot Applications at SPIE Lase, Photonics West*, San Francisco, USA (2019)
- "Extreme ultraviolet lensless imaging of biological specimen", *Label-free Biomedical Imaging and Sensing at SPIE BiOS, Photonics West*, San Francisco, USA (2019)
- "Ptychographic reconstruction and characterization of optical vortices", *82nd Annual DPG Conference*, Erlangen, Germany (2018)
- "Ptychography and Single-Shot Nanoscale Imaging with Plasma-Based Laser Sources", *16th International Conference on X-Ray Lasers*, Prague, Czech Republic (2018)
- "Lensless diffraction imaging using a HHG seeded X-Ray Laser", *3rd International Workshop on Frontiers of X&XUV Optics and its Applications*, Prague, Czech Republic (2017)

Accompanied theses

- F. Kohrell, "Installation and Characterization of a Semi-Infinite Gas Cell for High Harmonic Generation", Bachelor thesis (2019)
- S. Oh, "High visibility magnifying ghost imaging", Master thesis (2018)
- T. Helk, "Transversal coherence measurements of XUV-radiation created by High Harmonic Generation", Master thesis (2017)

Eidesstattliche Erklärung

Ich erkläre hiermit ehrenwörtlich, dass ich die vorliegende Arbeit selbständig, ohne unzulässige Hilfe Dritter und ohne Benutzung anderer als der angegebenen Hilfsmittel und Literatur angefertigt habe. Die aus anderen Quellen direkt oder indirekt übernommenen Daten und Konzepte sind unter Angabe der Quelle gekennzeichnet.

Bei der Auswahl und Auswertung folgenden Materials haben mir die nachstehend aufgeführten Personen in der jeweils beschriebenen Weise unentgeltlich geholfen:

- Tobias Helk (IOQ Jena): Zusammenarbeit bei Planung und Durchführung der Experimente.
- Michael Damm (IOQ Jena): Entwicklung diverser mechanischer Komponenten für diverse Experimente
- Prof. Dr. Michael Zürch (UC Berkeley): Zusammenarbeit bei der Planung und Auswertung des seeded SXRL Experiments (Kapitel 5).
- Dr. Silvio Fuchs und Martin Wünsche (IOQ Jena): Organisation und Zusammenarbeit bei der Planung und Durchführung des Reflektions CDI Experiments (3).
- Dr. Eduardo Oliva und Pablo Martinez Gill (IFN Madrid): Durchführung der Simulation zur Rekonstruktion des Plasmakanals (Kapitel 5).

- Dr. Stéphane Sebban, Fabien Tissandier und Julien Gautier (LOA Palaiseau): Betrieb des seeded SXRL und experimentelle Zusammenarbeit (Kapitel 5).
- Aurelie Dehlinger und Dr. Holger Stiel (MBI Berlin): Betrieb der Wasserfenster-Quelle und experimentelle Zusammenarbeit (Kapitel 4).
- Dr. Jan Rothhardt, Wilhelm Eschen und Getnet Tadesse (IAP Jena): Bereitstellung experimenteller Daten für den Vergleich mit Simulationen (Kapitel 6).
- Prof. Dr. Stefan Heinemann (CMB Jena): Bereitstellung der HEK293 Zellkulturen (Kapitel 4).

Weitere Personen waren an der inhaltlich-materiellen Erstellung der vorliegenden Arbeit nicht beteiligt. Insbesondere habe ich hierfür nicht die entgeltliche Hilfe von Vermittlungs- bzw. Beratungsdiensten (Promotionsberater oder andere Personen) in Anspruch genommen. Niemand hat von mir unmittelbar oder mittelbar geldwerte Leistungen für Arbeiten erhalten, die im Zusammenhang mit dem Inhalt der vorgelegten Dissertation stehen.

Die Arbeit wurde bisher weder im In- noch im Ausland in gleicher oder ähnlicher Form einer anderen Prüfungsbehörde vorgelegt.

Die geltende Promotionsordnung der Physikalisch-Astronomischen Fakultät ist mir bekannt.

Ich versichere ehrenwörtlich, dass ich nach bestem Wissen die reine Wahrheit gesagt und nichts verschwiegen habe.

Unterschrift:

Datum:
